

Robert Weiß

**Modeling of generation, propagation and runup of
tsunami waves caused by oceanic impacts**

2004

Chapter 1

Background, Aims and Methods

The term **Tsunami** is derived from the Japanese word *tsun ami*, meaning harbor wave. Fig. 1.1 shows an artwork of Katsushika Hokusai, circa 1831 (Hollow Deep Wave), illustrating destructive consequences of a tsunami wave.

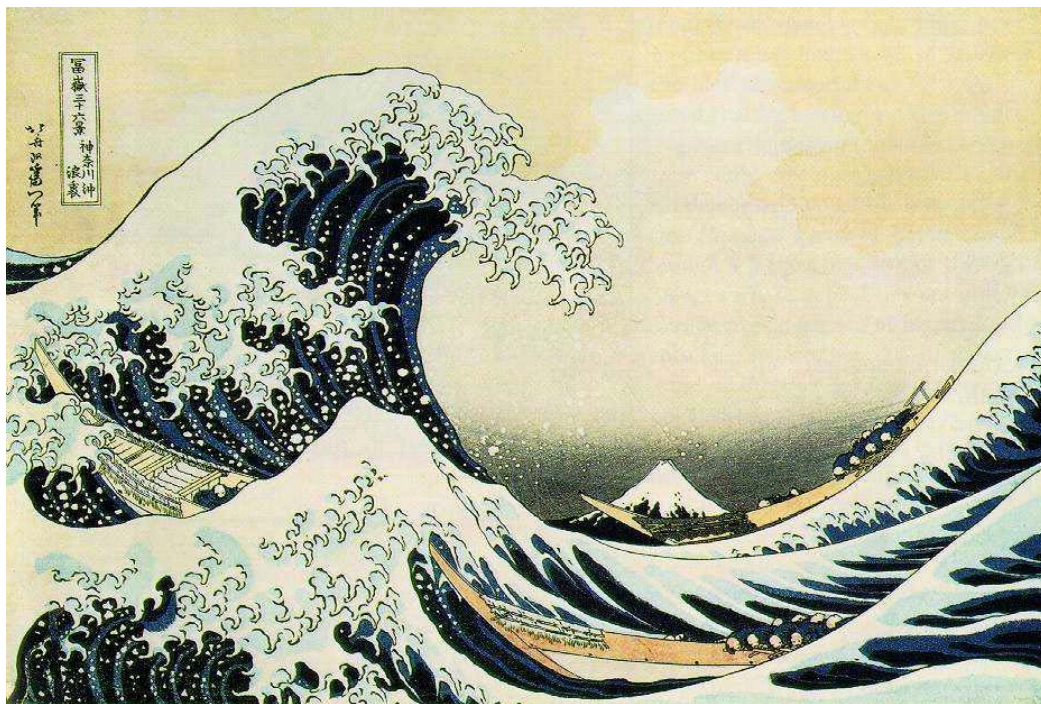


Figure 1.1: Print of the color woodcut, No. 20 from the series 'Thirty-Six Views of Fuji' (ca. 1831), showing the *Hollow of the Deep-Sea Wave*. Many websites and textbooks about tsunami waves depict this artwork as a tsunami wave, but it is a wind-generated wave (Bryant, 2001).

Geologie

Modeling of generation, propagation and runup of tsunami waves caused by oceanic impacts

Inaugural-Dissertation
zur Erlangung des Doktorgrades
der Naturwissenschaften im Fachbereich Geowissenschaften
der Mathematisch-Naturwissenschaftlichen Fakultät
der Westfälischen Wilhelms-Universität Münster

vorgelegt von
Robert Weiß
aus Nordhausen

– 2004 –

Dekan: Prof. Dr. Hans Kerp
Erster Gutachter: Prof. Dr. Heinrich Bahlburg
Zweiter Gutachter Prof. Dr. Costas. E. Synolakis
Tag der mündlichen Prüfung: 26. Januar 2005
Tag der Promotion: 26. Januar 2005

Contents

Abstract	v
Zusammenfassung	vii
1 Background, Aims and Methods	1
2 Impacts and Impact Cratering	9
2.1 Crater Morphology	9
2.2 Impact Cratering	11
2.3 Modeling Impacts	17
3 Tsunamis	21
3.1 Physics of Water Waves–Tsunamis	23
3.2 Sources of Tsunamis	27
3.3 On Modeling Tsunami Waves	38
4 Numerical and Computational Methods	41
4.1 Finite Difference Method	41
4.2 Time and Space Discretization for the Wave Propagation Problem	44
4.3 Boundary Conditions and the Computational Domain	47
4.4 Runup	49
4.5 Validation of the Wave Propagation Model	51
5 Experiments in Modeling Impacts and Wave Propagation	55
5.1 Varying Water Depth to Investigate the Influence on the Charac- teristics of the Rim Wave	56
5.2 Bathymetric Variations affecting Tsunami Wave Propagation	65
5.3 Comparison of Wave Evolution over linear and "real" Bathymetries	69

6	Outline of Some Geological Implications from Modeling Impacts and Wave Propagation	73
6.1	Additional Modification of the Crater Cavity	74
6.2	Crater Filling after the Chicxulub Impact Event	77
6.3	Erosion, Transport, Sedimentation along a Tsunami Wave Train .	79
7	Summary and Outlook	83
	References	85
	Danksagung	93

List of Figures

1.1	Hollow of the Deep–Sea	1
1.2	1964 Alaskan Tsunami: left Whittier bay; right Seward Bay.	2
1.3	Craters on the Moon	4
1.4	Distribution of impact craters on Earth	5
2.1	(a) Simple and complex crater, (b) Moltke Crater on Moon , (c) geological cross section of the Meteor Crater	10
2.2	Snapshots of the contact– and compression stage.	12
2.3	Geometry of the excavation flow.	14
2.4	Generation of simple craters.	16
2.5	Geometries used in SALE	17
2.6	A time step in SALE	19
3.1	Distribution of Tsunami Events	22
3.2	Definition of wave parameter	23
3.3	Wave types: (a) deep, (b) intermediate deep, and (c) shallow water waves	25
3.4	Different shape of tsunami waves	26
3.5	Simple model for an earthquake as tsunami sources	29
3.6	Definitions of important parameters of an earthquake and a surface elevation due to an earthquake	30
3.7	Simple slide model	31
3.8	Model for complex slides according to Ward and Day (2002)	33
3.9	Generation of tsunami waves by oceanic impacts	35
3.10	Free oscillations caused by an impact into deep water	37
3.11	Wave gauges at certain distances from the impact point	37
4.1	Derivatives and their approximations	42

4.2	Different numerical approximations	44
4.3	Transition between the SALE hydrocode and the wave propagation	48
4.4	Structure of the computational domain.	49
4.5	Shoreline computations in MOST	50
4.6	Verification between MOST and ND-WP	51
4.7	1/r relationship of the wave propagation & verification of MOST	52
5.1	Measurement of wave characteristics	57
5.2	Time series of the gauge points recording the wave elevation	58
5.3	Wave amplitude as a function of the water depth	59
5.4	Wave period	61
5.5	Theoretical characteristics of the rim wave.	63
5.6	The collapse wave problem	64
5.7	Varying angle of slope	66
5.8	Times series based on a varying angle of slope	67
5.9	Log-log plot of the data for different angles of slope	68
5.10	Left: a real bathymetry. Right: linear bathymetry	69
5.11	Maximum wave elevation as a function of the location	70
5.12	Runup along the coast.	71
6.1	Simplified Hjulström-Sundborg diagram	74
6.2	Illustrating the surge of water back into the crater	75
6.3	Extended Hjulström-Sundborg diagram	76
6.4	Gravitational anomaly of the Chicxulub crater and a core picture of the K/T transition	78
6.5	Dynamic range of the velocity along the tsunami wave train	80

Abstract

The modeling of generation, propagation and runup of impact-generated tsunami waves give insights into the generation mechanisms of those waves by oceanic impacts and their evolution during the propagation and runup. The SALE hydro-code is used to compute the impact cratering. A new developed 2D propagation model for tsunami waves is applied to simulate the wave propagation of impact-generated tsunami. This model is based on dispersive and non-dispersive equations. To combine the SALE code to the wave propagation model, a transition is established as the mean step. The impact is transferred to the wave propagation model along a circle because SALE only simulates vertical impacts. With the help of model strategy, two different classes of tsunami wave caused by oceanic impacts could be identified: the rim wave and the collapse wave. The generation mechanisms are profoundly different. While the rim wave is generated by the collapsing crater rim of water, the collapse wave is the result of the collapsing central peak. Applying these wave classes, three different oceanic impacts in terms of the water depth could be defined: impact into deep, intermediate and shallow water. Only considering the SALE code, the characteristics of the rim wave is investigated. While a linear analysis of the wave height of this wave succeeds, it fails for the wave period. With the help of the wave propagation code, the influence of the angle of the slope of a platform is investigated. The difference between the obtuse angle (1:10) and acute angle (1:90) is appr. 1 m in the wave propagation; but this difference might become important during the shoaling while wave height is multiplied by up to 6 times. The comparison between a linear bathymetry and a real one, both containing similar geometrical features, results that the influence on the wave propagation is weak, but becomes strong during the runup. In case of the real bathymetry, the course of the runup is more complex than in case of the linear one. In addition, from the modeling impact and the tsunami wave propagation, qualitative geological implications can be drawn: (a) The surge of

water back into the crater is powerful enough to erode large fractions of the crater rim and transport them into the crater cavity. (b) The sedimentary system along a tsunami wave train is only in erosional conditions, implying that tsunami deposits might be identified by a erosional surface below the storm wave base. (c) In case of the Chicxulub impact, the crater rim was high enough to prevent a powerful surge of water into the crater cavity.

Keywords: Impact-generated tsunami waves, impact cratering, tsunami wave evolution, shallow water equations, Boussinesq equations

Zusammenfassung

Die Modellierung von Bildung, Fortpflanzung und Auflaufen von impakt-generierten Tsunami-Wellen gibt Einsichten in die Bildungsmechanismen dieser Wellen durch ozeanische Einschläge, ihre Fortpflanzung und ihr Auflaufen. Der SALE hydrocode wurde verwendet, um die Impaktprozesse zu simulieren. Ein neuentwickeltes 2D Fortpflanzungsmodell wird benutzt um die Fortpflanzung der Tsunamiwellen zu simulieren. Es basiert auf dispersiven und nicht-dispersiven Gleichungen. Um den SALE code und das Wellenmodell miteinander zu verbinden, wurde als Zwischenschritt eine Übergabe entwickelt. Der Impakt wird entlang eines Kreises an das Wellenmodell übergeben. Das ist möglich, da SALE nur vertikale Einschläge berechnen kann. Mit diesen beiden Modellen konnten zwei Klassen von Tsunamiwellen identifiziert werden: die Randwelle und die Kollaps-welle. Die Bildungsmechanismen beider Wellen sind sehr unterschiedlich. Während die Randwellen durch den Kollaps des Kraterrandes des Wassers entsteht, bildet sich die Kollapswelle durch den Kollaps des zentralen Hochs des Wassers. Durch die Anwendung dieser Klassen konnten drei verschiedene Einschläge bezüglich der Wassertiefe definiert werden: Impakt in tiefes, in mittel-tiefes und flaches Wasser. Die Charakteristik der Randwelle wurde mit Hilfe des SALE codes untersucht. Eine lineare Analyse der gewonnenen Daten gelang für die Wellenhöhe der Randwelle, missglückte allerdings für ihre Periode. Ein weiteres Experiment ist die Untersuchung der Abhängigkeit der Wellenhöhe von dem Hangwinkel einer Plattform. Der Unterschied zwischen dem stumpfen Winkel (1:10) und dem spitzen Winkel (1:90) war ca. 1 m. Aber dieser Unterschied wird wichtig, wenn durch die Annäherung an den Strand, die Wellenhöhe sich bis zu versechsfacht. Der Vergleich in der Wellenevolution über einer linearen und einer realen Bathymetrie, mit ähnlichen geometrischen Eigenschaften, zeigte, dass der Einfluss des Winkel auf die Evolution relativ schwach ist. Dieser wird jedoch stark während des Auflaufens der Tsunamiwelle. Im Falle der realen Bathymetrie ist der Verlauf

der Auflaufkurve komplexer als im Falle der linearen Bathymetrie. Zusätzlich können aus der Modellierung qualitativ geologische Informationen gezogen werden: (a) Der Rückstrom des Wassers in den Krater ist kräftig genug, dass große Teile des Kraterrandes erodiert und in den Krater transportiert werden. (b) Entlang eines Tsunamiwellenzuges wird ausschliesslich Material erodiert. Diese Tatsache führt zur Annahme, dass Tsunamiablagerungen anhand einer Erosionsoberfläche unterhalb der Sturmwellenbasis identifiziert werden könnten. (c) Im Falle des Chicxulub Einschlages war der Kraterrand hoch genug, um des Rückstrom des Wassers in die Kraterstruktur zu verhindern.

Schlüsselworte: Impakt-generierte Tsunamiwellen, impact cratering, Evolution von Tsunamiwellen, Flachwasser-Gleichungen, Boussinesq Gleichungen

Chapter 1

Background, Aims and Methods

The term **Tsunami** is derived from the Japanese word *tsun ami*, meaning harbor wave. Fig. 1.1 shows an artwork of Katsushika Hokusai, circa 1831 (Hollow Deep Wave), illustrating destructive consequences of a tsunami wave.

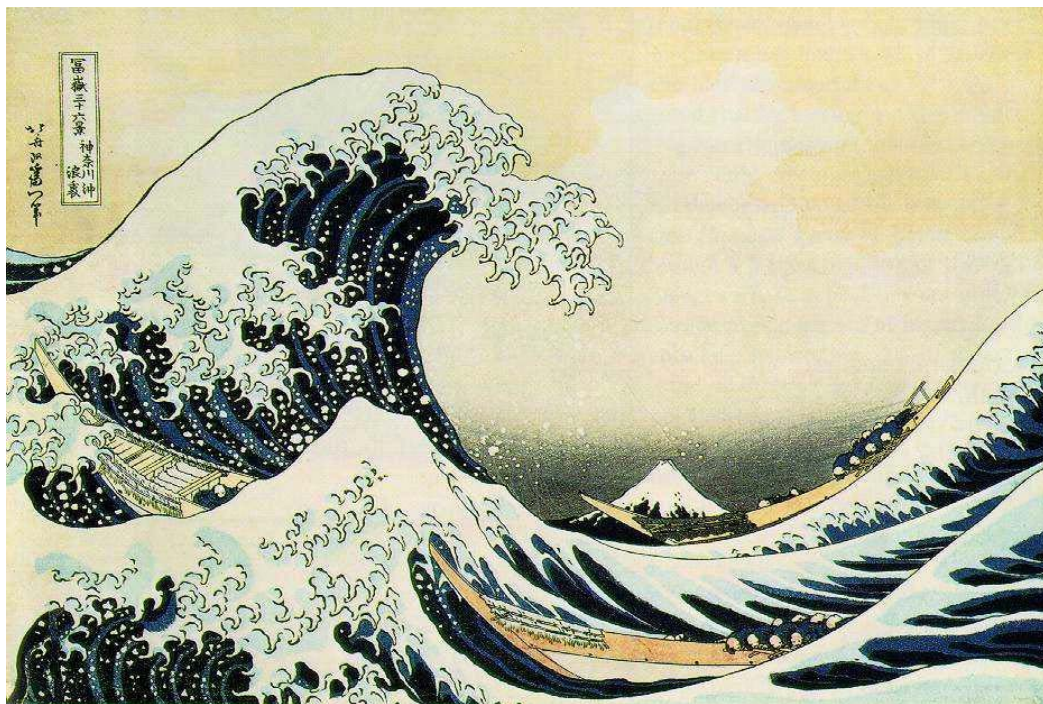


Figure 1.1: Print of the color woodcut, No. 20 from the series 'Thirty-Six Views of Fuji' (ca. 1831), showing the *Hollow of the Deep-Sea Wave*. Many websites and textbooks about tsunami waves depict this artwork as a tsunami wave, but it is a wind-generated wave (Bryant, 2001).

But in fact this picture shows a wind-generated wave and not a tsunami. **Tsunami waves** are waves in water bodies, which differ in their characteristics, e.g. in wavelength, wave period and velocity, from other water waves due to their generation mechanisms. Normal mode water waves are generally induced by the interaction between the water surface and the wind. In contrast, tsunami waves are commonly generated during earthquakes, submarine slides, or oceanic impacts. The list of different sources makes clear that tsunami waves may theoretically occur in oceans, lakes, reservoirs, or in any water body. The main feature of tsunami waves in the open sea is the wave length which is very long compared to normal mode waves. The amplitude of the tsunami waves is comparatively small. The travel velocity can reach about 600 km/h. However, the amplitude increases extremely when these waves propagate in shallower water. Their velocity and wavelength decrease during the so-called shoaling, meaning the process of waves coming ashore. Nevertheless, the increased amplitude of the waves may cause severe destruction in the coastal areas (Fig. 1.2).

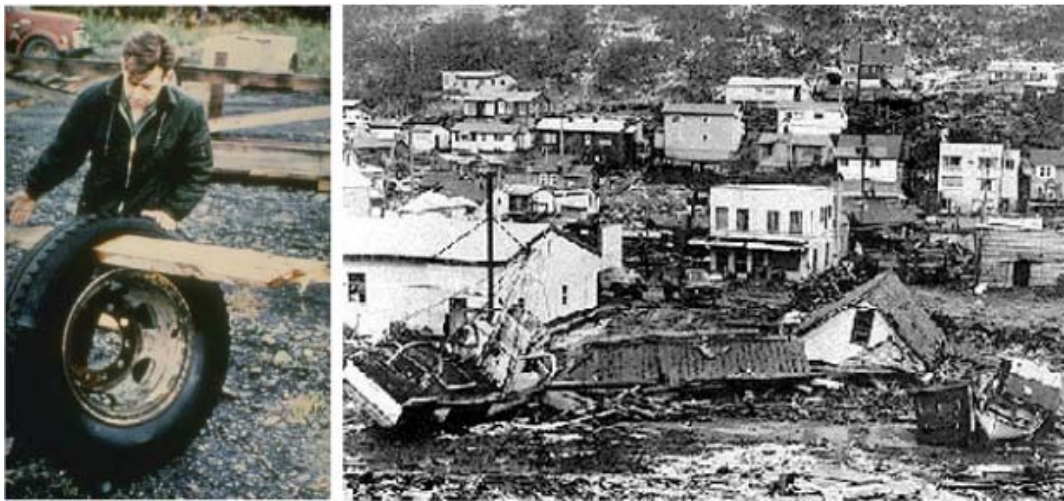


Figure 1.2: The destruction is caused by inundating tsunami waves. As the source the $M=8.4$ earthquake on March 29, 1964 with the epicenter in the area of Prince William Sound, Alaska, was determined. The left picture displays the destruction power in the Whittier Bay. The runup of tsunami was here 30–40 ft (9.1 m to 12.1 m). The right photo illustrates destruction further south in the Seward Bay. In this bay the runup was also measured at 30–40 feet (Dudley and Lee, 1998).

The source for the 1964 Alaska tsunami (Fig.1.2) was an $M=8.4$ earthquake with the epicenter in the area of Prince William Sound, Alaska. Owing to earthquakes around the Pacific, a total of 462,597 deaths has been attributed to tsunami waves for the last 2000 years (Bryant, 2001). Hence in this region, tsunami waves are a serious natural hazard.

Land or submarine slides are the second source of tsunami waves. These slides may also produce tsunami waves with destructive consequences for coastal areas. The Papua New Guinean Tsunami 1998 demonstrates the lethal power of a slide-induced tsunami wave. An earthquake at 08:49:15 GMT on July 17, 1998 in the area of Aitape, located at the north central coast of Papua New Guinea, generated a submarine slide. The tsunami due to this slide caused the death of 3,000 people at the north coast of Papua New Guinea. The wave climbed up to 10 m above the sea level.

A third source of tsunami waves is the occurrence of meteoritic impacts into oceanic environments. Their relative frequency is very low compared to submarine earthquakes and slides, but consequences for surrounding coastal areas might be even more destructive. Independent of the diameter of the impactor and its velocity, an impact represents a sudden supply of energy to the Earth. Obviously, different systems respond in different manners to this energy supply.

Independent of the water depth, a meteoritic impact always produces tsunami waves. Near to the impact site, their importance as a key parameter for the environmental system is low compared to the environmental consequences of the impact cratering. The relative importance of tsunami waves increases with the distance to the impact area. The initial amplitude of impact-generated tsunami waves depends on the size of the impactor and the pre-impact water depth. In addition to the initial wave height, the amplitude of an impact-generated tsunami during the propagation over the open sea depends also on the local bathymetry. The superposition of local effects along the wave train of a tsunami determines the overall evolution and the coastal inundation caused a tsunami wave. **The tsunami waves, investigated in this thesis, are generated by oceanic impacts.** Fortunately, there are no recent examples available. Ancient evidences for oceanic impacts and their tsunamis are very rare.

Besides the generation and propagation of tsunami waves, runup is important process of a tsunami wave. During the propagation over the open ocean, the wavelength can be several 10's- to 100's of kilometers, however the wave height is comparatively small. The actual risk of a tsunami wave is the shoaling ef-

fect where the wave amplitude rises as the wavelength decreases. The risk exists because very important structures like harbors, industries and settlements are located in these areas and are, in case of the harbors, key points of the relationships between different countries and different continents. The main evidences of tsunami waves in the geological history are vast re-distributions of sediments in coastal areas.

As already mentioned, the sources of tsunami waves, considered in this study, are oceanic impacts. However impacts, not only oceanic ones, definitely have general meaning for the **history of our planet and planetary system** as they accompany the formation and early phases of planetary bodies. Especially in the early history of our planetary system between 4.6 and 3.9 Billion years ago, those impacts were 100 times more frequent than they have been ever since. Obvious traces of such impacts are crater structures, observable on Earth and other planetary bodies like the Moon (Fig. 1.3) and Mars. Fig. 1.3 displays

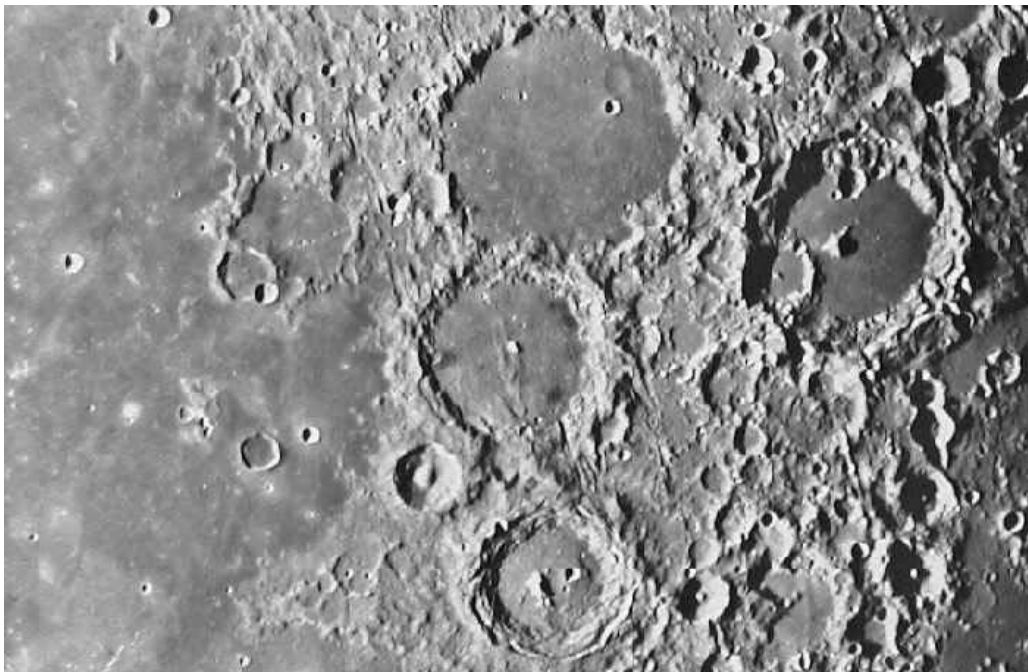


Figure 1.3: Picture of the craters Ptolemaeus, Alphonsus, Arzachel and Albategnius on Moon (<http://www.moon-phases.com/moon-pictures/11.html>).

impact craters of varying diameters on the Moon. Looking at the surface of the Earth (Fig. 1.4), impact craters are much less common than on the Moon. A total of 170 craters on the Earth have been confirmed as impact structures

(Grieve et al., 1981; Gersonde et al., 2002; Abels et al., 2002). The dots and circles in Fig 1.4 represent impacts that were recognized until 2000.

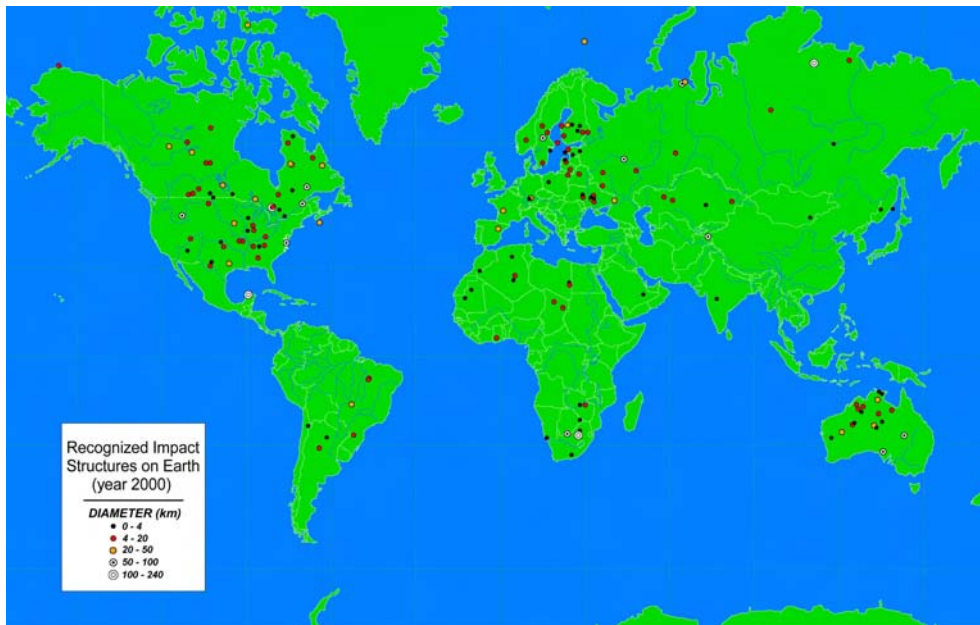


Figure 1.4: Distribution of impact craters known on Earth (<http://www.lpi.usra.edu/publications/slidesets/craters/craterindex.shtml>, 2000)

Only 27 impact structures with evidence of/for an impact in a marine environment have been identified (Grieve et al., 1981; Gersonde et al., 2002; Abels et al., 2002). Since two thirds of the Earth's surface is covered by water, the probability of marine impacts is greater than that of impacts on continents.

However, the distribution of continental and marine impacts tells a completely different story. Glikson (1999) estimated a total of 8,104 marine craters larger than 20 km that have been formed during the Earth's history. The apparent gap between the number of known impact structures and the estimated quantity (Glikson, 1999), and the imbalance of the spatial distribution of known marine and continental impact craters can be ascribed to: (i) the coarse resolution of investigated marine basins, (ii) plate tectonic destruction of oceanic crusts, (iii) long-term erosional and depositional processes that have changed the surface of the Earth, and as we will see later, (iv) small meteorites do not always generate impact craters in the oceanic crust.

A thorough description of the general physics of impact cratering is given

by Melosh (1989). The knowledge of impact craters in oceans and the environmental perturbations is based on numerical experiments by Strelitz (1979), Nordyke (1977), Sonett et al. (1991), O’Keefe and Ahrens (1982), Melosh (1989), Gault and Sonett (1982), van der Bergh (1989), Wünnemann and Lange (2002) and Weisz et al. (2003). Those experiments were mostly dedicated to the influence of the water column on the final impact crater. However, Weisz et al. (2003) have been focusing on the generation of tsunami waves during oceanic impacts, too. (With Weisz et al. (2003), parts of the thesis have already been published.) Impactors may hit continental shelves, where the water is shallower as well as deep sea basins. Independent of the water depth, kinetic energy is transferred to the water column resulting in strong water movements. These water movements cause the generation of tsunami waves.

The aim of the presented study is the investigation of generation mechanisms of tsunami waves caused by oceanic impacts, and the propagation, including runup, of these waves. Compared with earthquakes and submarine slides as sources for tsunamis, less research has focused on the understanding of generation process of tsunami waves during oceanic impacts. The investigation of impact-induced tsunami waves involves impact simulations to define the initial conditions for the wave propagation. By means of these impact simulations, the following two questions can be answered: *How are tsunami waves generated by oceanic impacts? In which way does the water depth influence characteristics of the initial tsunami wave?*

As already outlined, the amplitude of tsunami waves depends on the local bathymetry. Assuming linearly-changing bathymetries, the modeling of wave propagation, based on changing angle of slope, implies: *How do bathymetric changes (e.g. angle of the platform slope) influence the global evolution of a tsunami wave?*

The **complete model strategy**, consisting of modeling generation and propagation (including runup) of a tsunami wave by oceanic impacts, is **applied to an artificial bathymetry and a real one**. Comparison of the results gives insights into the influence of realistically varying water depth. Finally, **sedimentologic informations will be drawn from the modeling of impacts and the tsunami wave propagation**. In this context, those information are **linked to the Chicxulub impact crater**.

Methods and Devices. To understand the generation mechanisms of impact-generated tsunami waves, only numerical modeling of impacts into marine environment is an approach. The SALE hydrocode (for more detailed information on this code, see section 2.3) is still under development, but in its newest release *SALE-3MAT* it represents an appropriate tool to investigate oceanic impacts. The propagation of tsunami waves is another aspect of this thesis.

The development of a 2D wave propagation model, based on non-dispersive and dispersive equations is a main issue. The MOST code (Method of Splitting Tsunami) was established by (Titov and Synolakis, 1995, 1998) used in this thesis to simulate propagation and the runup of tsunami waves in coastal areas.

The development of a new wave propagation model is necessary because the dispersive wave models that are available only run on multi CPU clusters and are programmed in a massively parallel style. For this study, a single CPU PC with LINUX and a PowerMac G5 were available. This limitation in the computational power is responsible for the limitations which are outlined later in the text.

This **thesis is part of a project** concerning the sediments around the Gulf of Mexico which are connected to the Chicxulub impact event, 65 Ma ago. These sediments are made up of sandy deposits with sedimentary structures indicating a highly dynamical system. Three possible generation hypothesis of these sediments are discussed in the literature: (i) turbidity current (Bohor, 1996), (ii) sea-level variations (Stinnesbeck and Keller, 1996), and (iii) tsunami wave (Bourgeois et al., 1988; Smit, 1999; Smit et al., 1996). From a sedimentologic point of view, the tsunami hypothesis appears to be most likely. Assuming such a mechanism, Bourgeois et al. (1988) estimated the wave heights of a possible tsunami to approx. 300 m, based on a comparison of the pre-tsunami water depth and the expected water depth according to the depositional features of the sediments. Such an estimation gives unrealistically high values since Bourgeois et al. (1988) did not take different types of waves into account. Therefore, 300 m are very speculative. Bahlburg (supervisor of this thesis; Bahlburg and Claeys, 1999) visited outcrops containing these sediments. His first question was whether is it possible to have such great wave height in the coastal area or not? His ad-hoc question results in the final issue of the whole project: How are tsunami deposits generated? This thesis is not able to give an answer to this final question. While trying to find an answer to this question, other questions of more general relevance arose which are given in *aims*. Hence, this thesis can only contribute to find an answer to the final question, but it investigates problems that are important

steps for that goal.

Chapter 2

Impacts and Impact Cratering

With a look at our solar system, we can see that impact structures are an obvious feature of the surface of other planets and planetary bodies. These structures are evidence of a dynamical history of our solar system and universe, being observable on the Earth and the Moon as well. The morphology of those impact structures differs in several aspects among each other. This chapter aims at giving a general summary about impact craters and their generation. For a more detailed description of impact cratering, see e.g. Melosh (1989) and Wünnemann (2001).

2.1 Crater Morphology

By means of modeling and observations of impact structures, two different kinds of impact morphologies can be distinguished: simple and complex craters. The transition between both morphologies is mainly due to the gravity of the target's surface; but also its structure and material properties have secondary influence (Melosh, 1989; Turtle et al., 2005). Here only the simple craters will further be described. The introduction into the generation of complex craters requires a more detailed description of processes during impact cratering. A general overview on the differences between both crater morphologies is given by Fig. 2.1a. Simple craters are commonly small craters with a simple bowl-shaped form (Fig. 2.1b). As an example of a simple crater, the Moltke crater on the Moon (Fig. 2.1a) is preserved in a pristine morphology. No further modification, like erosion, has taken place.

On the Earth, the Meteor crater in Arizona is an analogous example. Its shape has been changing since its generation during the crater structure is exposed on

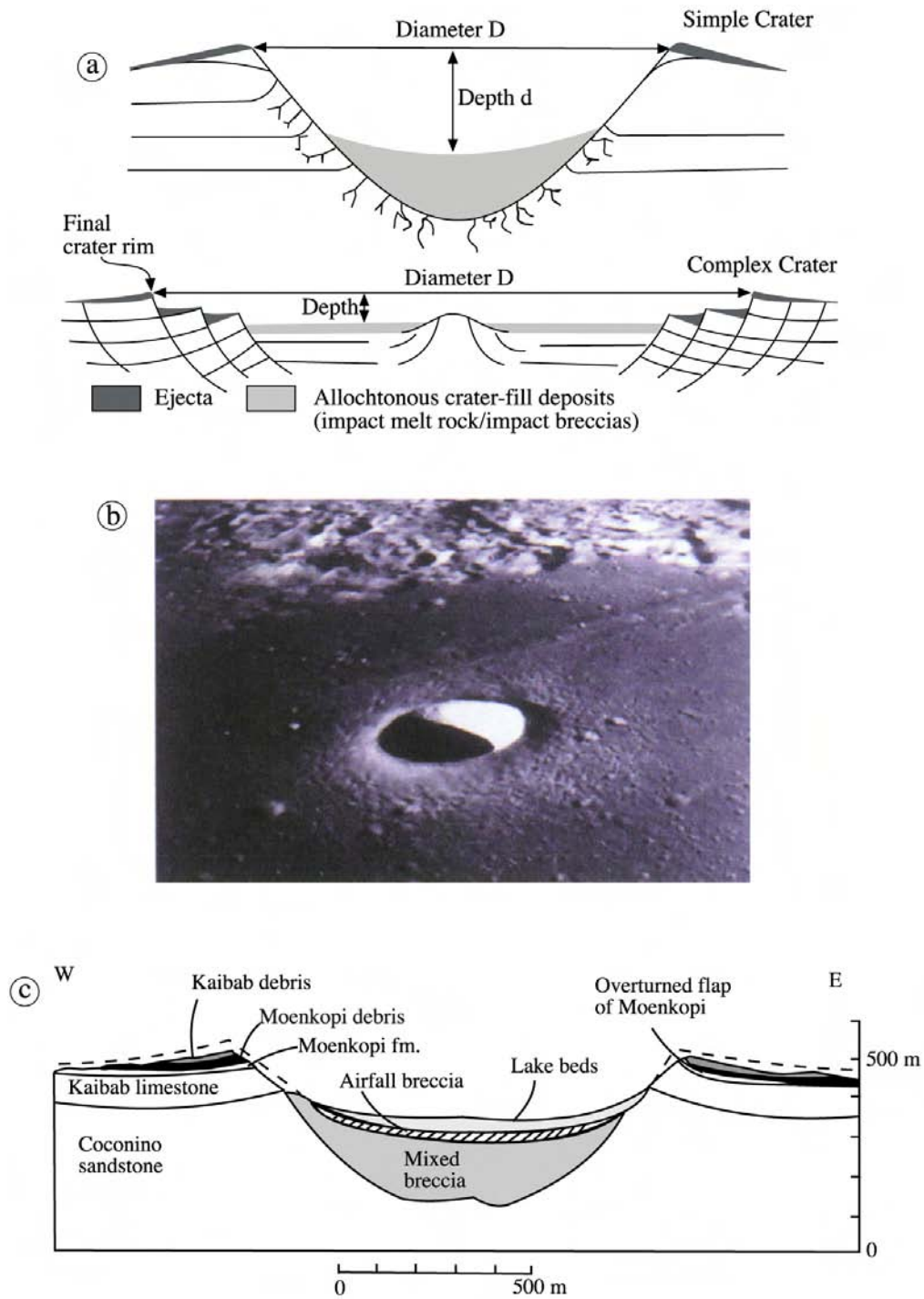


Figure 2.1: (a) Principal comparison in the structure of simple and complex crater morphologies (Redrawn from Kai Wünnemann according to Melosh, 1989). (b) The Moltke Crater on the Moon shows an almost perfect bowl-shaped form. It is 7 km in diameter (Apollo Mission 10, As10-29-4324). (c) gives a simplified geology of the Meteor crater (Shoemaker, 1960). For further information, see text.

the surface (Shoemaker, 1960). In Fig. 2.1c, the dashed line represents the reconstructed original crater shape. Erosional forces have been working on this crater for the last 50,000 years and have changed its shape. In the Meteor crater, Pleistocene lake beds and Holocene slope-wash deposits also occur. The crater cavity was formed in a sequence of Paleozoic rocks, consisting of the Moenkopi sandstone, Kaibab limestone and the Coconino sandstone. The latter is not completely penetrated. The younger Pleistocene lake beds are underlain by a breccia approx. 150 m thick. This breccia consists of shattered blocks of the Coconino sandstone and meteoritic material. The meteoritic material occurs in fine spherules.

2.2 Impact Cratering

Gault et al. (1968) subdivided the process of impacting (also known as impact cratering) into three stages. These stages take the juxtaposition of mechanical and thermo-dynamical processes into account. They are: (i) Contact- and Compression stage, (ii) Excavation stage, and (iii) Modification stage. It means that the stages should not be understood as discrete conditions, but as a continuous conglomerate of physical processes. Before a body can penetrate into the solid Earth or into oceanic environments, it has to travel through the atmosphere. An impact technically begins when the meteorite enters the atmosphere. During travel through the atmosphere, it loses kinetic energy owing to an interaction with the atmospheric components. During interaction, the atmosphere is extremely heated up, which may change the chemical composition of atmosphere around the moving body. Depending on the structural and chemical composition of the body, it is possible that it explodes, burns out or is de-accelerated up to the respective "fall velocity" (Ivanov et al., 1997; Chyba et al., 1993; Lyne et al., 1996) which means a gravity controlled vertical velocity.. Bodies which fall with "fall velocity" onto the Earth are so-called *meteorites*.

Contact- and Compression Stage

The contact- and compression stage begins when the impactor touches the surface of the target. The normal velocities of bodies, which lead to the formation of craters, are between 11 km/s and 73 km/s (Haymes, 1971).

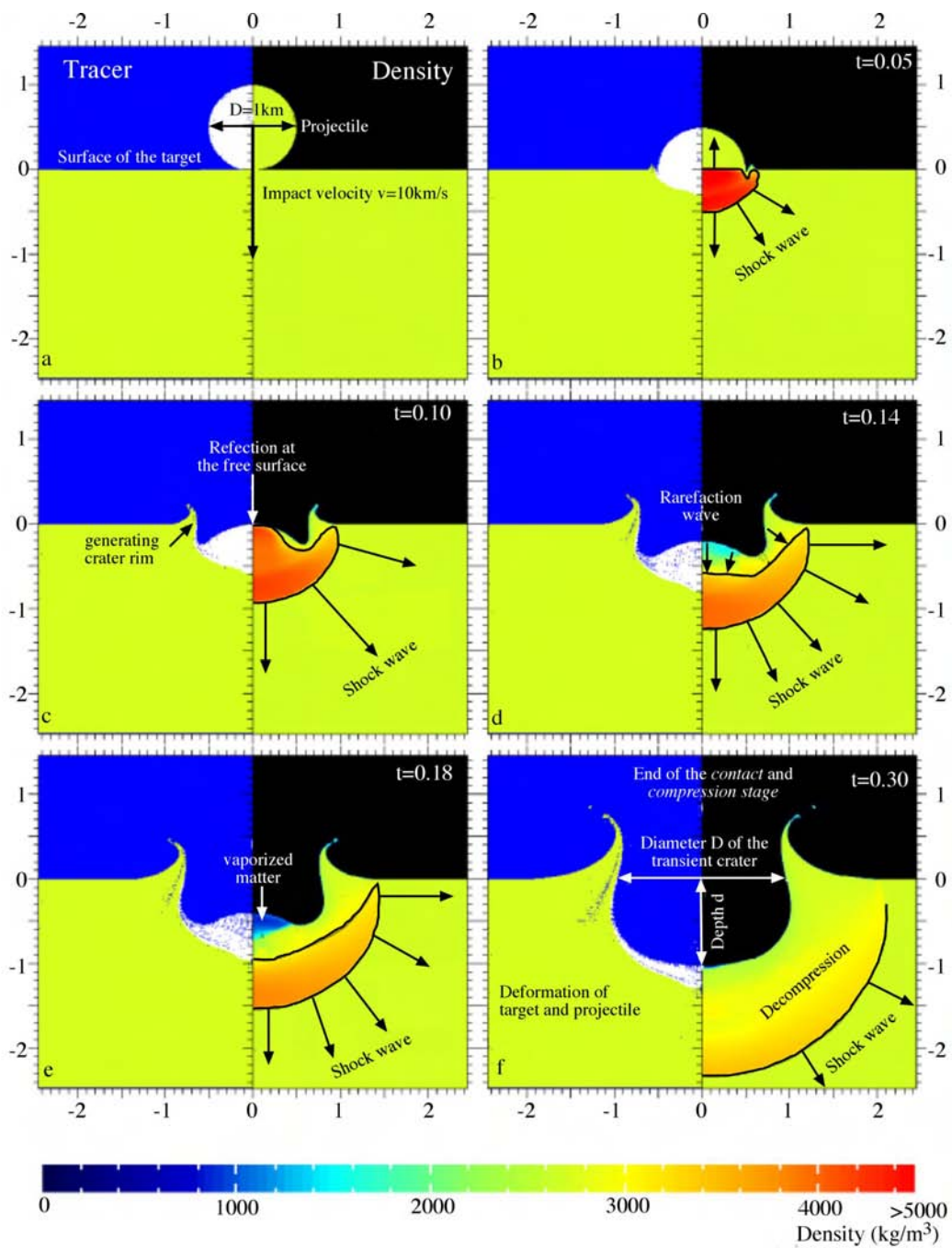


Figure 2.2: Snapshots of the contact and compression stage. The right hand side of each snapshot displays the density and the left side hand shows the tracer. The scale is in km (Wünnemann, 2001).

The average on Earth is approximately 18–20 km/s and on the Moon 14–

15 km/s (O’Keefe and Ahrens, 1994). Fig. 2.7a–f display 6 snapshots of the contact– and compression stage (Wünnemann, 2001). During the penetration of the impactor into the target, the target material is accelerated almost up to the velocity of the original impact velocity, and simultaneously the velocity of the impactor decreases. In this way, the target and the impactor is in compression. This is a non–isentropic compression of matter which is also known as shock wave compression. This shock wave is induced in the direction of the impact and backwards in the projectile.

Depending essentially on the impact velocity, pressures in the shock wave of several 100 GPa are obtained, which is much larger than the yield strength Y of solid matter. Under these conditions, solid materials behave like fluids. As a consequence, plastic deformation of the target occurs when the crater cavity begins to form. The projectile is mashed and fits more and more the curvature of the cavity (Fig. 2.7b–f). The shock wave, traveling against the impact direction reaches the free surface of the projectile and is reflected on it, resulting in phase change and a decompression. This wave is now known as *Rarereaction wave*. Therefore, the engulfed material is molten, vaporized or strongly shattered (Fig. 2.7d–e).

The contact– and compression stage ends when the projectile is unloaded from pressure. Usually, the projectile is completely vaporized during this first stage (Melosh, 1989). Among the other stages, the contact– and compression stage is the shortest one. For 10 m diameter projectile with an impact velocity of 10 m/s and a siliciclastic target this stage lasts $\approx 2.5 \cdot 10^{-3} s$ (Wünnemann, 2001). For a 1 km diameter projectile it would last $\approx 2.5 \cdot 10^{-1} s$ (Melosh, 1989).

Excavation Stage

The excavation stage is characterized by two processes: (i) propagation and weakening of the shock wave, and (ii) formation of the excavation flow. The formation of the excavation flow is directly linked to the shock and rarefaction waves; both impart motion to the target material (Turtle et al., 2005), resulting in the initiation of the excavation flow. Fig. 2.3 schematically illustrates the flow field.

Initially, the flow is radial; however due to interactions with the free surface, an upward component is added to the velocity field. This is illustrated by the vector arrows in Fig. 2.3. It is demonstrated that material near the surface is driven upward and outward. Material from deeper parts of the cavity never reaches the

surface, while material located at the crater floor only moves downwards (Melosh, 1989). Some material rises above the preimpact surface; so it is defined to be ejected (Melosh, 1989). This ejected material, whose moving debris is loosely coupled, generates the *ejecta curtain*.

The result of the excavation flow is the transient crater. However, this term actually is a simplifying approach, because numerical experiments have shown that parts of the transient crater collapses while other parts, mostly deeper ones, are still excavating (Turtle et al., 2005). The excavation flow is retarded by inner

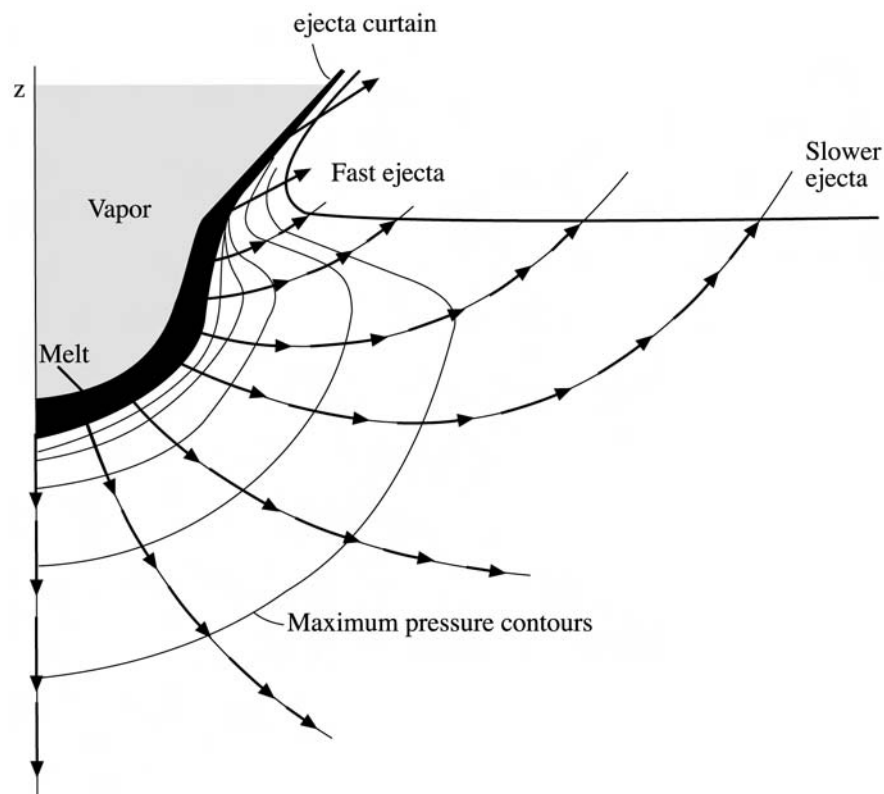


Figure 2.3: Geometry of the excavation flow field. Ejecta from near the impact site travels at high speed, while ejecta set in motion at larger distances travels at slower velocities (Melosh, 1989).

properties of the target (dry friction, cohesive strength retained in the target) and gravity (Melosh, 1989). It stops when there is insufficient energy to set adjacent material in motion. Owing to the inertia of the surrounding material, the excavation flow does not cease simultaneously in all directions (Melosh, 1989; Turtle et al., 2005). Indeed, the crater often continues to grow horizontally after

the vertical growth has stopped (Turtle et al., 2005).

If a water layer is involved in the cratering processes, the ejecta curtain may have a complex structure regarding the composition of different materials and their physical conditions. It is even possible that two ejecta curtains can be generated (Weisz et al., 2003) due to apparent differences in the material properties between water and crust.

Whereas the transition from the contact- and compression stage to the excavation stage is relatively sharp, the transition from the excavation stage to the modification stage cannot be defined as explicitly (Turtle et al., 2005); rather it is a overlap of processes in the later phase of the excavation and the early phase of the modification stage that belong to both stages.

Modification Stage

The transient crater is gravitationally unstable. Once the pressure decreases, material loses the ability to flow plastically. The viscosity increases and when the yield strength is exceeded, plastic deformation in terms of ductile material behavior is no longer possible. Instead the material starts to behave brittle or elastic, depending on the acting strain. The formation of the different types of craters (as phenomenologically described above) depends on the spatial extension of the transient crater. Assuming that the strength of planetary bodies is almost the same, the transient diameter D_t is a function of the gravity of the respective planetary body (see also sec. 2.1.2).

In the generation of simple craters, the yield strength is exceeded before the crater is gravitationally balanced which means that some parts of the transient crater are fragmented and can fall back into the crater. Fig. 2.4 illustrates the formation of simple craters. The bottom of the simple final crater is made up of breccia which moved down from the crater edge. In case of complex craters, the magnitude of modification is much larger. On Earth, if the depth of the crater is greater than 1 – 2 km, lithostatic inner pressure halts or blocks the excavation flow. The resulting crater cavity is gravitationally not stable. As a result, the bottom of the crater lifts up, and the edge or flank of the crater slides towards the center. The adjacent rocks are not able to resist the masses, resulting in the generation of series of normal faults.

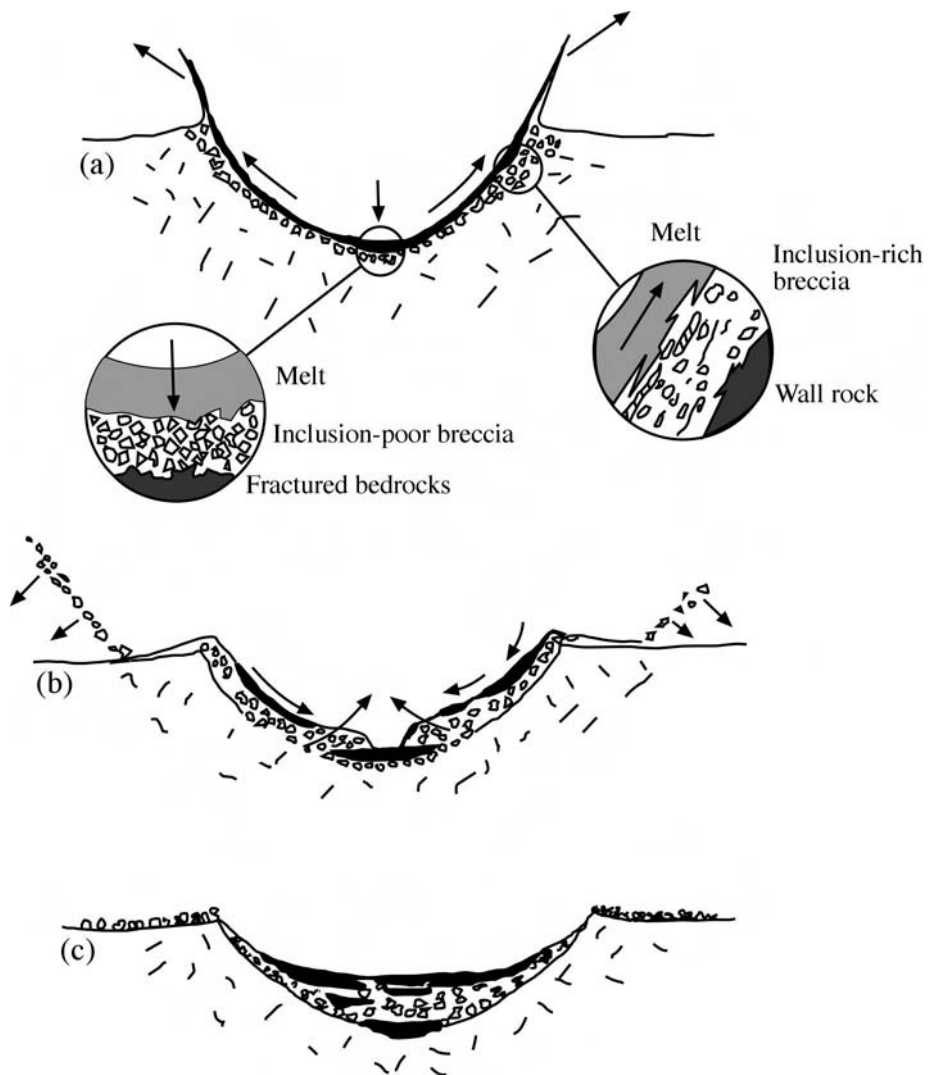


Figure 2.4: The generation of the simple craters. (a) represents the transient crater. (b) gives the collapse of the crater rim and (c) shows the final crater (Melosh, 1989).

2.3 Modeling Impacts

In order to compute the processes involved in impact cratering, the SALE hydrocode is used. SALE is the abbreviation for Simplified Arbitrary Lagrangian Eulerian. It was originally developed by Hirt et al. (1974) and Amsden et al. (1980). Essential improvements have been established by Kai Wünnemann in Wünnemann (2001) and Wünnemann and Lange (2002). The following description of the SALE hydrocode is based on Wünnemann (2001). In the text, it is not referred to this work, because the following description is taken from it. References that are given in Wünnemann's thesis are also given here.

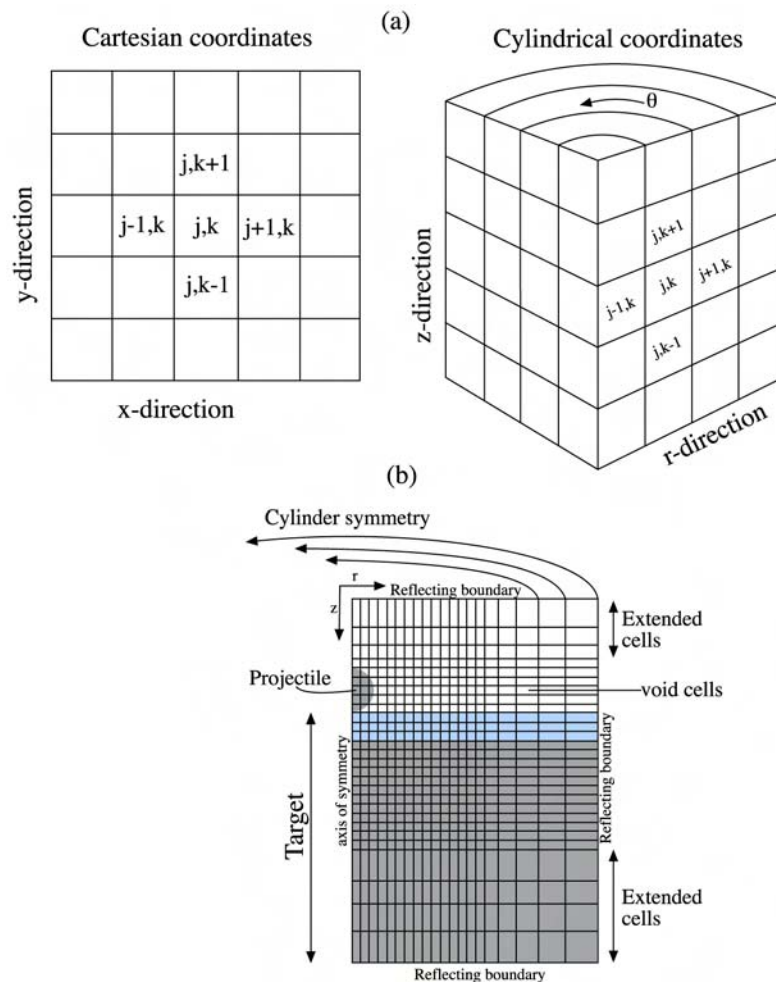


Figure 2.5: (a) Sketch of a cartesian and cylindrical coordinate system (Wünnemann, 2001). (b) The computational mesh with imbedded materials and boundary conditions (Wünnemann, 2001).

SALE is an explicit two-dimensional two-step finite difference algorithm. It is possible to choose between a cartesian and a cylindrical coordinate system as the basis for computations. Independent of the kind of the coordinate system, scalar parameters like pressure, density and internal energy are located in the center of a cell, while vectorial parameters are defined at the nodes. Fig. 2.5a gives the graphical representation of the possible coordinate system (Wünnemann, 2001). i and j denote the cell numbers in the horizontal and vertical direction. The initial positions of the bolide and the target, embedded into a cylindrical coordinate system depicts Fig, 2.5b. The equations used in this hydrocode are the conservation of mass, conservation of momentum, and the conservation of energy.

In the original SALE hydrocode, a time step comprises three subsequent steps.: (i) pure Lagrangian step to update the velocity field owing to the acting forces, (ii) the "SIMPLE" step which is a semi-implicit one. In this step, the pressure is corrected by the *Newton-Raphson iteration*; however in impact simulations, it is neglected. (iii) Calculation of the internal energy by using a transport equation of energy. In a pure Lagrangian mode, calculations within a time step were finished. In the Eulerian mode, the spatial change of energy, mass and momentum has to be re-calculated with a method given by Fig. 2.6. A time step ends with the update of the pressure.

In case of severe deformations, a pure Lagrangian mode would result in spurious results; therefore impact simulations are done in the Eulerian mode. Since in the Eulerian approach a infinitesimal part of the space is considered, the numerical modeling using an Eulerian mode is accompanied by artificial numerical diffusion along boundaries between different materials. To avoid this, the concept of internal boundaries is implemented. The procedure to establish internal boundaries between different materials or the determination of the free surface takes the volume fraction of each material in the actual cell and the adjacent ones and the mass fluxes among them into account. The concentration of masses in the actual and adjacent cells is of crucial importance. The newest release of Wünnemann's SALE hydrocode, referred to as *SALE-3MAT*, is now able to handle three different kinds of materials in one cell. In this case, two internal cells have to be constructed. This is, so far, the description of an hydrodynamical model. Impact cratering consists of a thermodynamic one, too.

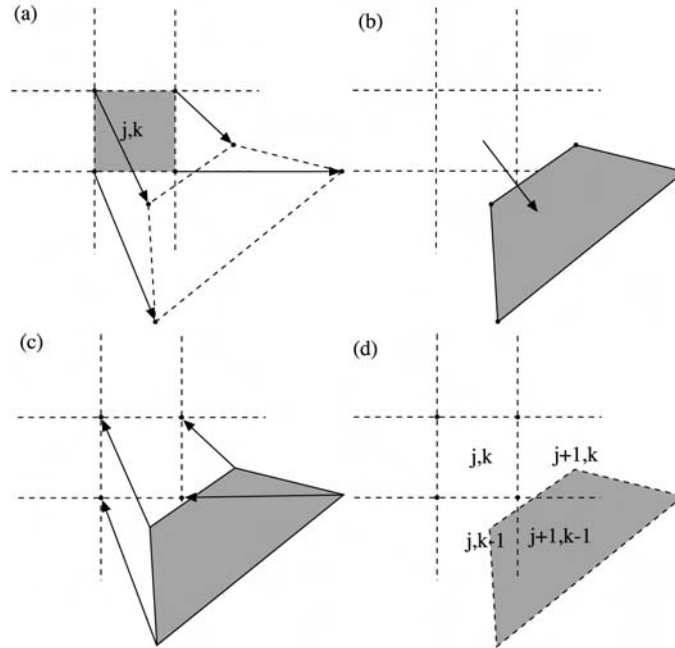


Figure 2.6: Illustration of the different steps within one time step of SALE. In (a) the nodes are relocated according to Lagrangian velocities. (b) depicts the resulting Lagrangian mesh. In (c), this cell is transformed to original location in space. (d) The mass, initially located in the cell (j,k) is now distributed over three adjacent cells (Wünnemann, 2001).

To compute the thermodynamic state of the material, the Analytical Equation Of States (ANEOS, Thompson and Lauson, 1972) for water and granite are used. Water is assumed to be purely hydrodynamic without any viscosity. In contrast, rocks behave plastically (ductile) only up to a certain yield point. Below the so-called plastic yield strength Y , rocks respond elastically to a given stress. The elastic failure of rock is calculated by the Von Mises yield criterion (Wilkins, 1964), whereas strength Y is a function of pressure and temperature ($Y = f(p, T)$). A more extended description of the constitutive equations is given in Wünnemann and Ivanov (2003).

All models in this thesis are carried out on a computational grid of cells in radial and vertical direction, respectively. A cylindrical geometric grid with the left boundary being the axial symmetry axis is applied. The two dimensional geometry constrains the model to vertical impacts only. To avoid any interfering reflections from the grid boundaries, the outer 100 cells in each direction (except the symmetry axis to the left) are interactively multiplied by 1.05 ($dx_{n+1} =$

$1.05 \cdot dx_n$, where dx is the cell size in one direction). Thus the spatial resolution is 25 m in the inner area in the vicinity of the point of impact and the maximum cell size at the boundary of the grid is approximately 800 m.

Chapter 3

Tsunamis

Tsunamis are a special type of water waves, propagating in the water column of oceans, lakes, bays and reservoirs. The term *tsunami* is Japanese and means harbor (*tsun*) wave (*ami*). Tsunamis possess a relatively small to moderate wave amplitude in deep waters. The length of these waves is long enough to be hardly noticeable in the deep sea, for instance in a fishing boat when the waves are passing by. However when the water depth is shoaling, the wave amplitude increases enormously in the same way as the wave length decreases. This chapter gives an introduction to the occurrence of tsunamis, their sources and the physics of the wave propagation and runup.

Tsunamis as a natural hazard are not homogeneously distributed along the shorelines of the Earth. Tab. 3.1 gives the locations of tsunami events in the world's oceans and seas and the statistical frequency. These numbers are based on event catalogues. The first record was made in 479 B.C. in the Mediterranean, (Bryant, 2001). Almost 2,000 years of continuously recorded tsunami events is accounted for. In China such a record extends back almost 4,000 years and in Japan almost 1,300 years. Records of tsunamis in other regions of the Earth are much younger. For example, tsunamis from Alaska have only been documented since 1,788 (Bryant, 2001). The Pacific Ocean region is most susceptible for tsunami waves in the world, where approximately 462,597 deaths have been attributed to tsunamis over the last 2,000 years.

Fig. 3.1 plots 1,274 observation of tsunamis reported along the coastlines of the Pacific Ocean. The size of the circles in figure corresponds to the number of observation per degree square of latitude and longitude. They represent, thus, a tsunami density. The plot clearly shows that a very high density affects the

Table 3.1: Percentage distribution of tsunami in the world's oceans and seas (Bryant, 1991).

Location	Percentage
Atlantic East Coast	1.6
Mediterranean	10.1
Bay of Benga	0.8
East Indie	20.3
Pacific Ocean	25.4
Japan–Russia	18.6
Pacific East Coast	8.9
Caribbean	13.8
Atlantic West Coast	0.4

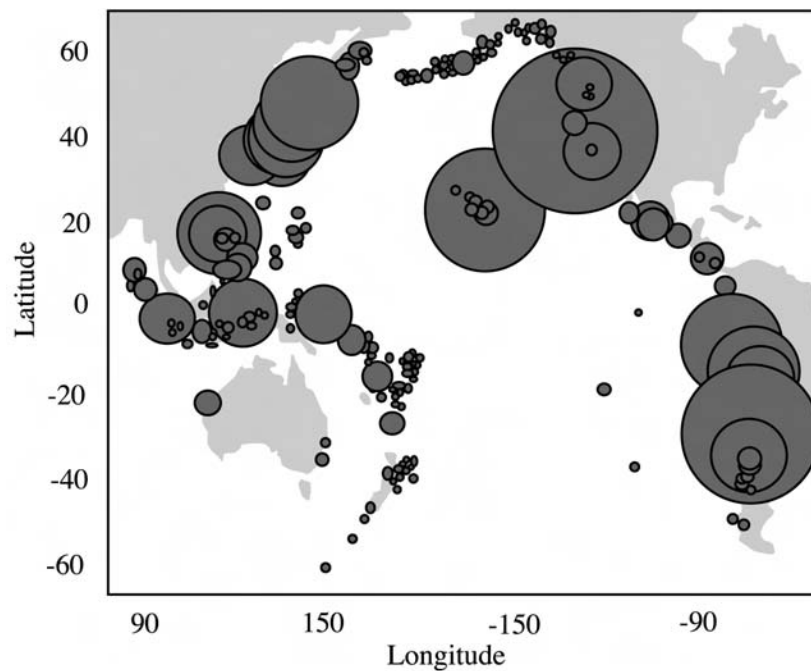


Figure 3.1: Location of 1,274 tsunamis since 47. B.C.. Size of circle increases proportional to number of events per degree square of latitude and longitude (Bryant, 2001).

coasts of the Western U.S.A. and Pacific coast of South-America.

3.1 Physics of Water Waves–Tsunamis

This section introduces the phenomenon of surface waves regarding different types of waves and their different characteristics. Assuming a sinusoidal wave-form in order to simplify the theory of surface waves, the wave displacement is a harmonic motion. Such a motion leads to a sinusoidal variation of the water level owing to the passing wave (Fig. 3.2). The lower axis in Fig. 3.2 represents a time series of the water level with time at a fixed point. The upper axis introduces general spatial parameters of waves. The vertical axis represents the displacement referring to vertical changes in height between the wave crest and the wave trough. Due to the fact, that the vertical displacement can be considered as the function of space and time (lower and upper axis), the displacement itself is a fixed instant in time or at a fixed point in space, varying between $+a$ (at the wave crest) and $-a$ (at the wave trough). Only taking the upper axis into account, the wavelength is the

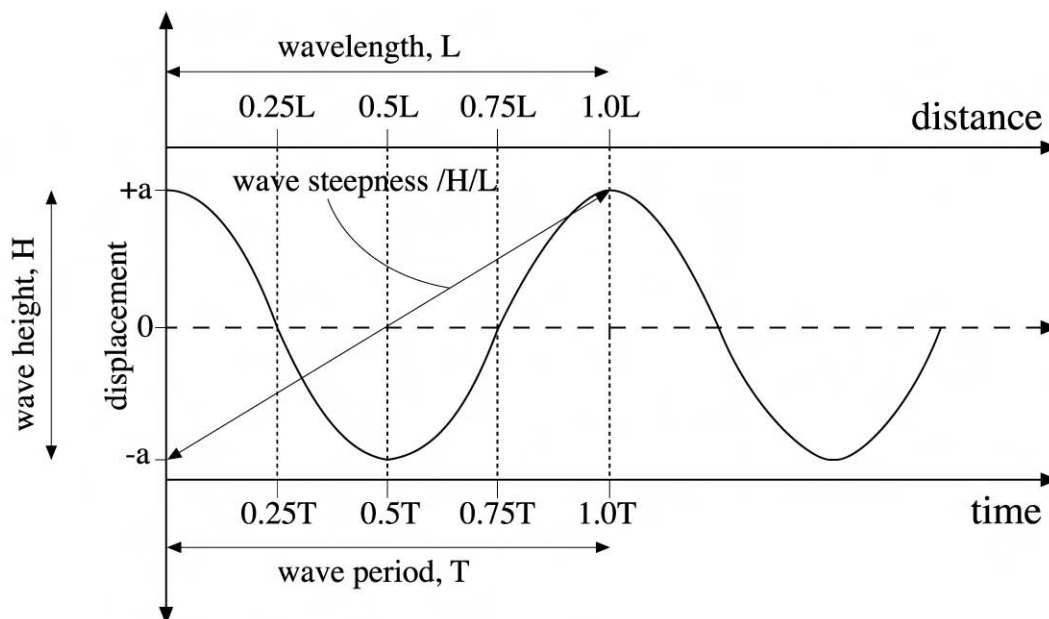


Figure 3.2: Using the upper axis, it displays the vertical profile of two successive idealized ocean waves, showing their linear dimensions and sinusoidal shape. Taking the lower axis into account, the displacement of an idealized wave at a fixed point, plotted against time, is given. The maximum and minimum displacement are recorded in fractions of the period T (Brown, 1999).

distance between successive crests (or troughs). The wave steepness is defined as the ratio between the wave height and its length. The period of a wave is the time interval between two successive crests (or troughs) passing a fixed point which is given by the lower axis in Fig. 3.2.

For further considerations, surface waves will be subdivided into three classes by the relation between the water depth and the wavelength: deep water, intermediate water and shallow water waves. Fig. 3.3a–c illustrates the motion of water particles that causes the propagation of surface waves. If the depth is larger than the half of the wavelength, waves are referred to as deep water waves. The water particles of this kind of wave move in an almost circular path (Fig. 3.3a). At the surface, the orbital diameter corresponds to the wave height. However, they exponentially decrease with depth. When the depth is roughly half of the wavelength, the orbital diameter is negligible, meaning no energy can be transferred to the bottom. This depth is also known as the wave base. Considering wave base, the wave heights of severe, ancient storms over a shallow water depth might roughly be estimated, if there are geological features of wave action left behind. If the water depth is between $L/20 < \text{depth} < L/2$, waves occur as intermediate water waves (Fig. 3.3b). The paths of the water particles show both a decrease in horizontal orbital diameter and a progressive flattening of the orbits near the sea-bed. If the water depth is less than $L/20$, waves are now referred to as shallow water waves, showing progressive flattening of the orbits near the sea-bed; but there is no decrease in the horizontal diameter, at all (Fig. 3.3c).

In general, speed is defined as: speed = distance/time. The same form of expression is valid for waves:

$$c = \frac{L}{T} = \sqrt{\frac{gL}{2\pi} \tanh\left(\frac{2\pi d}{L}\right)} \quad (3.1)$$

where d is the water depth. Since the wave period T can be expressed as a function of the wavelength L , the period can be substituted. Eq. 3.1 is a general equation in terms of the three different wave types and is mathematically referred to as the hyperbolic tangent. Further simplification can be derived for deep and shallow water waves that finalize to:

$$c = \sqrt{\frac{gL}{2\pi}} \quad \text{for deep water waves} \quad (3.2)$$

$$c = \sqrt{gd} \quad \text{for shallow water waves.} \quad (3.3)$$

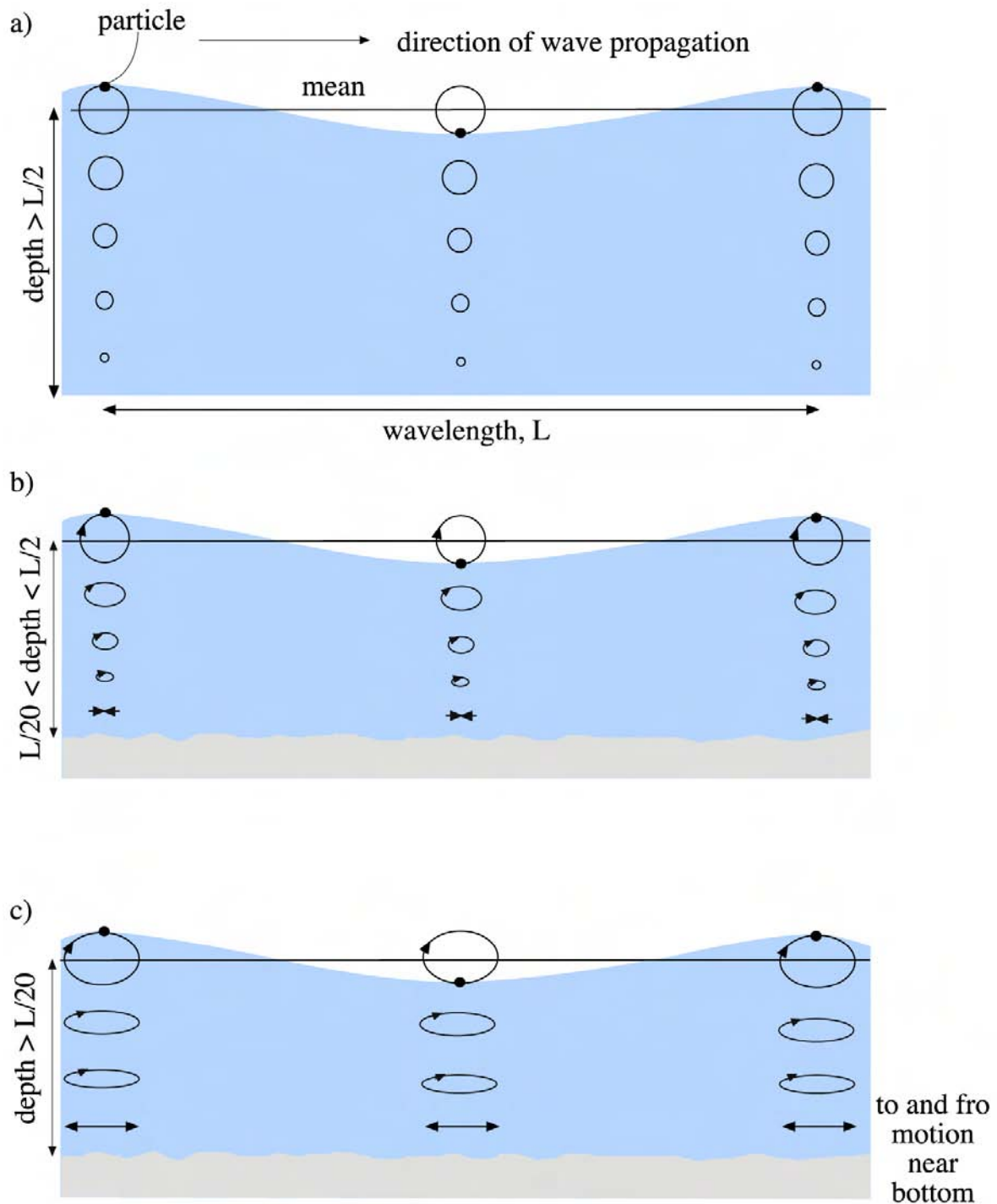


Figure 3.3: (a) Particle motion in deep water, displaying the exponential decrease in the orbital diameters with depth. (b) Particle motion in intermediate deep water. Particle path show both decrease in the horizontal orbital diameter and progressive flattening near the sea-bed. (c) Particle motion in shallow water, showing progressive flattening near the sea-bed, but no decrease in the horizontal orbital diameters (Brown, 1999).

If the water depth is $L/20 < \text{depth} < L/2$, equation 3.1 is required.

As already mentioned, tsunami waves are characterized by a long wavelength (minimum depth = $L/20$); this fact results in the simplification to consider tsunami waves as shallow water waves. Theoretically, only the ratio between water depth and wavelength allows a classification as a certain wave type, meaning that tsunamis can occur in small but shallow bays and lakes and reservoirs. For oceans and greater lakes, the varying water depth defines a tsunami window whose period is 100 – 2000 seconds (Ward, 2000). This feature makes tsunami waves profoundly different from tides and storm waves. So far we have only considered sinusoidal waves. However, observations and numerical investigations revealed that the shape of the tsunami waves varies with respect to the evolution of a tsunami wave itself; but it fits one of the general shapes, shown in Fig. 3.4.

Fig. 3.4 gives idealized sketches of different shapes as cross sections. In

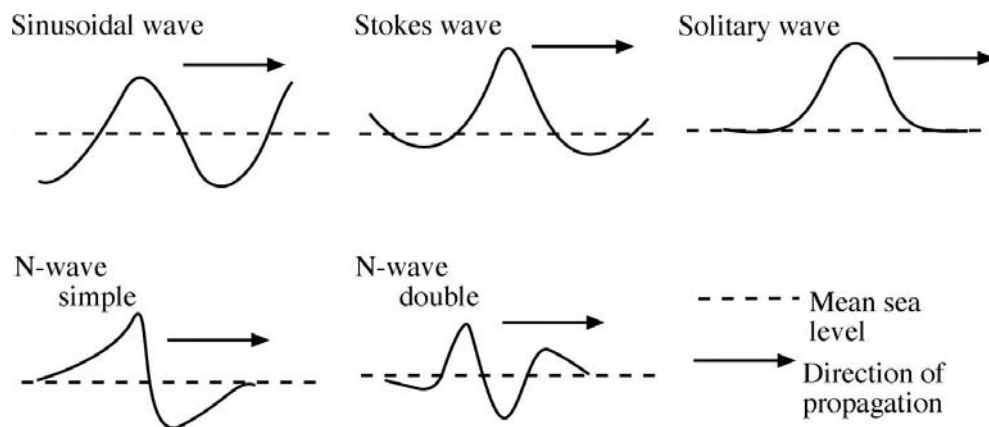


Figure 3.4: Idealized shapes of tsunami waves (Tadepalli and Synolakis, 1994; Geist, 1997). Note that the vertical dimension is greatly exaggerated.

experiments and in theoretical work, often the solitary wave is used because it is the ideal form to prevent energy losses during the propagation. This kind of wave excludes wave components below the sea level. Many observations of real tsunami events revealed that there exists a component below the sea level. This kind of wave is referred to as N-wave (Tadepalli and Synolakis, 1994; Geist, 1997). Independent of the shape of the wave, a fraction of the wave energy is transferred to bottom. Among other parameters the actual amount of energy transferred to the bottom is a function of the water depth. So, it is theoretically possible that a tsunami wave may rework sediment along the entire course of the tsunami wave

train.

Tsunami waves, approaching the shore line, decelerate while the wave height increases as the wavelength decreases. This process is known as amplification. This is due to the long wave length and the fact that different parts of the wave may be located in strongly different water depth. In general, the approach of a tsunami wave towards the shore line can theoretically be considered as the interaction of linear and non-linear elements of the fluid motion (Ward, 2000). The shoaling factor, that is an expression of linear elements, can be determined by the application of a linear wave theory (Ward, 2000; Ward and Asphaug, 2000). It is normally not larger than 6, meaning that the wave height in the coastal area is, at maximum, 6 times of the wave height in the deep water (Ward, 2000; Ward and Asphaug, 2000, 2003). However, the non-linear elements cannot be handled by linear wave theory, neither by simple non-linear approaches. It is only possible to treat them by using highly non-linear approaches like the fully 3D Navier-Stokes equations.

3.2 Sources of Tsunamis

Tsunami waves may have different sources, ranging from tectonic, extra-terrestrial, climate to even human-made sources. Since the characterization of a water wave as a tsunami wave is not only dependent on the source but also on the relationship between water depth and wavelength, explosions in lakes, reservoirs and shallow water, in general, are technically to be seen as tsunami sources. The climatic source is, for example, a calving glacier that loses huge chunks of ice to shallow seas. However, climatic and human-made sources certainly are negligible compared to tectonic and extra-terrestrial sources in terms of range of coverage and potential fatalities.

The tectonic source is the most important one. It is subdivided into different single processes as earthquakes, slides and volcanic hazards. Among them, earthquakes are the most frequent and the most lethal tsunami source. For example in the Pacific ocean, 1171 tsunami events have been counted with 390929 fatalities (Tab. 3.2) With 1171 events, earthquakes are the most prominent cause for death after tsunamis. Japan concentrates the largest death toll with 211300 fatalities. Death were caused by the impact of tsunami waves on the coasts. Surely, the magnitude and position of the source and the local bathymetry affect the depth

Table 3.2: Causes of tsunamis in the Pacific Ocean region over the last 2000 years (according to Bryant, 2001).

Cause	No. of Events	Perc. of Events	No. of Death	Perc. of Death
Earthquakes	1171	82.3	390929	84.5
Landslides	65	4.6	14661	3.2
Volcanic	65	4.6	51643	11.2
Unknown	121	8.5	5364	1.2
Total	1422	100	462597	100

tolls.

From a historical point of view, earthquakes are the most frequent source of tsunami waves. Tab. 3.2 gives other sources that may generate tsunami waves, as well. However there are only three physically different categories of tsunami waves: dislocation, slump and impact source. The dislocation sources are earthquakes and submarine volcanic explosions. Slides in a general manner (also slides by volcanic hazards) count to the slump sources. Meteoritic impacts also generate tsunami waves with varying characteristics. The main characteristics of these sources will be given in this section

Dislocation Source – Earthquakes

The most simple representation of a dislocation source is given in Fig. 3.5. A part of the oceanic crust uplifts. Since, the dislocation is instantaneous and the water is considered as a continuum, a hump is formed at the surface. According to the parameters given by Fig. 3.5, the energy available for the tsunami wave (Okal and Synolakis, 2003) is

$$E_T = 0.5\rho_w g S (\delta h)^2 \quad (3.4)$$

where S is the area of the uplifted section of the ocean floor, δh represents the height of the uplift, g is the gravity and ρ_w is the density of water. Be v the velocity of the dislocation of the ocean floor, for an earthquake is $v \gg c$. c is the travel velocity of the tsunami wave. In this case, the velocity of the upward motion prevents the hydraulic equilibrium during the motion, itself. If $v \ll c$, the hydraulic equilibrium is reached throughout the deformation. The hump of

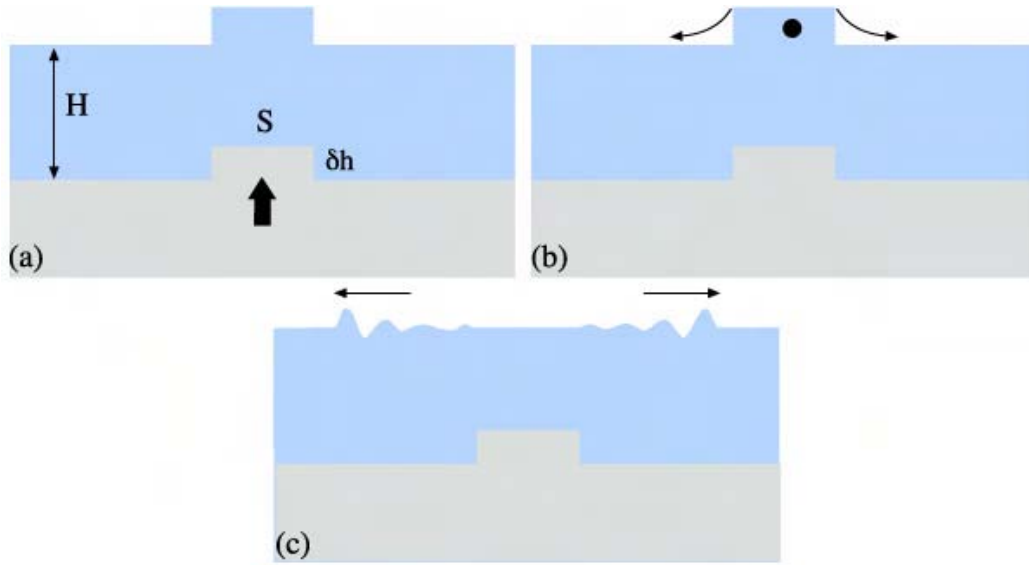


Figure 3.5: (a) a sudden uplift of a fraction of the ocean floor results in an identical hump of ocean surface. (b) the hump is gravitationally collapsed. The center of displaced material (solid dot) falls down by an amount of $\delta h/2$. (c) This change in the potential energy leads to the generation and propagation of tsunami wave (Okal and Synolakis, 2003).

the surface would faster disappear than it is being created by the upward motion.

Eq (3.5) gives the parameters which are important to calculate the energy transformed from dislocation to the tsunami wave. The most appropriate geometry of the earthquake source is the dip-slip source that is very typical for subduction zone earthquakes (Fig...). The vertical displacement u_z of this setting is

$$u_z(x, 0) = \int_a^b U_z(x, s) \delta'_\xi(s) ds \quad (3.5)$$

where a and b are the updip and downdip distances along the ξ -axis, δ' represents any arbitrary distribution of slip along an inclined fault and U_z is a complex-variable representation of stresses (Geist and Dmowsky, 1999). Fig. 3.6c gives the initial tsunami wave form for an earthquake occurring on a inclined plane from 10 km to 38 km depth with a slip component of 1 m. The wave gauges on the left side represent the tsunami wave evolution in the near field, while the right ones represent the tsunami characteristics that propagate towards open ocean.

A more general theory of the generation of tsunami waves is the normal mode theory. This theory explains why a severe earthquake does not deterministically

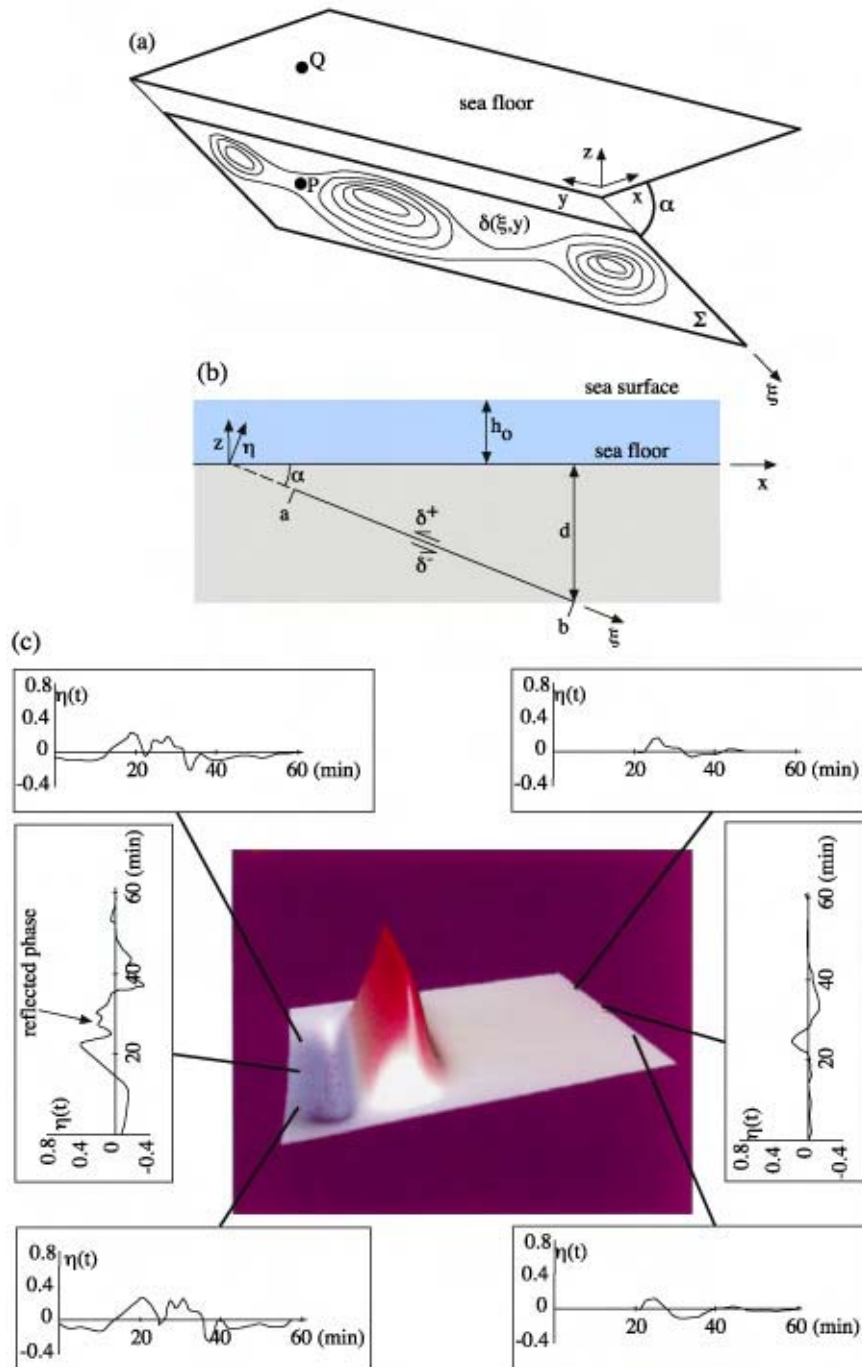


Figure 3.6: (a) 3D view on the fault plane with a slip varying in both dip (ξ) and strike (y) direction. The magnitude of the slip is schematically displayed by the contours (Geist and Dmowsky, 1999). (b) Cross-section of the rupture zone defined by $a \leq \xi \leq b$ where ξ -axis is aligned with the dip direction of the fault plane (Geist and Dmowsky, 1999). (c) Surface plot of the initial tsunami wave form (Geist and Dmowsky, 1999).

result in lethal tsunami waves. It scales characteristics of the source and source mechanisms to the energy supplied to potential tsunami waves.

Slides

The slide source is dipolar as given in Fig. 3.7. The maximum velocity of the moving mass along inclined plane is $v = \sqrt{2gz}$ (Okal and Synolakis, 2003), where z is the vertical extent traveled by the slide. With the help of this equation, the

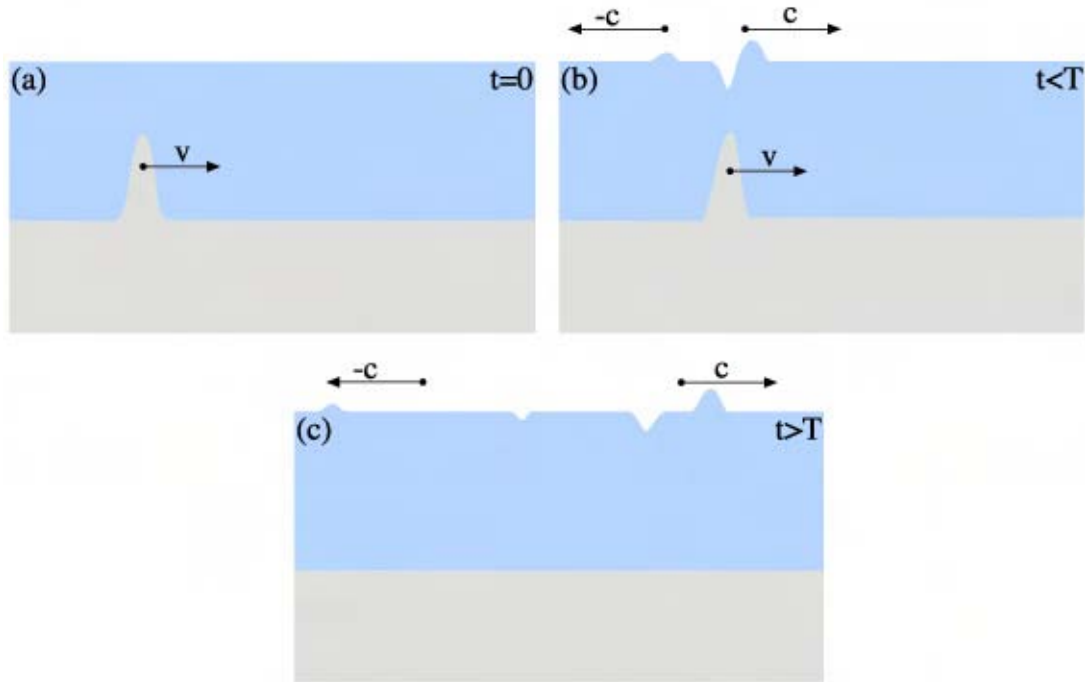


Figure 3.7: A simple slide model with a gaussian curvature of the slide and the propagation of the respective tsunami waves (Okal and Synolakis, 2003).

ratio of the maximum velocity of the slide to the tsunami can be given as:

$$\frac{v}{c} = \sqrt{2\frac{z}{H}} \quad (3.6)$$

Since the water depth H is always larger than z the ratio is $v/c < 1.0$, leading to $v < c$. As already outlined, such a condition characterizes a hydraulic equilibrium which would lead to a vanishing of the hump at the surface. Owing to this fact, it is necessary to quantitatively consider the development of a tsunami wave during

slumping. Okal and Synolakis (2003) assume a gaussian of slumping block, so that the deformation can be given by:

$$\epsilon(x, t) = A + \exp [-k(x - vt)^2] \quad (3.7)$$

Assuming linear waves, the deformation ϵ results in the following wave equation:

$$\frac{\partial^2 \eta}{\partial t^2} - c^2 \frac{\partial^2 \eta}{\partial x^2} = \frac{\partial^2 \epsilon}{\partial t^2} \quad (3.8)$$

Because of the dipolar character of this source, Okal and Synolakis (2003) give two solutions for Eq. 3.7: η_1 for the positive x -direction with

$$\eta_1(x, t) = A H(t) \left[\frac{v^2}{v^2 - c^2} \exp [-k(x - vt)^2] + \frac{v^2}{2c} \left(\frac{\exp [-k(x + ct)^2]}{c + v} + \frac{\exp [-k(x - ct)^2]}{c - v} \right) \right],$$

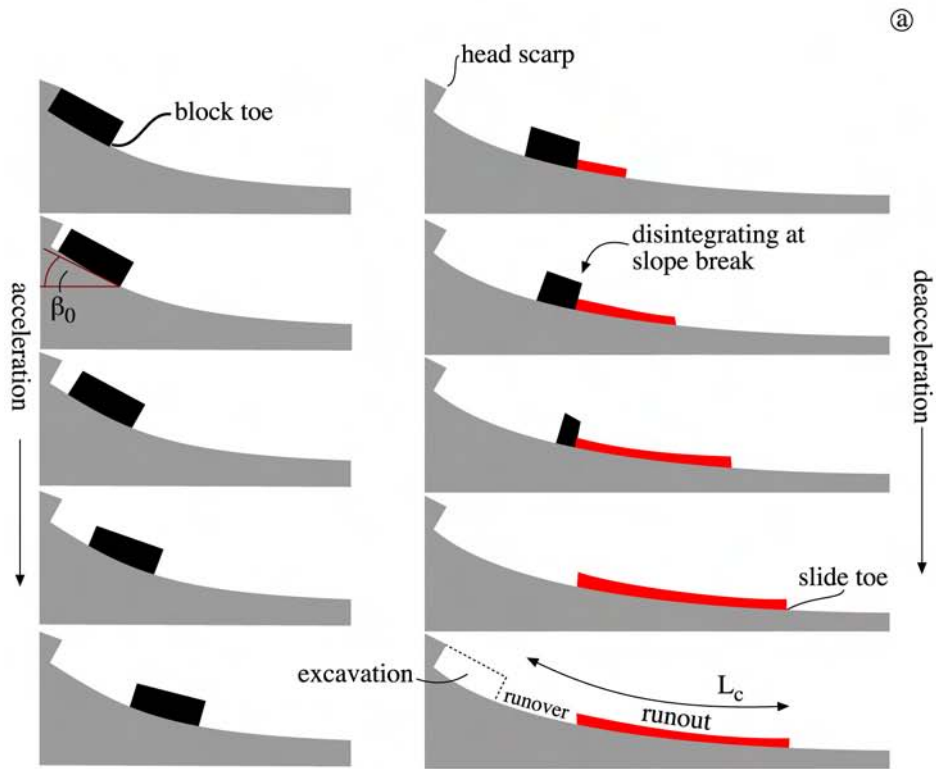
and for the opposite direction ($-x$ -direction):

$$\eta_2(x, t) = -A H(\tau) \left[\frac{v^2}{v^2 - c^2} \exp [-k(\xi - v\tau)^2] + \frac{v^2}{2c} \left(\frac{\exp [-k(\xi + c\tau)^2]}{c + v} + \frac{\exp [-k(\xi - c\tau)^2]}{c - v} \right) \right],$$

In this case, the amplitude of the block is negative. The starting point of the motion for η_2 is $t = T$ and at abscissa $x = L = vT$, where $\xi = x - L$ and $\tau = t - T$. This simple model does not take dispersion of sliding masses into account.



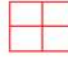
Disintegrating (dispersion) of the slide masses is important because of the asymmetry in size of the erosion and deposition area of the slide. The kinematics of the slide movement is crucial for the understanding of how tsunami waves are generated. Slides have a more complex geometry as given by Fig. 3.7 and Eqs. (3.8). Complex slide geometries can be modeled by the superposition of a discrete number of simple slides (Ward, 2001; Ward and Day, 2002), applying the Green's function approach. Fig. 3.8 compares the simple slide to a typical slide behavior. It is apparent how the slide block is disintegrating; the volume of the initial slide block (black) corresponds to the volume of the runout masses (red).

Fig. 3.8 shows the geometry of a slide and gives the kinematics. The parabolic



Legend for notations:

- $D(t)$ - distance
- $V(t)$ - velocity
- $A(t)$ - acceleration
- β_0 - initial slope angle at block toe
- L_c - slide length

-  excavation
-  runover
-  runout

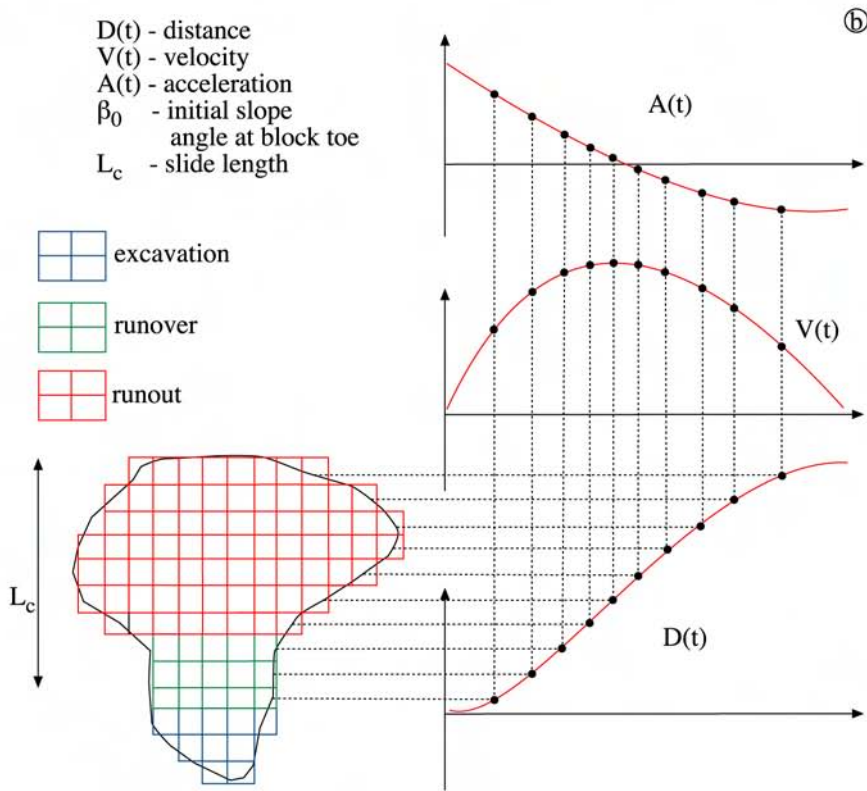


Figure 3.8: Disintegrating of slide masses and slide kinematics (Ward and Day, 2002).

evolution of the slide masses is owing to the gravitationally controlled motion of the slide. It should be mentioned that Ward and Day (2002) uses the Green's function approach to calculate the wave elevation owing to moving slide masses. Okal and Synolakis (2003) use the classical linear wave equations. Both ways are finally based on the linear wave equation with source term as given by Eq. (3.7).

Oceanic Impacts

Physical processes of the dislocation and the slide source differ from each other as demonstrated; nevertheless it is possible to compare both sources by the application of simple models as presented above. The Physics needed for the description of these simplified models is almost the same and strictly based on water as an incompressible continuum. This base assumption can not be made in the case of an oceanic impact.

In the contact and compression stage of an oceanic impact (see sec. 2.2), shock waves are induced. Owing to the characteristics of the shock wave, other physical assumptions as the compressibility of the water ought to be applied. Compressibility of a continuum increases the complexity of the equation system, meaning that it makes no sense to apply very simple assumptions in order to compare oceanic impacts to other tsunami sources.

Before this fact will further be discussed, it should be outlined how tsunami waves are generated by oceanic impacts. A series of snapshots in Fig. 3.9 sketches the wave generation. The second snapshot of this series highlights the generation of two crater rims: one for the "solid" earth and another for the water column. The crater rim of water collapses under gravity. In the course of the collapse, the rim wave is generated (snapshot 3 in Fig. 3.9). During the generation of the rim wave, water begins to resurge into the crater cavity. The resurge results into the generation of a central peak of water (snapshot 4 in Fig. 3.9), which collapses under gravity, likewise. This collapse leads to the generation of the collapse wave (snapshot 5 in Fig. 3.9). In case of the given example, the generation of a huge bore prevents the propagation of the collapse wave. The last snapshot gives the situation after 1700 s. The rim wave has already left the panel. The chunks within the crater cavity are the crater rim that is washed away during the resurge.

The characteristics of the generated waves is determined by the kinetic energy of the impactor and the water depth. To characterize the depth of the water for a constant kinetic energy of impact, the ratio between the impact's diameter d

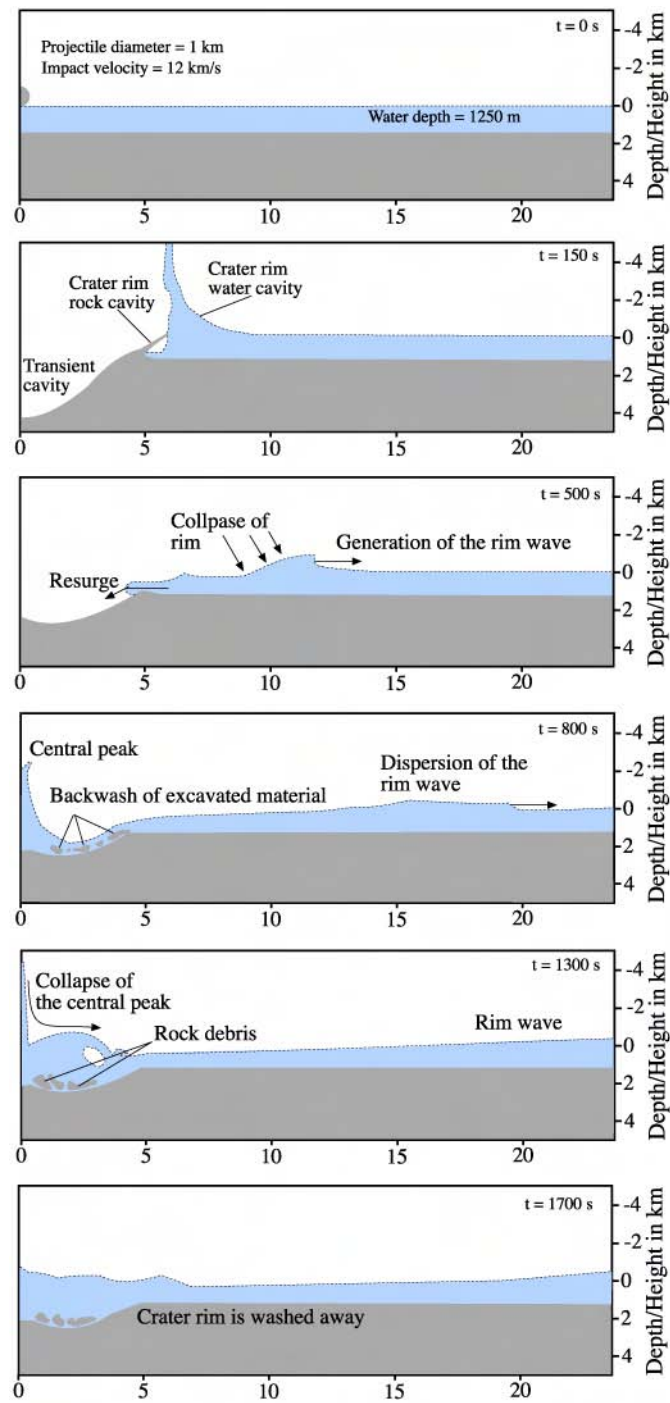


Figure 3.9: Snapshots illustrate the generation of the rim wave and the collapse wave by oceanic impacts.

and the water depth H is used. In this context, shallow water is given by a large d/H -ratio while deep water is characterized by a small d/H -ratio. Based on this definition of the water depth and with the help of numerical experiments, it is possible to subdivide oceanic impacts into three categories: impacts into deep, intermediate and shallow water (Tab. 3.3).

Table 3.3: Characterization of oceanic impacts by the water depth (Weisz et al., 2003).

Water depth	Rim Wave	Collapse Wave
deep	yes (but very small)	yes
intermediate	yes	no (generated; but no propagation)
shallow	yes	no

Impacts into deep water are characterized by a very small rim wave and an enormous collapse wave. If the water depth is very large, resulting in free oscillation of the water column after the collapse of the transient cavity, a huge number of collapse waves is generated (Fig. 3.10.) But also in cases of impacts into deep water, where the water column cannot freely oscillate, the collapse wave is larger than the rim wave. The relevance of the rim wave is increased for impacts into intermediate water. Fig. 3.9 gives an example of such an impact. It is readily recognizable that during the generation of the rim wave, water resurges into the crater cavity. A central peak is also formed but the superposition of the ongoing resurge and the collapse of the central peak finalizes in the generation of a huge bore that prevents the outward propagation of the collapse wave. In case of an impact into shallow water, the rim wave plays the major role because even the generation of the collapse wave is prevented. This is due to the fact that the crater rim is in the same dimension as the water depth; a powerful resurge of water is hindered or even prevented for extremely shallow water.

The wave height as a function of time is measured by gauge points in distances from 8 to 16 km from the impact point (Fig. 3.11). The first peak of each graph represents the crest of the rim wave, the following minimum the trough. Then the crest and trough of the collapse wave follows. Only considering the rim wave, the asymmetry between wave crest and trough is readily recognizable, being due to the superposition of the beginning resurge of water into the crater cavity and the generation of the rim wave, itself. Comparing the graphs for 8 km and 12 km, the wave height is 570 m and 310 m, respectively. This decrease is accompanied with

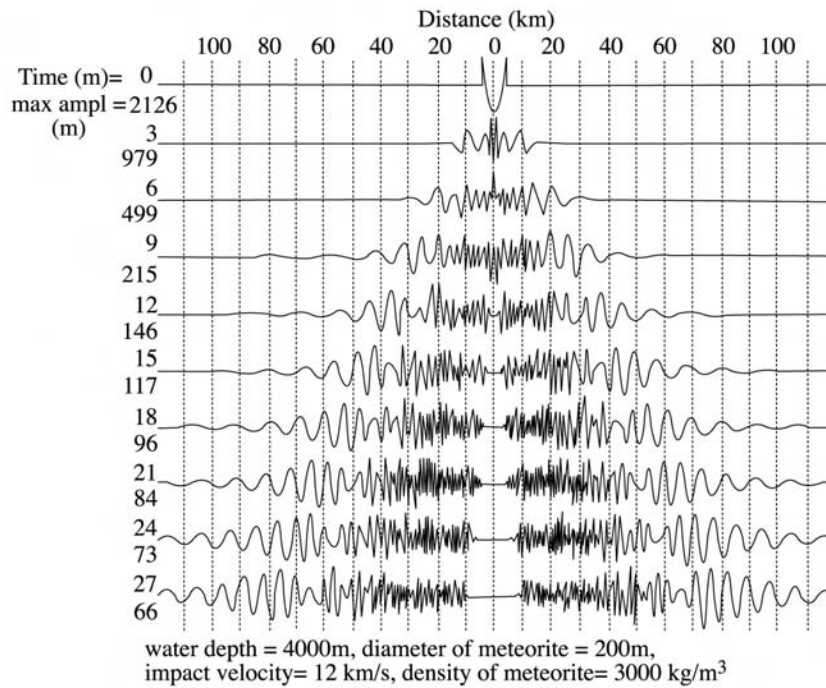


Figure 3.10: Impact of 200 m sized meteorite into 4500 m deep ocean, resulting in free oscillations of the water column (Ward and Asphaug, 2000).

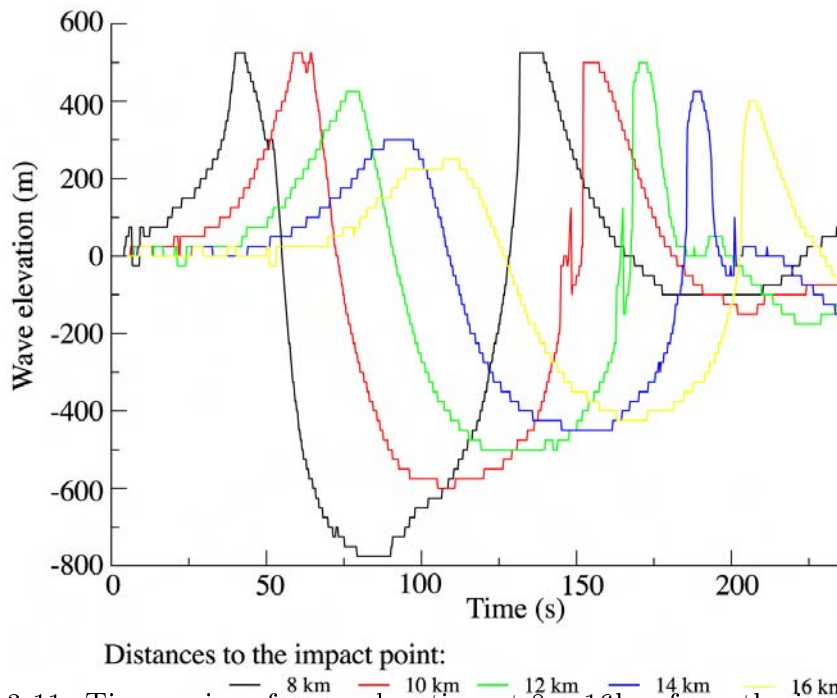


Figure 3.11: Time series of wave elevation at 8 – 16km from the impact point.

an increase in the wavelength owing to dispersion. However, the length of the crest increases faster than the length of the trough. This is due to the asymmetry between wave crest and trough near the generation area of the rim wave.

3.3 On Modeling Tsunami Waves

The modeling of tsunami waves is a crucial task to improve the risk assessment of coastal areas susceptible for tsunami waves. As demonstrated in chapter 1 *Background and Aims* tsunamis may cause severe destruction and have considerable death tolls (Synolakis et al., 2002). The design of the models depend on the source and on the type of tsunami wave. Since earthquakes are the most frequent tsunami sources, the majority of tsunami models is dedicated to tsunami waves generated by earthquakes. However during the last decade, the number of tsunami models using a slide has steadily increased, especially since a slide-generated local tsunami, where the slide is induced by an earthquake, killed 3000 people in Papua New Guinea, 1998 (Synolakis et al., 2002; Fryer et al., 2004). Models, considering oceanic impacts as tsunami source, are very rare. The most accepted one is developed by Steven N. Ward (Ward and Asphaug, 2003; Ward, 2000; Ward and Asphaug, 2000). Advantages and disadvantages of this model will be discussed later in this section.

Classical approaches to simulate tsunami wave propagation are Shallow Water Equations (SWE) in non-linear and linear form, the Korteweg-de-Vries Equations (KdV), and the Boussinesq Equations (BE). The KdV approach is only appropriate for "1+1" problems (one spatial and one temporal dimension) because a fully 2D expansion leads to the Boussinesq equation. The basics of the SWE and the BE are Euler equations that are integrated over depth to achieve a depth-averaged velocity field in the momentum equation. The momentum equation reads (Peregrine, 1967):

$$\nabla_t \bar{w} + \bar{w}(\nabla \cdot \bar{w}) + g\nabla\eta = \frac{h}{2}\nabla \left[\nabla \cdot \left(h \frac{\partial w}{\partial t} \right) \right] - \frac{h^2}{6}\nabla \left(\nabla \cdot \frac{\partial w}{\partial t} \right) \quad (3.9)$$

where \bar{w} represents the depth-integrated velocity field; η is the water surface elevation due to the tsunami wave, g is the gravity and h represents the water depth. Based on this equation, Beji and Nadaoka (1996) expanded the Boussinesq

Equation with special regard to an improvement of the dispersive characteristics:

$$\begin{aligned} \nabla_t \vec{w} + \vec{w}(\nabla_h \cdot \vec{w}) + g\nabla_h \eta &= (1 - \beta) \frac{h}{2} \nabla [\nabla \cdot (h \frac{\partial w}{\partial t})] - \beta \frac{h^2}{6} \nabla (\nabla \cdot \frac{\partial w}{\partial t}) \\ &+ \beta \frac{gh}{2} \nabla [\nabla \cdot (h \nabla \eta)] - \beta \frac{gh^2}{6} \nabla [\nabla^2 \eta] \end{aligned} \quad (3.10)$$

The parameter β controls the dispersive properties of this equation and is normally set to $\beta = 1/5$ (Beji and Nadaoka, 1996). The high order derivatives represent the dispersion which is taken into account. A similar equation was derived by Lynett and Liu (2002). Comparing the equations according to Peregrine (1967), Beji and Nadaoka (1996) and Lynett and Liu (2002), the first two yield reliable result if the depth to wavelength ratio is $d/\lambda < 0.25$, while the equation according to Lynett and Liu (2002) gives reliable results for $d/\lambda < 0.5$.

By the structure of Eqs. (3.9) and (3.10), it is possible to differ non-dispersive elements on the left hand side from dispersive ones on the right hand side of the equations. So in general, they can be rewritten as:

$$\nabla_t \vec{w} + \vec{w}(\nabla \cdot \vec{w}) + g\nabla \eta = \vec{D} \quad (3.11)$$

with \vec{D} denoting the dispersive element. If the dispersive element is equal to the right hand side of equations (3.9) or (3.10) the BE are obtained. However, if the dispersive elements are neglected, leading to $\vec{D} = 0$, the SWE are received. A proper derivation of SWE assumes constant hydrodynamic pressure distribution along the water surface. This assumption results in the elimination of the pressure term of the Euler equation and the establishment of the term $g\nabla \eta$. The momentum equation of SWE is:

$$\nabla_t \vec{w} + \vec{w}(\nabla \cdot \vec{w}) + g\nabla \eta = 0 \quad (3.12)$$

In order to make Boussinesq and the SWE to complete approaches, a continuity equation needs to be introduced. Such an equations is:

$$\frac{\partial \eta}{\partial t} + [h + \eta] (\nabla_h \cdot \vec{w}) + \vec{w} \nabla_h [h + \eta] = 0 \quad (3.13)$$

A numerical model successfully computes tsunami wave propagation on a plane if a momentum equation (eqs 3.9, 3.10 or 3.12) is combined with the continuity equation (eq. 3.13) and initial or boundary conditions, especially source terms.

The SWE (equations 3.12 & 3.13) can only be numerically solved for real-

istically varying water depth. Nonetheless, there exists an analytical solution achieved by Synolakis (1986, 1987). This solution includes the run-up of waves. However, Synolakis assumes a uniform water depth up to the beach break and a linear beach. A soliton was used as the boundary condition, which is the simplest shape of a wave to prevent dispersion.

Another interesting analytical approach to tsunami propagation problem has been developed by Steven N. Ward (Ward, 2000; Ward and Asphaug, 2000, 2003)). He uses the Green's function approach to solve the Euler equations. It should be mentioned that this approach provides very reliable results for linear environments, meaning the water depth is large and the amplitude of the wave is small. In case of oceanic impacts, those conditions are given by a deep water and small bolide (impacts into deep water). Unfortunately, the evolution of considered waves, including the runup is not solved as closed mathematical problem as the shore line is represented by an asymptote towards infinity. The asymptotic behavior has to be buffered by mathematical constructs. Furthermore, from a mathematical point of view, this approach should not give reliable results for impacts into shallow and intermediate water.

Equations 3.9 to 3.11 are used to develop a 2D wave propagation model based on dispersive and non-dispersive equations. This model is the major achievement of this thesis. Its technical details are described in the next chapter.

Chapter 4

Numerical and Computational Methods

Equations used in this thesis to compute the wave propagation are numerically solved. Finite Element Method (FEM), the Boundary Element Method (BEM) and the Finite Difference Method (FDM) are the most common numerical approaches. Among them, FDM is the oldest and probably most frequently used method to solve complex equations. This chapter introduces FDM and also gives insights into the global strategy of modeling oceanic impacts and tsunami wave propagation, discretizations and boundary conditions. Additionally, basics of the MOST (Method Of Splitting Tsunami) is described with which the runup and inundation of the land is simulated.

4.1 Finite Difference Method

The idea behind the FDM is directly linked to the definition of a derivative of a function ϕ :

$$\left(\frac{\partial\phi}{\partial x}\right)_{x_i} = \lim_{\Delta x \rightarrow 0} \frac{\phi(x_i + \Delta x) - \phi(x_i)}{\Delta x} \quad (4.1)$$

The geometrical interpretation of this consideration is shown in Fig. 4.1. In this figure the solid line represents the function ϕ . At point x_i the first derivative has to be calculated. The solid straight line is the tangent. The slope of this tangent represents the exact solution for the first derivative of the function ϕ . The dotted, dashed and dot-dashed straight lines are other differential approximations. The *forward difference* (dotted line) is the derivative at point x_i which is approximated

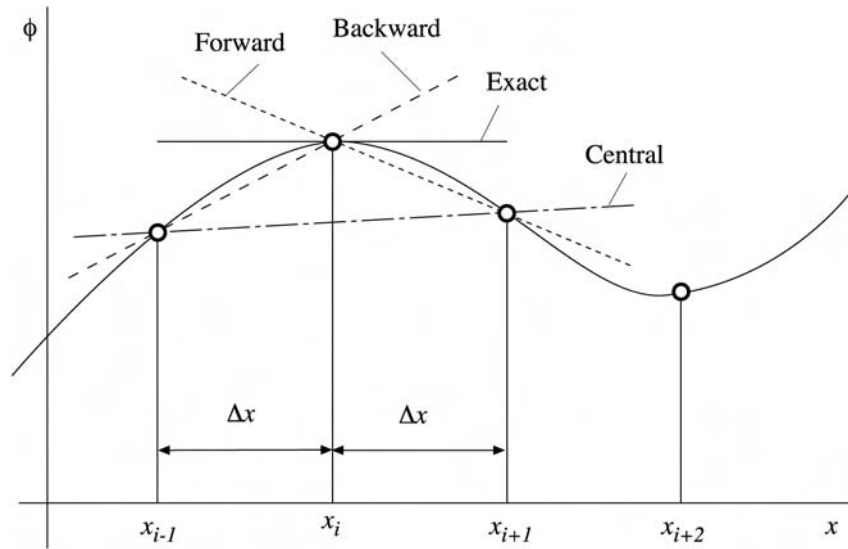


Figure 4.1: On the definition of a derivative and its approximations (Ferziger and Peric, 2002).

by the slope of a line passing through the point x_i and x_{i+1} . The dashed line displays the *backward difference* which approximates the first derivative in point x_i with the help of point x_{i-1} . The dot-dashed line is the *central difference* which uses the slope of a line passing through the point x_{i-1} and x_{i+1} . The graphically given approximations to the first derivative of a function ϕ at a point x_i can also be mathematically derived. Any continuous differentiable function ϕ at point x_i can be expressed by a Taylor series:

$$\begin{aligned} \phi(x) = & \phi(x_i) + (x - x_i) \left(\frac{\partial \phi}{\partial x} \right)_i + \frac{(x - x_i)^2}{2!} \left(\frac{\partial^2 \phi}{\partial x^2} \right)_i + \\ & \frac{(x - x_i)^3}{3!} \left(\frac{\partial^3 \phi}{\partial x^3} \right)_i + \dots + \frac{(x - x_i)^n}{n!} \left(\frac{\partial^n \phi}{\partial x^n} \right)_i + H, \end{aligned} \quad (4.2)$$

where H represents *higher order terms* which can be neglected. Applying the Taylor series expansion to the first derivation of function ϕ at point x_{i+1} gives:

$$\left(\frac{\partial \phi}{\partial x} \right)_i = \frac{\phi_{i+1} - \phi_i}{x_{i+1} - x_i} - \frac{x_{i+1} - x_i}{2} \left(\frac{\partial^2 \phi}{\partial x^2} \right)_i - \frac{(x_{i+1} - x_i)^2}{6} \left(\frac{\partial^3 \phi}{\partial x^3} \right)_i + H \quad (4.3)$$

Equation (4.2) can also be applied to the derivation at point x_{i-1} :

$$\left(\frac{\partial\phi}{\partial x}\right)_i = \frac{\phi_i - \phi_{i-1}}{x_i - x_{i-1}} - \frac{x_i - x_{i-1}}{2} \left(\frac{\partial^2\phi}{\partial x^2}\right) - \frac{(x_i - x_{i-1})^2}{6} \left(\frac{\partial^3\phi}{\partial x^3}\right) + H \quad (4.4)$$

It is also possible to apply equation (4.2) to both x_{i+1} and x_{i-1} :

$$\begin{aligned} \left(\frac{\partial\phi}{\partial x}\right)_i = & \frac{\phi_{i+1} - \phi_{i-1}}{x_{i+1} - x_{i-1}} - \frac{(x_{i+1} - x_i)^2 - (x_i - x_{i-1})^2}{2(x_{i+1} - x_{i-1})} \left(\frac{\partial^2\phi}{\partial x^2}\right) - \\ & \frac{(x_{i+1} - x_i)^3 + (x_i - x_{i-1})^3}{6(x_{i+1} - x_{i-1})} \left(\frac{\partial^3\phi}{\partial x^3}\right) + H \end{aligned} \quad (4.5)$$

Depending on the number of higher order terms, equations (4.3), (4.4) and (4.5) are very close approximations of the first derivative of function ϕ . However, these equations do not simplify the problem of calculating the first derivative. Numerically useful approximations to the first derivative can be obtained by ignoring the higher order terms and the term with higher derivatives, as well. The ignored terms can be understood as a truncation error which mainly depends on the resolution Δx (see Fig. 4.1). The truncation of respective terms in Eqs (4.3), (4.4) and (4.5) yields:

$$\text{forward differences: } \left(\frac{\partial\phi}{\partial x}\right)_i \approx \frac{\phi_{i+1} - \phi_i}{x_{i+1} - x_i} \quad (4.6)$$

$$\text{backward differences: } \left(\frac{\partial\phi}{\partial x}\right)_i \approx \frac{\phi_i - \phi_{i-1}}{x_i - x_{i-1}} \quad (4.7)$$

$$\text{central differences: } \left(\frac{\partial\phi}{\partial x}\right)_i \approx \frac{\phi_{i+1} - \phi_{i-1}}{x_{i+1} - x_{i-1}} \quad (4.8)$$

Regarding to the truncation error, the first deleted term has the largest influence on the grade of accuracy. In other words, this first term is the principal source of errors in the numerical calculation by using one of the differences above. The truncation error is the sum of product of a power of the spacing between points and a high order derivative at point $x = x_i$ (Ferziger and Peric, 2002):

$$\epsilon_\tau = (\Delta x)^m \alpha_{m+1} + (\Delta x)^{m+1} \alpha_{m+2} + \dots + (\Delta x)^n \alpha_{n+1}, \quad (4.9)$$

α 's are the high order derivatives multiplied by constant factors. One can easily recognise, that the first term in Eq. (4.9) dominates the error. As already outlined, increasing the spatial resolution Δx , the distance between the exact

solution and the numerical solution becomes smaller. The error is proportional to $(\Delta x)^m$, where m is the dominate term of the truncated terms. That also means the error is reduced by a factor of 2^m .

The schemes of Eqs. (4.6) – (4.8) can be applied to adjacent points in same time level or in the previous time level. Fig. 4.2 illustrates these possibilities. The implicit scheme requires, in the simplest case, iterations to get the solution

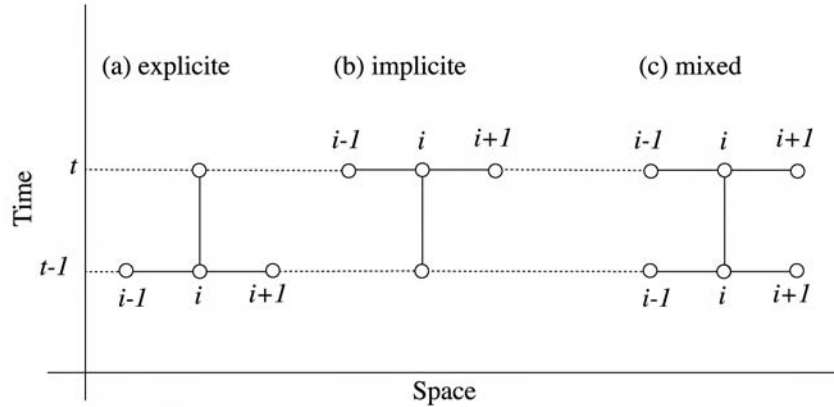


Figure 4.2: Illustration of different numerical approximations (Press et al., 1992).

of one time step because the parameters at the adjacent point are unknown as well. If it is necessary to apply such an implicit scheme, it is better to transform the system of equations into a matrix form. In this form it is possible to apply a clever solver for the system of equations. Also mixed schemes are possible like the Ruge–Kotta scheme (Press et al., 1992). They are of importance to terms with mixed spatial and temporal derivatives, as in the Boussinesq approach.

4.2 Time and Space Discretization for the Wave Propagation Problem

For an orthogonal velocity field \vec{w} with the components $\vec{w} = \vec{u} + \vec{v}$, Eq. (3.11) becomes:

$$\frac{\partial \vec{u}}{\partial t} + \vec{u} \frac{\partial \vec{u}}{\partial x} + \vec{v} \frac{\partial \vec{u}}{\partial y} + g \frac{\partial \eta}{\partial x} = \vec{D}_u \tag{4.10}$$

$$\frac{\partial \vec{v}}{\partial t} + \vec{u} \frac{\partial \vec{v}}{\partial x} + \vec{v} \frac{\partial \vec{v}}{\partial y} + g \frac{\partial \eta}{\partial y} = \vec{D}_v \tag{4.11}$$

As known from section 3.3 *On Modeling Tsunami Waves*, the left hand side comprises non-dispersive elements, while $D_{u,v}^{\vec{}}$ denotes dispersive ones. If $D_{u,v}^{\vec{}} = 0$ (SWE) the numerical scheme is purely explicit (Fig. 4.2); however if $D_{u,v}^{\vec{}} \neq 0$, then a mixed scheme is required as described below. No matter the value of $D_{u,v}^{\vec{}}$, Eq. (3.13) needs to be added as the equation of continuity. Only considering SWE, an explicit centered finite difference scheme is used. The parameter $\psi = \psi(x, y, t)$ depends on both spatial directions and time. The following numerical operators are defined for the first derivate in time and space of ψ :

$$\delta^{(t)}\psi = \frac{\psi(x, y, t) - \psi(x, y, t - \Delta t)}{\Delta t} \quad (4.12)$$

$$\delta^{(x,t-1)}\psi = \frac{\psi(x + \Delta x, y, t - \Delta t) - \psi(x - \Delta x, y, t - \Delta t)}{2\Delta x} \quad (4.13)$$

$$\delta^{(y,t-1)}\psi = \frac{\psi(x, y + \Delta y, t - \Delta t) - \psi(x, y - \Delta y, t - \Delta t)}{2\Delta y} \quad (4.14)$$

$$\delta_{Lax}\psi = 0.25 * (\psi(x + \Delta x, y, t - \Delta t) + \psi(x - \Delta x, y, t - \Delta t) + \psi(x, y + \Delta y, t - \Delta t) + \psi(x, y - \Delta y, t - \Delta t)) \quad (4.15)$$

With the help of these numerical operators, SWE can be written as:

$$\delta_{Lax}^{(t)}\vec{u} = -\vec{u}\delta^{(x,t-1)}\vec{u} - \vec{v}\delta^{(y,t-1)}\vec{u} - g\delta^{(x,t-1)}\eta \quad (4.16)$$

$$\delta_{Lax}^{(t)}\vec{v} = -\vec{u}\delta^{(x,t-1)}\vec{v} - \vec{v}\delta^{(y,t-1)}\vec{v} - g\delta^{(y,t-1)}\eta \quad (4.17)$$

$$\delta_{Lax}^{(t)}\eta = -[h + \eta] (\delta^{(x,t-1)}\vec{u} + \delta^{(y,t-1)}\vec{v}) - \vec{u}\delta^{(x,t-1)}[h + \eta] - \vec{v}\delta^{(y,t-1)}[h + \eta] \quad (4.18)$$

These equations are used to consider SWE. But if $D_{u,v}^{\vec{}} \neq 0$, a mixed scheme is used (Fig. 4.2). From Eq. (3.11) follows that

$$\begin{aligned} D_{u,v}^{\vec{}} = & (1 - \beta) \frac{h}{2} \nabla \left[\nabla \cdot \left(h \frac{\partial w}{\partial t} \right) \right] - \beta \frac{h^2}{6} \nabla \left(\nabla \cdot \frac{\partial w}{\partial t} \right) \\ & + \beta \frac{gh}{2} \nabla [\nabla \cdot (h \nabla \eta)] - \beta \frac{gh^2}{6} \nabla [\nabla^2 \eta] \end{aligned} \quad (4.19)$$

In evaluating this expression (Eq. 4.19), a coordinate splitting is assumed in which spatially mixed and orthogonal derivatives are neglected:

$$\begin{aligned}\vec{D}_u = & (1 - \beta)h \left[\frac{h}{2} \frac{\partial^3 \vec{u}}{\partial x^2 \partial t} + \frac{\partial h}{\partial x} \frac{\partial^2 \vec{u}}{\partial x \partial t} + \frac{1}{2} \frac{\partial \vec{u}}{\partial t} \frac{\partial^2 h}{\partial x^2} \right] \\ & - \beta \frac{h^2}{3} \left[\frac{\partial^3 \vec{u}}{\partial x^2 \partial t} + g \frac{\partial^3 \eta}{\partial x^3} \right] \\ & + \beta \frac{gh}{2} \left[h \frac{\partial^3 \eta}{\partial x^3} + 2 \frac{\partial h}{\partial x} \frac{\partial^2 \eta}{\partial x^2} + \frac{\partial \eta}{\partial x} \frac{\partial^2 h}{\partial x^2} \right]\end{aligned}\quad (4.20)$$

$$\begin{aligned}\vec{D}_v = & (1 - \beta)h \left[\frac{h}{2} \frac{\partial^3 \vec{v}}{\partial y^2 \partial t} + \frac{\partial h}{\partial y} \frac{\partial^2 \vec{v}}{\partial y \partial t} + \frac{1}{2} \frac{\partial \vec{v}}{\partial t} \frac{\partial^2 h}{\partial y^2} \right] \\ & - \beta \frac{h^2}{3} \left[\frac{\partial^3 \vec{v}}{\partial y^2 \partial t} + g \frac{\partial^3 \eta}{\partial y^3} \right] \\ & + \beta \frac{gh}{2} \left[h \frac{\partial^3 \eta}{\partial y^3} + 2 \frac{\partial h}{\partial y} \frac{\partial^2 \eta}{\partial y^2} + \frac{\partial \eta}{\partial y} \frac{\partial^2 h}{\partial y^2} \right]\end{aligned}\quad (4.21)$$

In terms of the operators given by Eqs. (4.12) – (4.15), spatial derivations are now applied in the current time step and not in the previous one:

$$\begin{aligned}\vec{D}_u = & 0.5(1 - \beta)h^2(\delta^{(x,t)}(\delta^{(x,t)}(\delta^{(t)}\vec{u}))) + (1 - \beta)h(\delta^{(x,t-1)}h)(\delta^{(x,t)}(\delta^{(x,t)}(\delta^{(t)}\vec{u}))) \\ & + 0.5(1 - \beta)h(\delta^{(t)}\vec{u})(\delta^{(x,t-1)}(\delta^{(x,t-1)}h)) - 0.3\beta h^2(\delta^{(x,t)}(\delta^{(x,t)}(\delta^{(t)}\vec{u}))) \\ & - 0.3\beta gh^2(\delta^{(x,t)}(\delta^{(x,t)}(\delta^{(x,t)}\eta))) + 0.5\beta gh^2(\delta^{(x,t)}(\delta^{(x,t)}(\delta^{(x,t)}\eta))) \\ & + \beta gh(\delta^{(x,t-1)}h)(\delta^{(x,t)}(\delta^{(x,t)}\eta)) + 0.5\beta gh(\delta^{(x,t)}(\delta^{(x,t-1)}(\delta^{(x,t-1)}h)))\end{aligned}\quad (4.22)$$

$$\begin{aligned}\vec{D}_v = & 0.5(1 - \beta)h^2(\delta^{(y,t)}(\delta^{(y,t)}(\delta^{(t)}\vec{v}))) + (1 - \beta)h(\delta^{(y,t-1)}h)(\delta^{(y,t)}(\delta^{(y,t)}(\delta^{(t)}\vec{v}))) \\ & + 0.5(1 - \beta)h(\delta^{(t)}\vec{v})(\delta^{(y,t-1)}(\delta^{(y,t-1)}h)) - 0.3\beta h^2(\delta^{(y,t)}(\delta^{(y,t)}(\delta^{(t)}\vec{v}))) \\ & - 0.3\beta gh^2(\delta^{(y,t)}(\delta^{(y,t)}(\delta^{(y,t)}\eta))) + 0.5\beta gh^2(\delta^{(y,t)}(\delta^{(y,t)}(\delta^{(y,t)}\eta))) \\ & + \beta gh(\delta^{(y,t-1)}h)(\delta^{(y,t)}(\delta^{(y,t)}\eta)) + 0.5\beta gh(\delta^{(y,t)}(\delta^{(y,t-1)}(\delta^{(y,t-1)}h)))\end{aligned}\quad (4.23)$$

As already mentioned, β controls dispersive properties. If $\vec{D}_{u,c} \neq 0.0$, Eqs. (4.16) – (4.18) and (4.22)–(4.23) are embedded into an iterative loop to constrain to values for parameters in the same time level. The number of dispersive terms shows the strongly increased computational efforts in order to take dispersion into account. They are only used if the water depth to wavelength ratio is less than 0.05.

4.3 Boundary Conditions and the Computational Domain

The impact simulation serves for defining the initial conditions required in the wave propagation model, as well as the wave propagation model for the MOST code. However due to the complete different structure of the utilized codes, it is of no advantage to connect them directly. In order to compute the evolution of impact-related tsunamis, the impact model runs, then the propagation model and then MOST.

If the amplitude of the shock wave is large, then compressible calculations are needed. However, the shock wave is rapidly weakened and soon compressibility can be neglected. The transition between the impact and the wave propagation model can only be done at this distance where compressibility can be neglected. Fig. 4.3a shows a snapshot 150 sec after the impact started. The light gray area represents the interval where position of the surface and the depth-averaged horizontal velocity are recorded. Fig. 4.3b depicts the wave elevation in the resolution of the wave propagation model. The dots represent original data, while the line displays smooth data which are used in the wave propagation model. From the center of the impact area to the left boundary of the transition interval, wave elevation and velocity are kept at zero; for the distance larger than the right boundary, the wave elevation and velocity is calculated by Eqs. (4.10) and (4.11). Vertical impacts produce a circular wave pattern. Hence, the impact area is embedded in the computational domain as a circle. Fig. 4.3c gives a close-up of the impact area. The blue area represents the impact area and blueish one is the wave propagation zone. The light blue band in Fig. 4.3c highlights the transition zone between the impact and the wave propagation area.

The transition between the wave propagation code and MOST is simply done by the input of information on wave elevation and the horizontal velocities at a certain time into MOST (for a graphical representation of the transition see Fig. 6). The computational domain of the model presented is made up of the generation and the propagation zone. The propagation zone contains the areas where the runup is calculated in coastal areas. To simulate the propagation and runup in the coastal zone, the MOST code is used, described in the next section. Islands, which can also be situated within this zone, have only reflective boundaries. The shape of islands must, at least, consist of two cells. Islands that

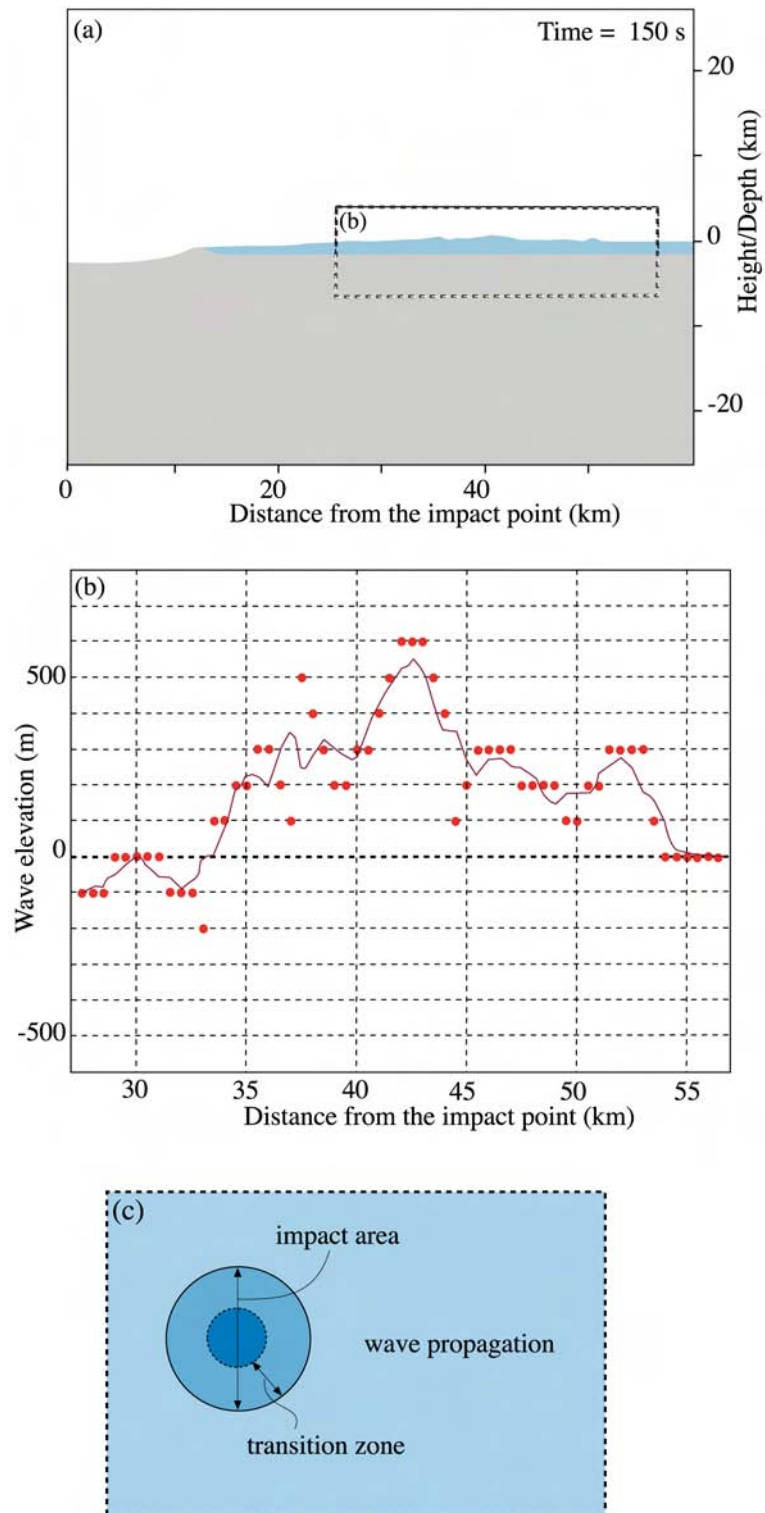


Figure 4.3: Transition between the SALE hydrocode and the wave propagation.

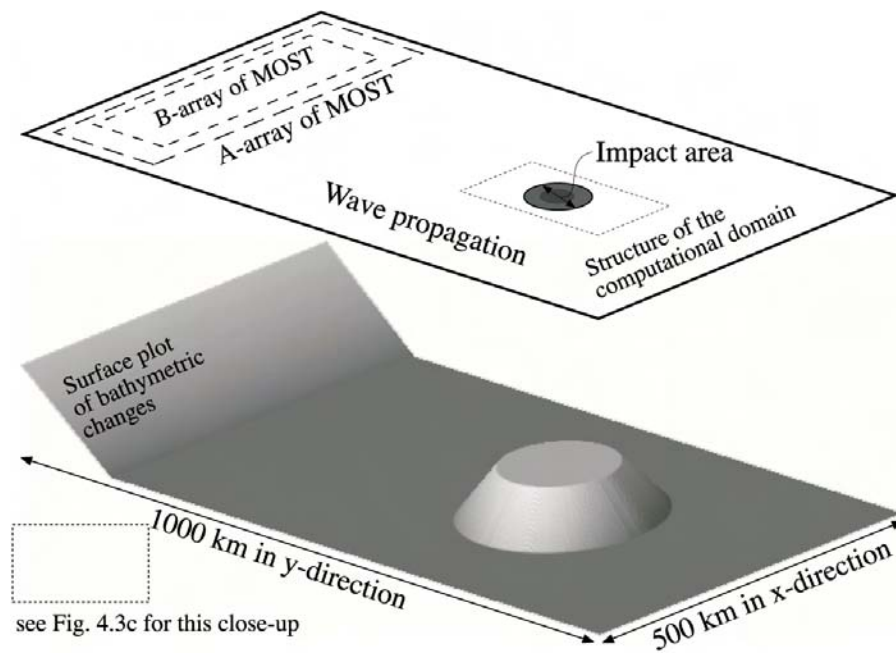


Figure 4.4: Structure of the computational domain.

are only made up of one cell will be erased from the propagation domain. To include open boundaries, a layer of 200 extended cells is added to each side of the wave propagation domain. The open ocean boundary is implemented by a layer of extending cells, calculated by $dx_{i+1} = dx_i \cdot \xi$ whereas ξ is between 1.01 and 1.03. If ξ is larger 1.03 reflection occurs at cell boundaries. The same method is utilized in the SALE code to prevent reflection of the shockwave at the grid boundary (see section 2.3). The tsunami waves propagate through this boundary without any reflections.

4.4 Runup

The calculation of the tsunami wave runup is a complex problem; a variety of methods have been proposed (Synolakis, 1987; Harbitz and Pedersen, 1992; Marchuk and Anisimov, 2001; Titov and Synolakis, 1995, 1998). Among them, different assumptions for the solution of this problem can be distinguished. Analytical approaches often emanate from linear or, at least, piecewise linear geometries in coastal areas. The accuracy of numerical or semi-numerical (Harbitz and Pedersen, 1992) methods is strongly affected by the spatial resolution.

To compute the runup, the MOST (Method Of Splitting Tsunamis) code

is used, developed by Titov and Synolakis (1995, 1998). MOST uses SWE to consider the propagation. A moving boundary is implemented to consider the runup. Fig. 4.5 gives a definition sketch for the shoreline computation. The basic

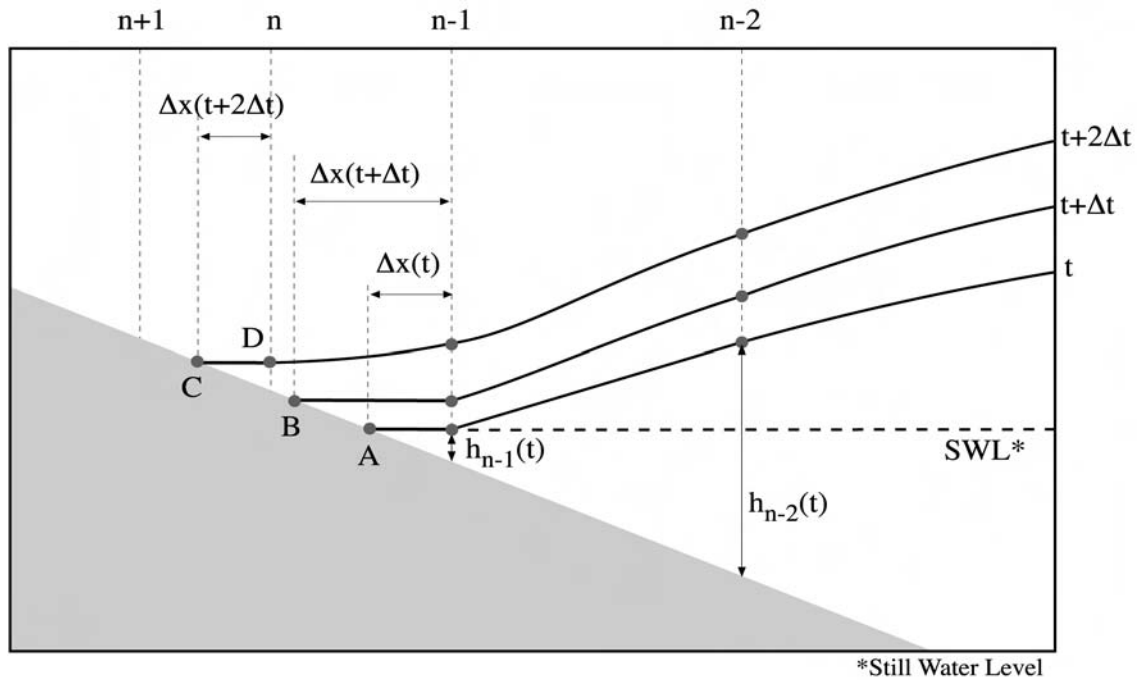


Figure 4.5: Shoreside computations in MOST (according to Titov and Synolakis, 1995)

assumption is a straight line between the last wet point and the position of the shoreline. New computational points are added according to the flow velocity over land. Within MOST, the characteristics of a tsunami wave is always discretized by a constant number of grid points. During shoaling and runup, the wavelength decreases as MOST reduces the spatial step size to keep a constant number of grid points along the wave characteristics. A more comprehensive description about the runup algorithm may be drawn from Titov and Synolakis (1995).

The algorithm to compute the runup used in MOST is very similar to a method proposed by Marchuk and Anisimov (2001). This method considers a "1+1" propagation and runup problem (Marchuk and Anisimov, 2001). I am working on the extension of Marchuk and Anisimov's method to a "2+1" problem in order to compute the propagation and runup with only one model. However, the MOST is much further in progress. It is tested against laboratory experiments

and analytically solvable problems (Titov and Synolakis, 1998, 1995). Additionally, it has been shown that MOST is very appropriate to simulate tsunami waves, for example the 1994 Kurils Islands Tsunami (Titov and Synolakis, 1998), 1996 Peru Tsunami (Titov and Synolakis, 1998), 1993 Okushiri Tsunami (Titov and Synolakis, 1998), 1998 Papua New Guinea Tsunami (Synolakis et al., 2002; Okal et al., 2003).

4.5 Validation of the Wave Propagation Model

The validation of the wave propagation model is split into two parts. The first part only considers non-dispersive wave propagation ($\vec{D} = 0$) and the second one includes dispersion introduced by Eqs. (4.20) and (4.21). The validation of the non-dispersive wave propagation is done with the help of the VTCS-2/MOST code. This code is comprehensively tested against the analytical solution of SWE and laboratory experiments (Titov and Synolakis, 1998, 1995). Fig. 4.6 gives the propagation of a 0.005 elliptic wave over constant depth. The elevation and the time are given in normalized coordinates. The number of points to describe the initial condition is 50. The red line represents the VTCS-2 run (Titov and Synolakis, 1995), while the black one corresponds the non-dispersive wave propagation. The agreement is rather good.

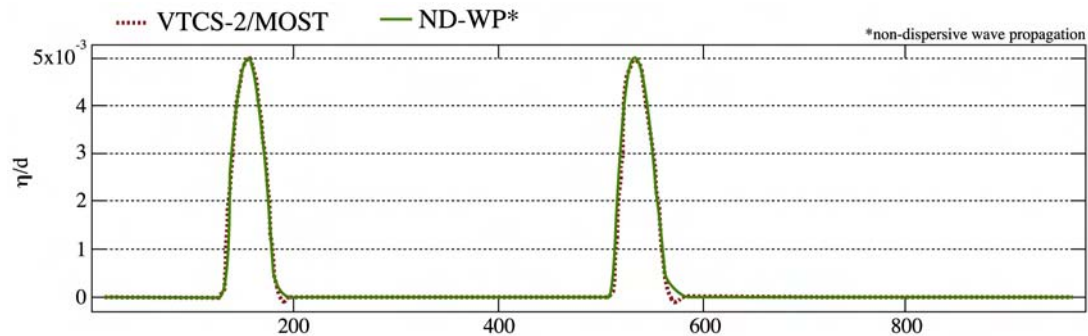


Figure 4.6: Comparison of non-dispersive wave propagation ND-WP with MOST. The red line is according to Titov and Synolakis (1995). Further information, see text.

To validate dispersive computations, the wave elevation as a function of the distance ought to be proportional to $1/r$. Ward and Asphaug (2000, 2002), who

use a dispersive linear theory, achieve the same $1/r$ relationship as it is supposed to come from a linear theory.

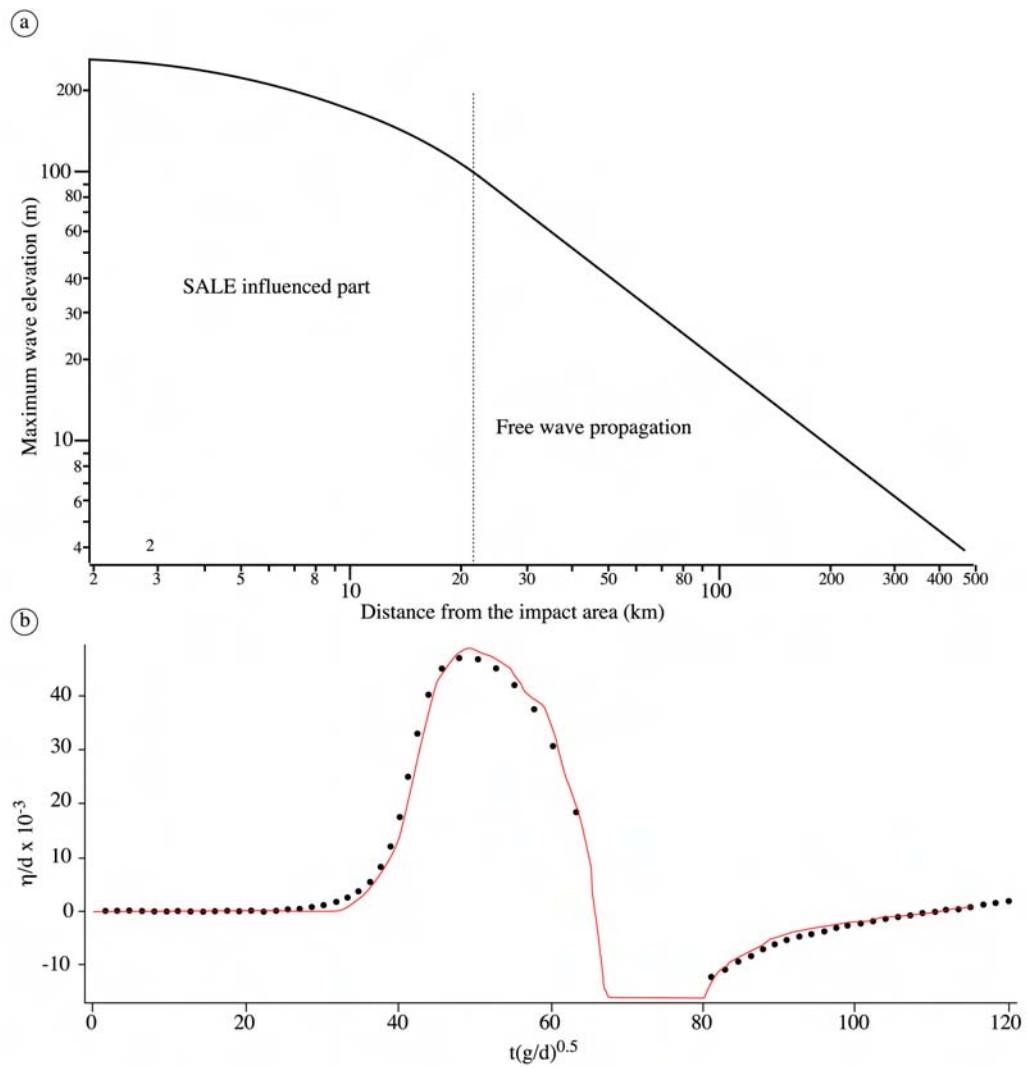


Figure 4.7: Upper panel: The maximum wave elevation as a function of the distance. The free wave propagation is proportional to $1/r$. Lower panel: Comparison of runup data between experiments (solid dots) and MOST (red line). Redrawn according to Titov and Synolakis (1995).

The stability criterion is the *Courant number*, which is

$$c = \frac{\Delta x}{\Delta t} \quad (4.24)$$

$$c \frac{\Delta t}{\Delta x} \begin{cases} > 1 & \text{technically not stable} \\ < 1 & \text{technically stable} \end{cases} \quad (4.25)$$

In this equation, c is the phase velocity, Δt represents the time step and Δx the spatial resolution, respectively. If the *Courant number* is larger than one, the calculations are not stable. However if the *Courant number* is less than one they technically remain stable.

The MOST code is validated and verified by Titov and Synolakis (1995, 1998). To verify this model, experiments, carried out by Synolakis (1986, 1987), were used. The upper panel of Fig. 5.12 illustrates the agreement of MOST with runup experiments of a non-breaking wave; the lower one gives the agreement to breaking wave. Owing to the good agreement between MOST and ND-WP, it can be expected that ND-WP would also be in good agreement with the non-breaking wave experiments.

Chapter 5

Experiments in Modeling Impacts and Wave Propagation

Three different experiments were constructed to investigate the generation mechanisms of tsunami waves caused by oceanic impacts, the influence of bathymetric variations on the wave evolution and the difference in the wave evolution based on a linear and real bathymetry. The investigation of the generation mechanisms of tsunami waves caused by oceanic impacts covers the analysis of characteristics of the rim wave. In the course of this analysis several problems arose. The most critical point here, is the fact that only four impact with varying parameters are available. The other problems in this experiment occurred, likewise, due to computational limitations of the SALE hydrocode. Those limitations are explained in a separate section. Hence, the presented analysis gives only a rough insight into characteristics of the rim wave. When more computational power will be available, especially the amplitude of the rim wave can be quantitatively related to the wave evolution and the runup.

The experiment concerning the investigations of the influence of bathymetric changes emanates from an impact of a 300 m sized meteorite into 1800 m deep water. The impact occurs on a platform-like bathymetric structure. However, in this context, the platform should not be seen as a carbonate platform, or as any geological feature of marine basins. It should only be seen as an artificial structure of a bathymetry in order to investigate the influence of the angle of the slope to higher water depths.

For the third experiment, a part of the Gulf of Mexico is used as a real bathymetry. In this bathymetry, the water depth in the impact area was changed

to guarantee a water depth of 1800 m. The artificial bathymetry is constructed with similar geometrical features, but with a linearly-changing water depth.

5.1 Varying Water Depth to Investigate the Influence on the Characteristics of the Rim Wave

Modeled impacts and Methods to Measure Wave Characteristics

As already mentioned, diameters of the impacting meteorites are constant at 300 m and the water depth varies from 300 m to 1800m. In Table 5.1, the parameters are summarized and names are allocated.

Table 5.1: Impacts used to investigate the characteristics of the rim wave

Water depth (m)	Diameter:Water depth ratio	Name
300	1:1	RI11
600	1:2	RI12
1200	1:4	RI14
1800	1:6	RI16

Along the train of the tsunami wave, the wave elevation is measured with time. Each gauge point has a record of the pass of the rim and the collapse wave. For the consideration of the wave period, the different part of the passing rim wave are investigated. Since the gauge record (Fig. 5.1) gives the wave elevation as a function of time, the time span in which wave crest passes the gauge point is, here, referred to as the *duration of the wave crest*, and *duration of the wave trough* for the pass of the wave trough, respectively. From this graph, the period T and amplitude of the rim wave η_{rimmax} , the maximum elevation of the rim wave, can be measured. The accuracy of the wave period depends on the spatial resolution in the SALE code, which were 20 and 25 m.

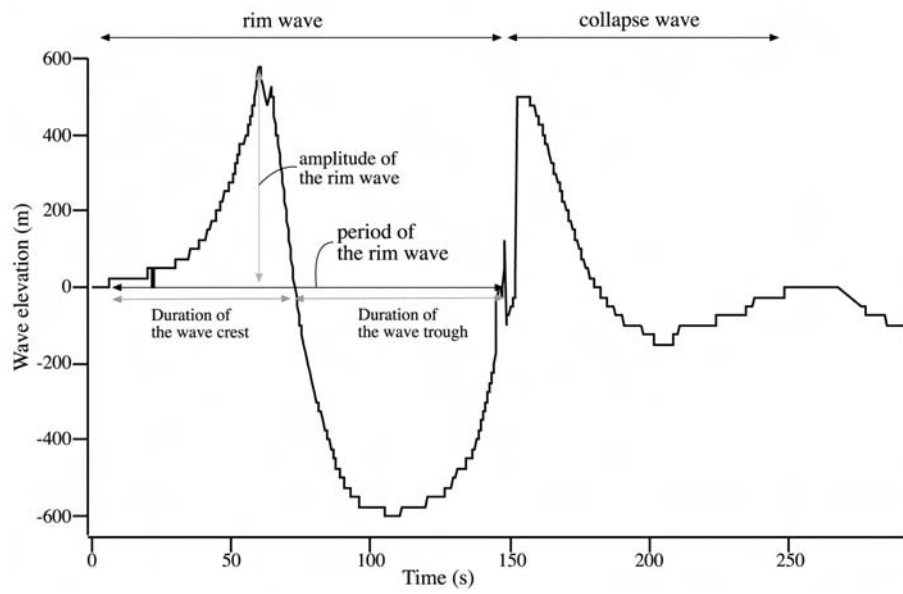


Figure 5.1: Illustration of the method of measuring amplitude, period, duration of the crest and duration of the trough of the rim wave.

Characteristics of the Rim Wave

The data set to investigate the characteristics of the rim wave were derived by the procedure described in the last section. Fig. 5.2 illustrates the data as functions of time.

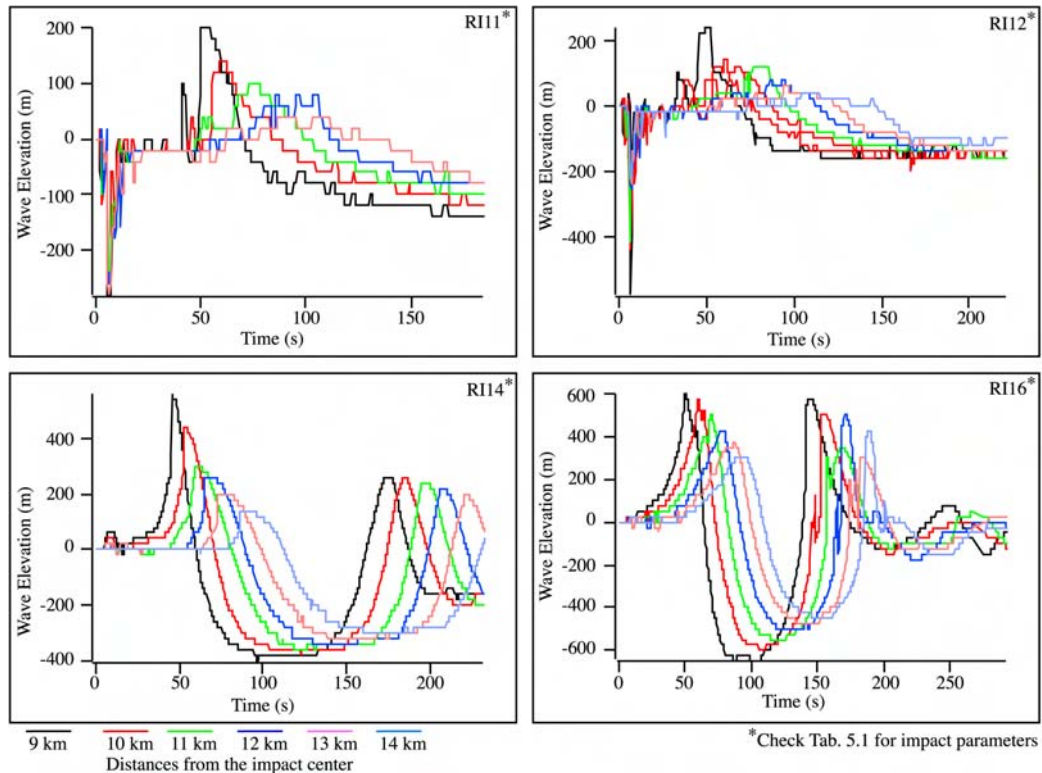


Figure 5.2: Time series of gauge records in certain distance from the impact center to investigate the early evolution of the rim wave.

The graphs show different complex courses that are due to the water depth to spatial resolution ratio. Even if the course of the graphs for RI11 and RI12 (water depth/spatial resolution: 12 & 24) are very stepped, the crest of the rim wave can be discovered. For RI14 and RI16, the course of the graphs are very smooth and reflect the rim wave very clearly. As mentioned, this section is dedicated to investigate the influence of the water depth on the characteristics of the rim wave and its early evolution in the near of the impact. Impact RI16 is used for the further experiments, too.

Results–Wave Height

The following graphs give the maximum values for the crest and trough of the different impacts at the respective distances from the impact center. The analysis

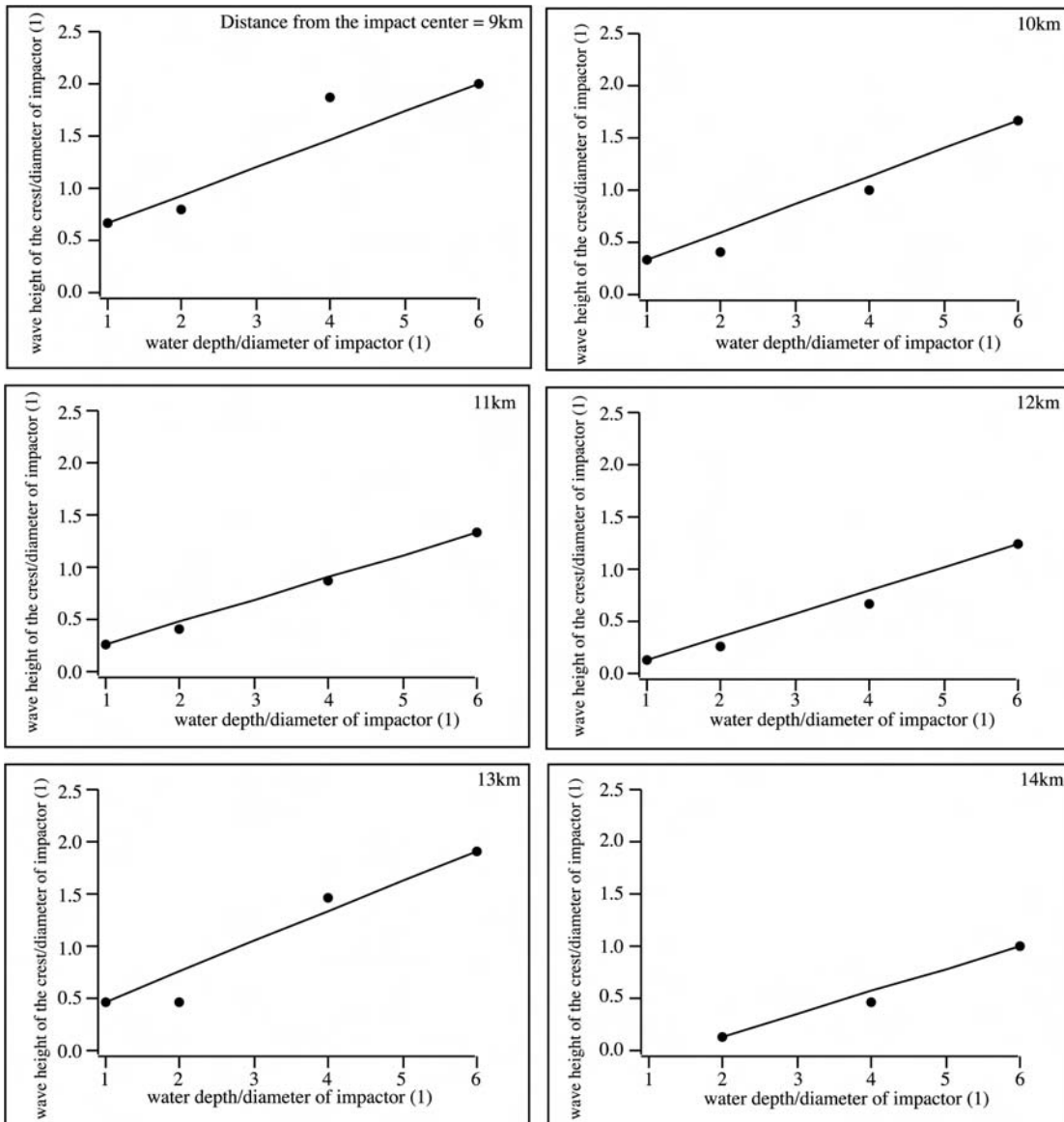


Figure 5.3: The wave amplitude of the rim wave as a function of the waterdepth.

of this data is based on linear relationship between the wave amplitude and water depth (impactor diameter). The wave amplitude and the water depth are given in dimensionless form by the ratio of the actual wave height or water depth and

the diameter of impactor. The line in these diagrams represents the a straight line between the first point at 300 m water depth and the last one at 1800m water depth. In case of the 300m water depth, it was not possible to get reliable wave heights for a distance of 14 km from the impact point.

Data points are below and above the line. This fact supports the assumption of linear relationship. The line also represents an interpolation graph. The equations of such a graph is $f(x) = a \cdot x + b$. However, it can be emanated from a dependence of parameters a and b from the distance of the gauge points to the impact center. As a first approximation, this dependence might also be assumed as linear. Assuming this, a two-dimensional equation is achieved:

$$A(x, y) = (cy + d)x + ey + f = cyx + dx + ey + f \quad (5.1)$$

$A(x, y)$ is the amplitude of the rim wave, x represents the water depth and y the distance to the impact center. For RI11 to RI16, the parameters of equation nnn are:

$$\begin{aligned} c &= -0.01 \\ d &= 0.36 \\ e &= -0.14 \\ f &= 1.706 \end{aligned} \quad (5.2)$$

Further condiseration, especially, of parameters d and f could involve the diameter of the impacting meteorite. Equations nn and nn+1 can be used for interpolation. However, under strict condition a careful extrapolation is also possible. For interpolation, an error of approx. 10% should be assumed. An extrapolation lets the error grow nonlinearly which growth rate is not predictable.

Wave Period

The investigation of the wave period is split into an analysis of the passing wave crest and trough at the gauge points, being defined as the duration of the wave crest and duration of the wave trough. Fig. 5.1 illustrates the apparent difference in the duration of the wave crests and troughs. This difference is due to the fact that the generation of the rim wave cannot only be ascribed to collapse of the crater rim of water (see Fig. 3.9). The beginning surge of water back into the

crater structure results in an enlargement of the wave trough (Fig. 3.9). In case of RI11 and RI12, it was not possible to record the entire rim. Since RI13 could be recorded completely, missing durations of the wave troughs of RI11 and RI12 could be estimated with the help of RI13. Fig. 5.4 gives durations of wave crests and troughs at 9 km, 10 km, 11 km, 12 km, 13 km and 14 km from the impact point.

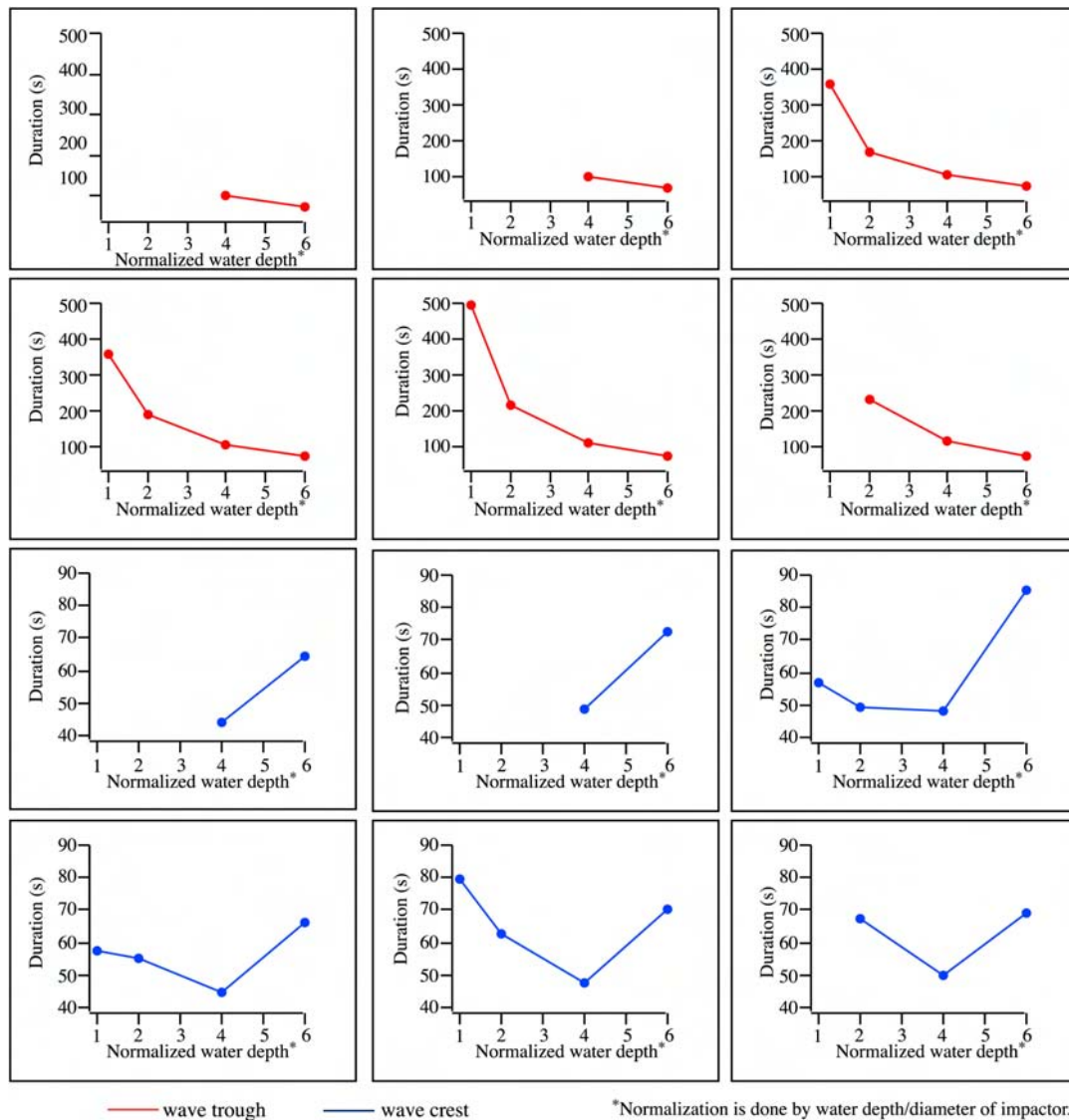


Figure 5.4: Durations of the wave crest (blue) and trough (red) in different distances from the impact point as functions of water depth in the impact area.

The wave troughs, marked by the red graphs, obey a negative trend; but is difficult to argue that it is a linear one. This assumption is supported by the courses of the wave crests in blue. Therefore, a simple linear analysis cannot be carried out; another kind of analysis is beyond the focus of this section, but the number of impact experiments is not high enough to guarantee reliable results. The reason for a nonlinear relationship is probably due to nonlinear dispersive processes during the collapse of the crater rim of water. An alternative explanation is given in the next chapter.

How to get insights into the wave period

Actually, the discussion about how to get a more detailed insight into the wave period dependent on the water depth in the impact area should be given in section *Summary and Outlook*. However due to the problems in using a linear analysis, it is necessary to briefly discuss this right after data are presented.

The computational limitations of the SALE hydrocode are discussed in the next section, but it is the only code with which it is possible to carry out simulations of impacts into oceanic environments from the beginning until later water movements where the impact cratering is long over. However, exactly these limitations prevent a very careful analysis of simulated impacts. The main problem is the spatial resolution. This sounds like criticism. Actually it is not because the SALE hydrocode is still under development and recent improvements have even made it possible to compute impacts with the parameters given by table 5.1. A careful analysis would presume a finer spatial resolution. Just half a year ago, a spatial resolution of 20m or 25m were not even possible. If the spatial resolution were finer than this, the collapse of the crater rim would be simulated more reliably because turbulent and highly nonlinear processes were represented more precisely.

Theoretical Consideration about the Characteristics of the Rim Wave

Computing oceanic impacts has several limitations. To achieve reliable movements of the water layer, a number of 6 (better 10) computational grid cells have to be located within the water column (Wünnemann, pers. commun.). That means the vertical spatial resolution depends on the thickness of the water

column. The aspect ratio of the cell ideally is 1.0 and so the horizontal spatial resolution depends on the thickness of the water column, too. If an impact into shallow water is considered, the bolide and the target are discretized with this spatial resolution. Depending on the size of the impactor and the horizontal extension of the target, this may lead to the limit of the computability regarding machine limits (array sizes and memory of the used computer system) and the run time of the model.

The kinetic energy of a bolide is transformed into other types of energy. The impact involves material of the half space below the the impact point. Therefore, it can be assumed that the energy which is transferred to the water column, responsible for the generation and propagation of tsunami waves, is a certain portion of the original kinetic energy of the impactor. Qualitatively it can be assumed that this portion has a limit, meaning it does not grow linearly with decreasing water depth (constant kinetic energy of the impactor). Quantitative calculations based on the wave energy of tsunami waves are not possible because in impact cratering, hydrodynamic and thermodynamic processes overlap each other. Hence, hydrodynamic approaches would give spurious results. Therefore, only a qualitative consideration is possible. Fig. 5.5 proposes such a qualitative model regarding the limit of the characteristics of the resulting rim wave.

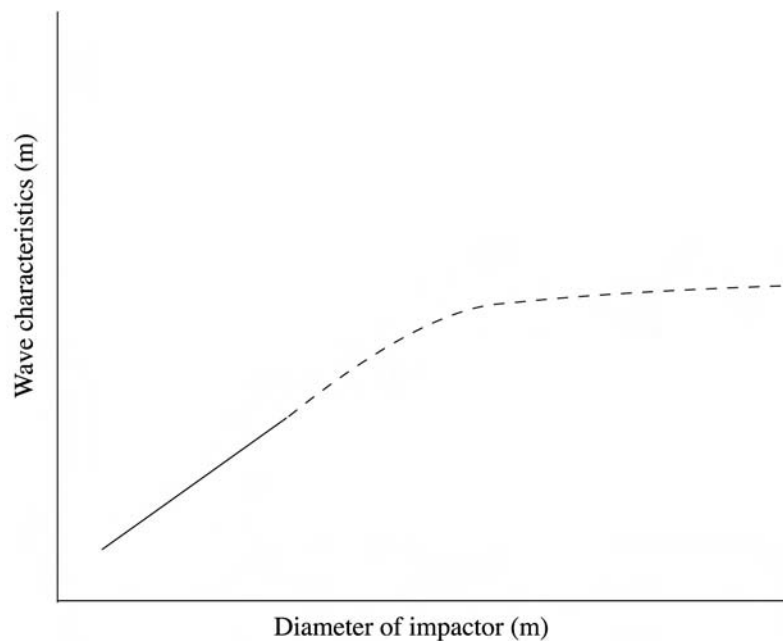


Figure 5.5: Qualitative model of the limit for a resulting rim wave.

The solid part of this graph can numerically be proven (Weisz et al., 2003). The dashed line represents parameter constellations which are not possible to simulate using SALE. They are not possible owing to the limitations described above. When it is possible to compute such constellations, it should be possible to scale characteristics of the rim wave, even in the saturated zone.

An alternative approach to tackle this problem could be an envelope, represented by the dashed line, of a more complex course of wave characteristics as a function of the diameter.

If the wave characteristics as a function of the diameter of impactor would have a course as proposed by Fig. 5.5, it is theoretically possible to find a scaling law to mathematically link both parameters. However, if the envelope were the right approach, the potential complexity of the course of the graph would prevent the setup of useful scaling law. An scaling law for the envelop is not appropriate tool for further quantitative analyses.

The Collapse Wave Problem

As qualitatively described in section 3.3 *Oceanic Impacts*, collapse waves are generated due to the collapse of the central peak of water which is a result of the resurgence of water into the crater cavity. Fig. 5.6 gives a series of snapshots, depicting the generation and the early evolution of the collapse wave. The crest

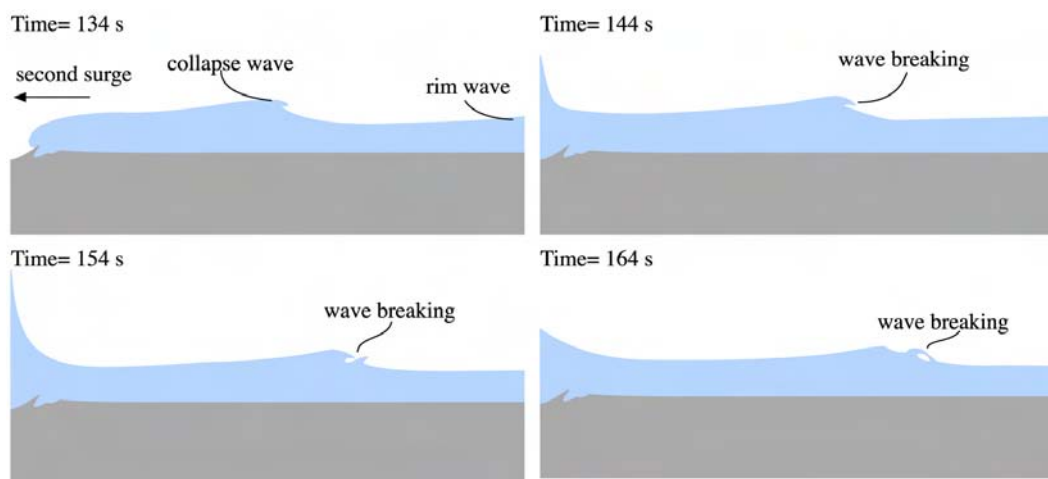


Figure 5.6: Snapshots illustrate the generation of the rim wave and the collapse wave by oceanic impacts.

of the rim wave has almost propagated out of the panel at the right side. The breaking of the collapse wave is represented by the turbulent structures at their front. However, the process of wave breaking is not precisely simulated because the spatial resolution of SALE is not appropriate for this task. From a hydrodynamical point of view, this breaking cannot be ascribed to the wave parameters (wave steepness, Fig. 3.1); rather it is a relict from the generation process of the collapse wave, especially the superposition of a weak resurgence of water into the crater structure and the collapse. This fact supports the subdivision of oceanic impacts into three different categories (section 3.3 *Oceanic Impacts*).

The breaking of the wave is not expected for large water depths as presented by in Ward and Asphaug (2000, 2003); Ward (2000). (see also Fig. 4.n). They only consider cases where the meteorite is absorbed within the water column. However, the linear theory, that is applied by Ward and Asphaug (2000, 2003); Ward (2000), use does not include wave breaking.

5.2 Bathymetric Variations affecting Tsunami Wave Propagation

The global evolution of a tsunami wave is the superposition of local bathymetric variations along the wave train. Positive and negative gradients determine the development of the wave characteristics. Investigations in this chapter focus on the wave height as a function of the distance to the impact point.

Experimental Setup

In order to investigate the influence of bathymetric variations on the wave height, as an example, an impact on a platform with 1800m deep water is assumed. From the platform break, the water depth increases to 4500m with varying angles of slope. The upper panel of Fig. 5.7 introduces the structure of the computational domain. Along the solid line (A to A', upper panel of Fig. 5.7) the wave height is recorded at each grid point out of the impact area. The lower panel of Fig. 5.7 shows a section along the section A-A'. The angle of slope varies from 1:10 to 1:90 (by steps of 10). The general form of angle is $1 : \tan(\alpha)$, where *alpha* is the actual angle of the slope.

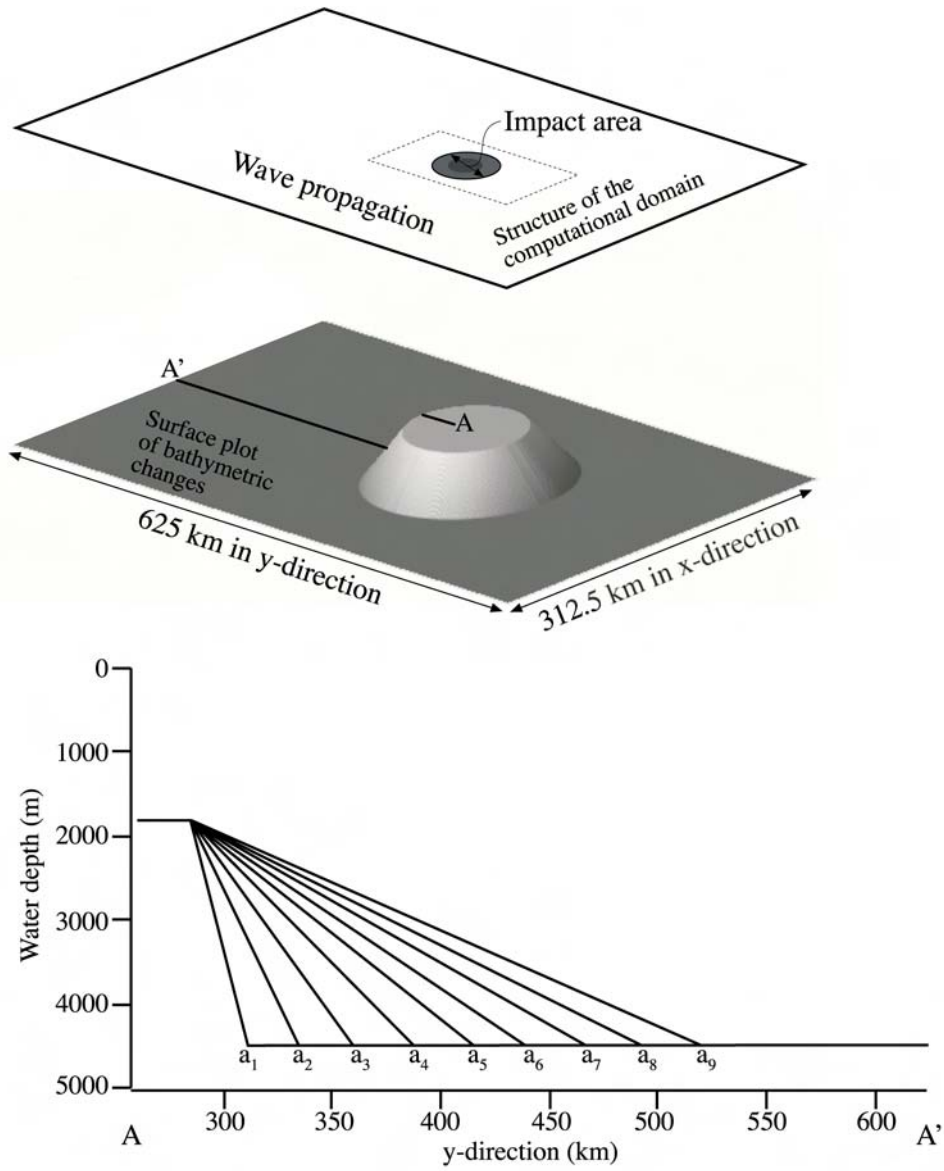


Figure 5.7: Structure of the computational domain for the experiments and bathymetric changes.

Data Set

The result of recoding the wave height are time series. Fig. 5.8 gives the time series for each angle of slope. The pattern looks very similar but the identification of the maximum as function of location will show the differences.

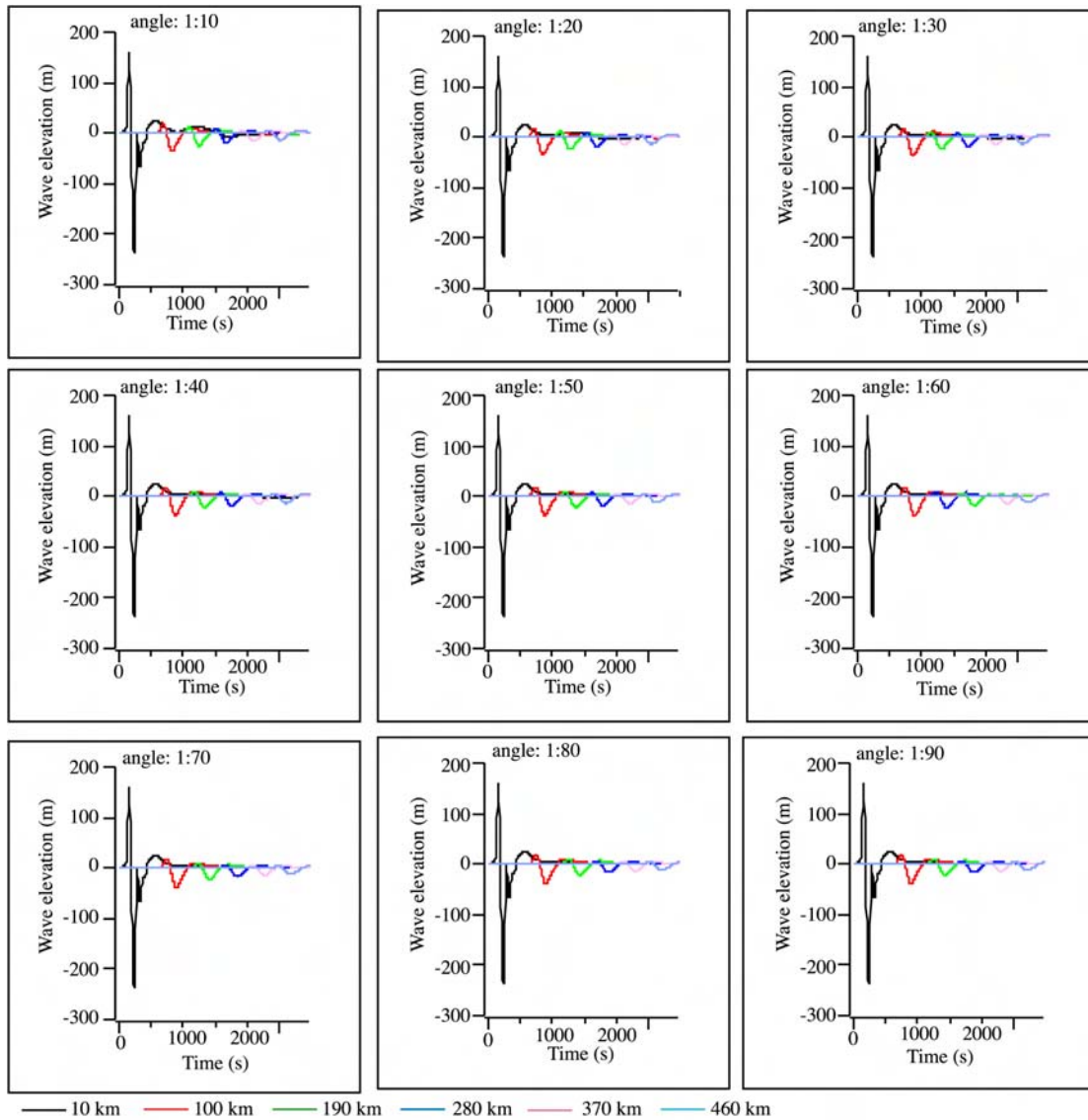


Figure 5.8: Time series for each angle of the slope in distances of 10, 100, 190, 280, 370 and 460 km from the impact area.

Results

The different angles of slope result in a different behavior in the respective areas. The maximum elevation of the rim wave is depicted in Fig. 5.9. The curvature of the graphs up to approx. 20 km from the impact point is due to nonlinear processes in the early phase of wave propagation. The linear parts of the graph

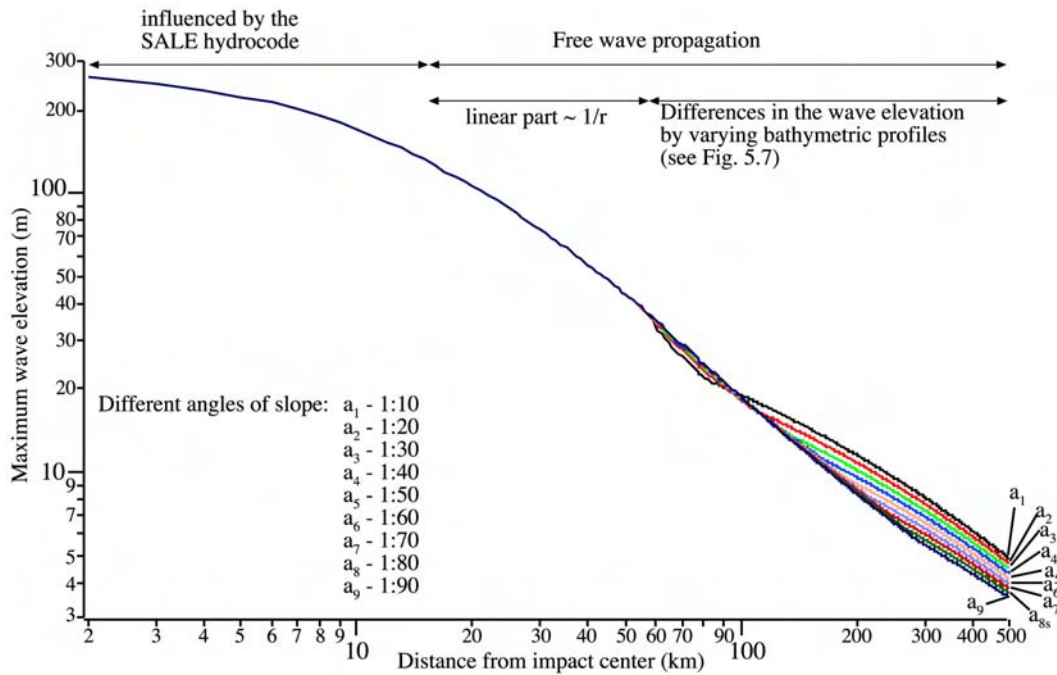


Figure 5.9: Log-log plot of the data for different angles of slope.

follow the $1/r$ relationship. 55 km from the impact point, the water depth linearly increases with angles between 1:10 to 1:90. Fig. 5.0 shows that a steep slope has a positive effect on the maximum wave elevation. However, it should be mentioned that the propagation over moderate to mild slopes takes longer. And so, the weakening of the wave height is more effective. Maximum wave elevations of a_1 and a_9 (see Fig. 5.9) at 500 km from the impact point ranges between 4.5 and 5.5 m. Thus, the effect of different angles of slope still exists, but taking the dynamic range from 4 to 250 m of the maximum wave height as a function of the distance into account, the actual effect seems to almost negligible in terms of the propagation. However during the shoaling of a wave towards the shoreline, the wave height is multiplied up to 6 (Ward and Asphaug, 2000) resulting in wave heights in coastal areas of 27 m for a_9 and 33 m for a_1 .

5.3 Comparison of Wave Evolution over linear and "real" Bathymetries

This section considers the impact RI14, impacting on a platform. Two different bathymetries, an artificial and "real" one are used as the basis of the wave propagation simulations.

Bathymetric Data

Fig. 6.1 illustrates both bathymetries. The structure of the computational domain is the same as introduced in Fig 5.7. For this numerical experiment, the runup of the respective waves is also taken into account. As usual, the wave elevation as function of time and space are gauged along the solid line. The loc-

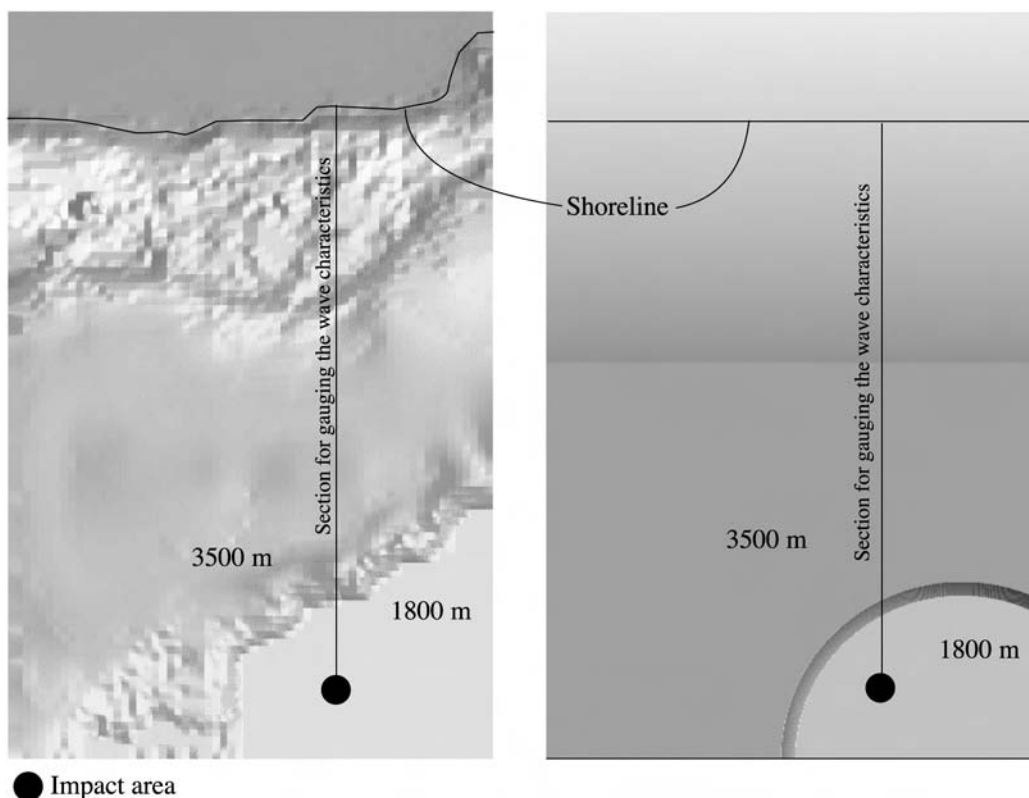


Figure 5.10: Left: a real bathymetry. Right: linear bathymetry

ation of the impact in case of the real bathymetry corresponds the same relative

position as for the artificial one. The spatial resolution in both simulations is $500m$.

Wave Propagation

With the help of the time gauges, the maximum wave elevation as a function of the distance can be determined as demonstrated in the last chapter. The differences in the course of both lines can be ascribed to the locally different gradients of the bathymetry. As the local gradient is here supposed to be defined as higher

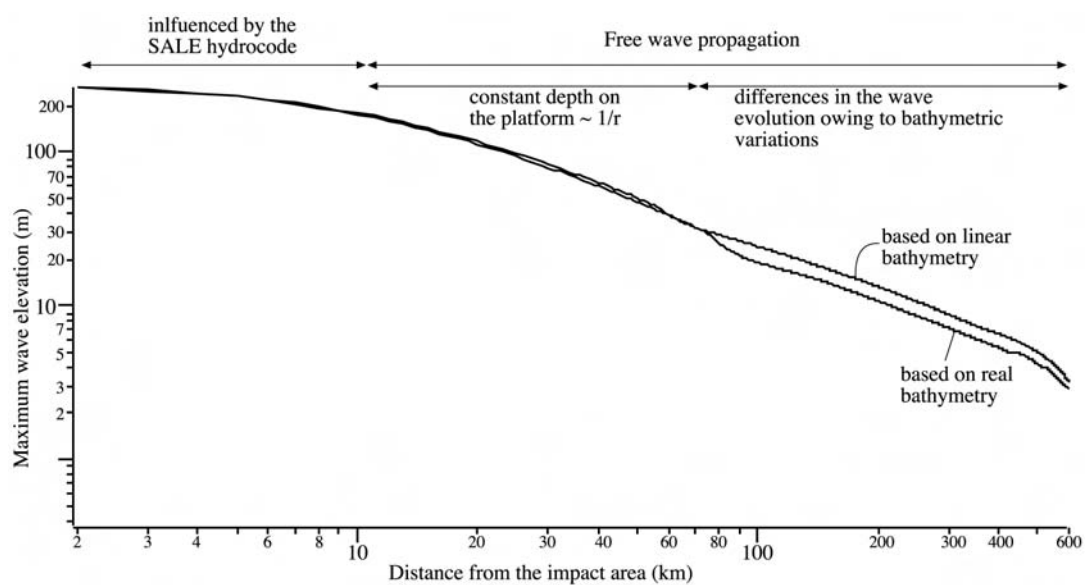


Figure 5.11: Maximum wave elevation as a function of the location.

order variations in the water depth the major gradients of the platform and beach slope. As already discussed in the last chapter, differences in the maximum wave heights are negligible for the entire dynamic range of wave heights along the train of an impact-induced tsunami wave.

Runup

The runup along the x -coordinate is given in Fig. 5.12. The complexity of the course of the runup along the shore is due to the variations in the depth in the coastal area. Depth variations of the linear bathymetry are very smooth. Therefore, the course of the runup curve is very simple. The complexity increases

of the runup curve for the real bathymetry. This can be ascribed to the nonlinear variation of the water depth in the coastal area.

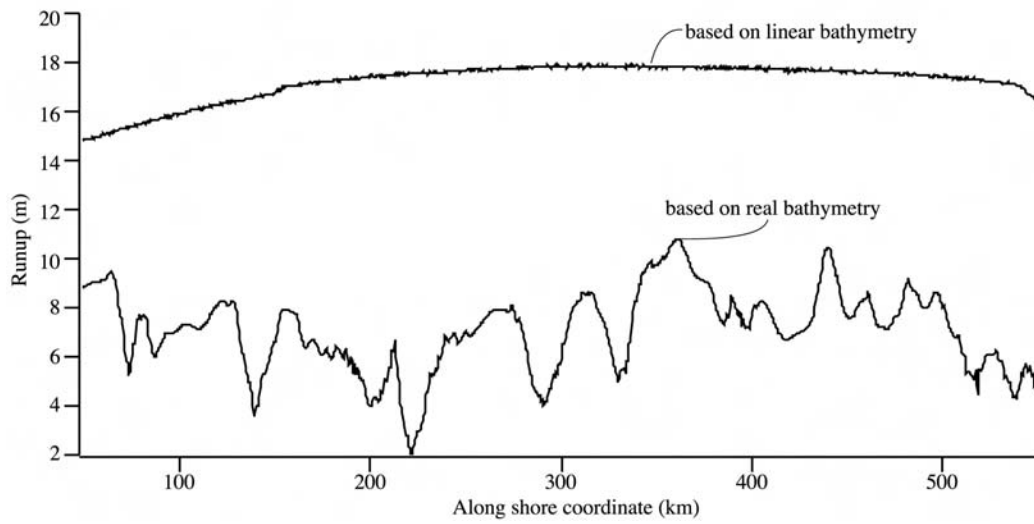


Figure 5.12: Runup along the coast.

Chapter 6

Outline of Some Geological Implications from Modeling Impacts and Wave Propagation

The apparent gaps between observations and implications of numerical simulations have existed always owing to the limitations of the theoretical approaches. The implementation of theoretical approaches is also affected by the development and improvement of hardware components of computers (Merriam, 2004).

Each process in the geological past is preserved in a geological record. The investigation of such a record is either an investigation of the products of a process, or it represents a snapshot of an ongoing process. Thus, the number of possible interpretations is very high. Numerical modeling of processes may help to understand a process or, in general, to find a process which is responsible for a certain geological record. This results in limiting the number of possible interpretations. Quantitative and qualitative results, obtained in the previous chapters, allow implications of a potential oceanic impact for both the impact area and the surrounding coastal areas.

The example, given in sec. 5.3. is to demonstrate the capability of numerical modeling to derive implications of general geological meaning. Especially from a sedimentologic point of view, displacements of water can be used to get geological implications. Such movements are on the one hand the surge of water back into to crater cavity and on the other hand the propagation of the impact-induced tsunami waves and the runup behavior. In this context, the Hjulström–Sundborg diagram gives conditions for erosion, transport and sedimentation in aquatic and

aeolian sedimentary systems. Neglecting the aeolian part of the diagram, Fig.6.1 illustrates a simplified redrawing of the Hjulström–Sundborg diagram.

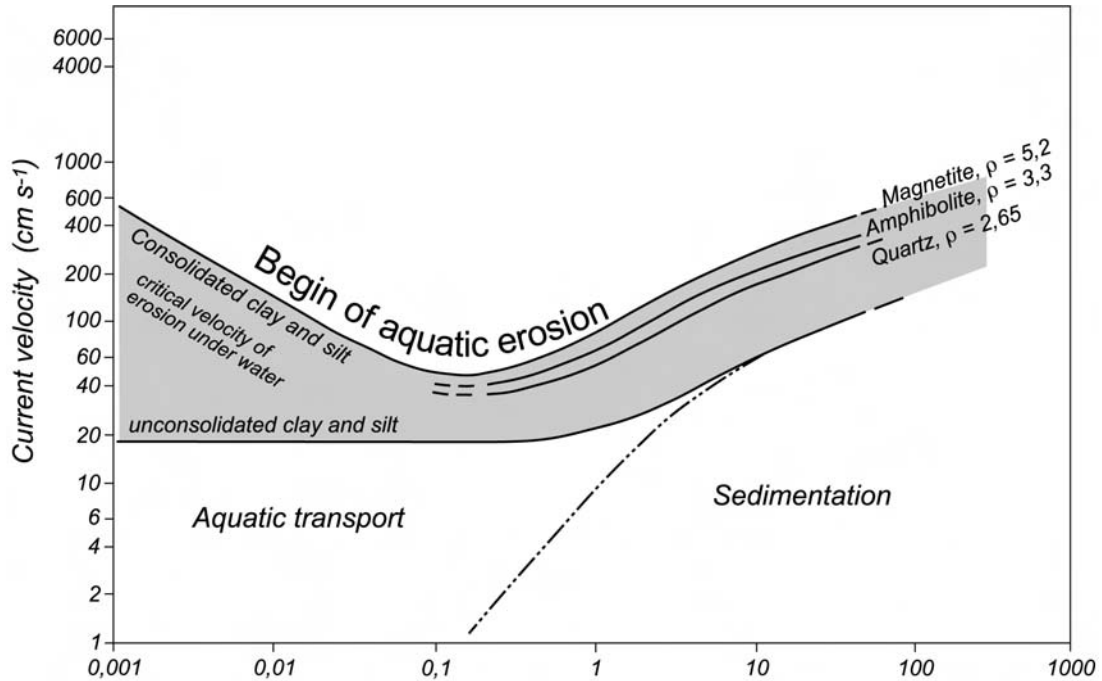


Figure 6.1: Simplified redraw of the Hjulström–Sundborg diagram (redrawn according to Chorley et al., 1984).

Simple measurements of the flow–velocities of the surge of water into the crater cavity and during the wave propagation already yield informations which are basic for the understanding of the sedimentologic features in deposits generated by such water movements. These informations are applied to the back–wash in the case of the Chicxulub impact event.

6.1 Additional Modification of the Crater Cavity

As described in chapter 2 *Impact Cratering*, impact cratering is generally subdivided into three different stages: contact and compression stage, excavation stage, and modification stage. The excavating cavity subjects to gravitational processes which determine the final shape of the crater. The processes taking place are summarized in the modification stage. Among all processes, resulting in modifications of the crater cavity, there are processes occurring in both contin-

ental and oceanic impacts. However, specific processes only take place in case of an oceanic impact. They mainly are linked to the occurrence of a water column. Weisz et al. (2003) referred such modifications to as additional modifications. The velocity of the water masses surging into the crater cavity is the controlling parameter for this modification. Sedimentologic evidences are located among deposits which are related to the impact cratering. They have not been described in the literature, so far. Fig. 6.2 shows snapshots (a-d), illustrating the surge of the water back into the crater cavity.

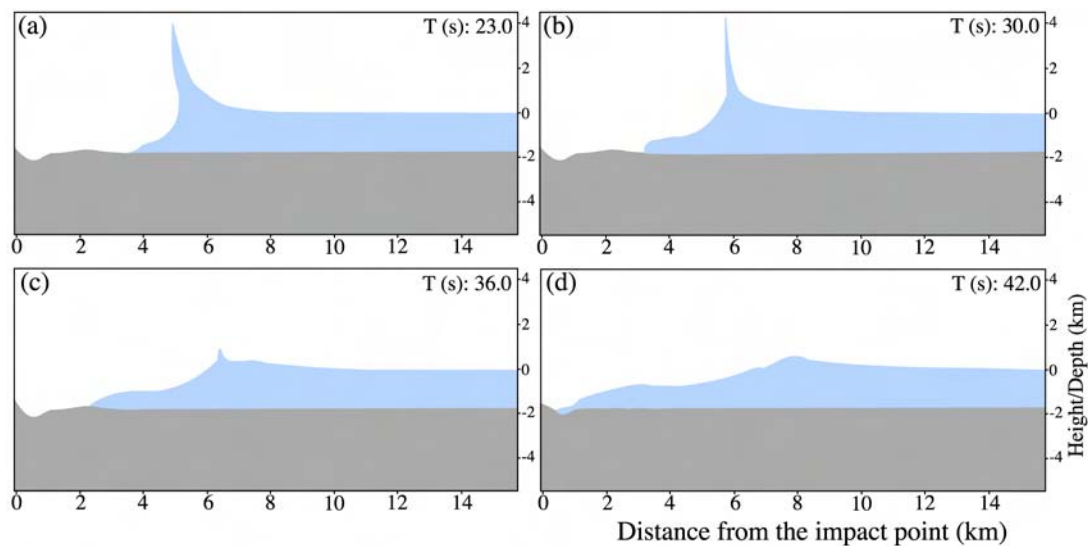


Figure 6.2: Illustration of the surge of water into the crater structure. The surge begins during the collapse of the crater rim of water.

With the help of such snapshots, the velocity of the surge front can be calculated. Assuming a depth-averaged velocity profile just behind this front, the resulting velocities can be used to assess the mode of a possible sedimentary system, meaning whether erosion, transport, or sedimentation occurs. However, the front of the surge moves with an average velocity of 20 m/s (2000 cm/s in Fig. 6.3). The maximum velocity is 28 m/s (2800 cm/s in Fig. 6.3) and the minimum one is 4 m/s (400 cm/s in Fig. 6.3).

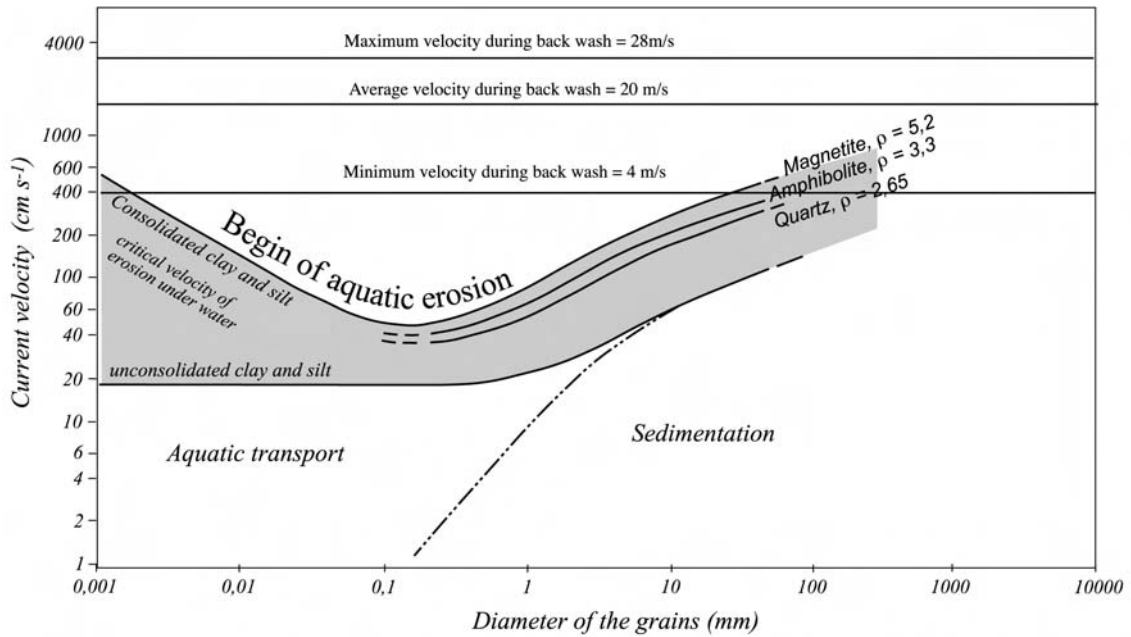


Figure 6.3: An extended Hjulström–Sundborg diagram to illustrate the mode of a possible sedimentary system of the surge of water back into the crater cavity.

The minimum velocity is obtained at the beginning of the surge. The velocity steadily increases during the surge up to the maximum velocity. The kinetic energy during the surge is transferred from the potential energy of the water column. Hence, the velocity during the surge depends on the thickness of the water column. Apart from the beginning of the surge, the velocity implies an erosional mode of the sedimentary system (Fig. 6.3). Assuming a linear relationship between the diameter of grains, current velocity and the mode of the sedimentary system as a first approximation, for surge velocity above the average velocity only erosion occurs. It should be mentioned that this implication assumes a linear relationship between the diameter of grains, current velocity and the mode of the sedimentary system, but the Hjulström–Sundborg diagram is given in log–log coordinates, implying that it cannot be drawn a simple straight line in Fig. 6.3. A possible extrapolation would be almost parallel to the x-axis. The crater rim is made of unconsolidated chunks of varying size displaced during the excavation stage. The erosional mode of the sedimentary system during the surge into the crater cavity, as displayed in Fig. 6.3, implies that the erosion of chunks from the crater rim may be lifted and transported into the crater cavity over several kilometers.

The water masses surge into the crater cavity from all direction. They generate a peak in the center of the crater (in case of vertical impacts). Owing to the generation of this peak, an upwardly directed component is added to the velocity which shortens the length of the lateral velocity component. In the area where the peak is generating, the shortening of the lateral velocity component is very effective. As a consequence, transported material of all grain sizes is deposited in very short time. The collapse of the central peak results in velocity components that outwardly directed. However, the effective length of the lateral velocity component, which is a result of the superposition of the collapse of the central peak and ongoing surge into the crater, very short. Therefore, coarse material or chunks will not re-mobilized; but it is possible that material of sandy grain size will be eroded and transported again.

This implications are only of qualitative relevance. It is not possible to give velocities at which certain sizes of chunks will be eroded from the crater rim and transported into the crater. Furthermore, it not possible to draw conclusions on the sedimentary features of the deposited material from the surging water during the generation of the central peak. Only the combined modeling of impact cratering and sediment transport is able to result in quantitative informations from the surge of water into the crater. Since the velocity of the surge of water into the crater depends on the water depth, the implications achieved above can be applied to the filling of the Chicxulub crater.

6.2 Crater Filling after the Chicxulub Impact Event

In the 1980s arose the hypothesis of a meteorite hitting the earth 65 Ma ago. Evidences could be found in Italy and around the world in a cm thick clay layer. Alvarez et al. (1980) were the first who investigated respective clay layers and were also the first who promoted the impact hypothesis. The key point of this hypothesis is that an impactor hitting the Earth is supposed to be responsible for the extinction of 75% of the species (Sepkoski, 1993). The most prominent species among them are the Dinosaurs. The Ir-anomaly in a clay layer, also referred as boundary clay, supported the impact hypothesis (Alvarez et al., 1980). But the crater was still missing until the Hildebrand et al. (1991) presented their work. They found a circular structure approx. 1000m below the surface that looked

like an impact crater on the Yucatan peninsula. Fig. 6.5a gives the shape of the gravitational anomaly. A multi-ring morphology is readily to recognize. Since the

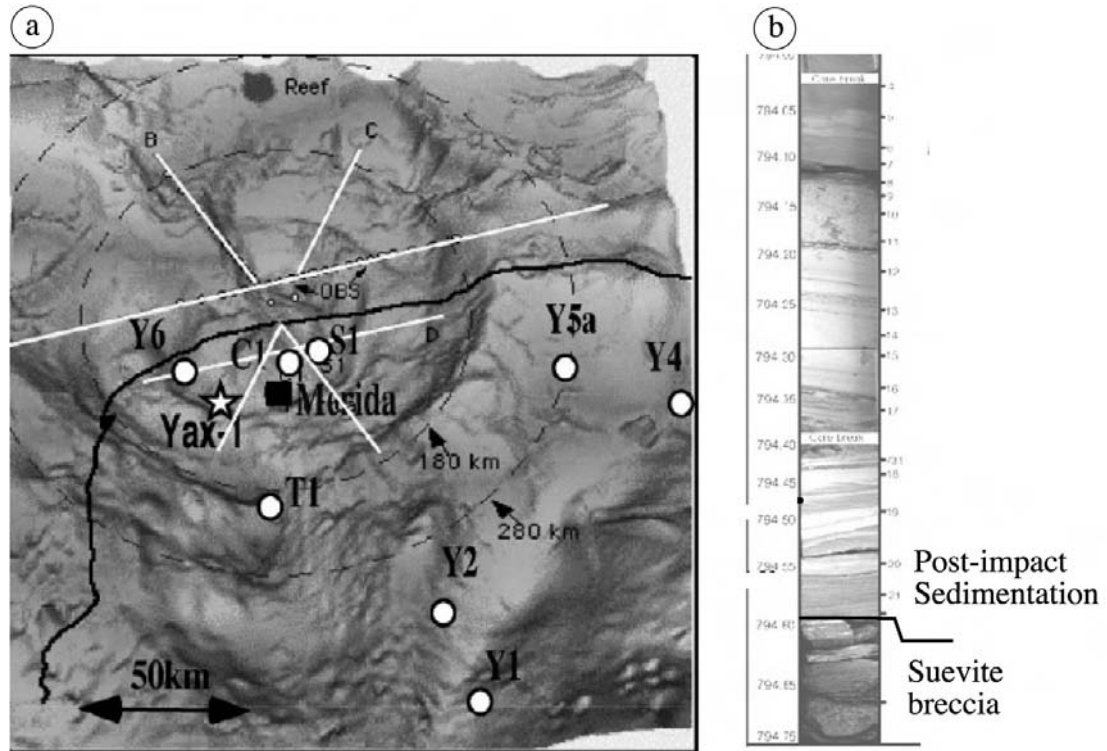


Figure 6.4: Left: The position of the drill hole Yaxcopoil-1 (Yax-1) in the Chicxulub crater based on the gravitational anomaly (Keller et al., 2004). Right: Core picture of the K/T transition (extracted from Keller et al., 2004).

crater is buried, the extension of the crater has to be concluded from geophysical data. With help of the gravitational anomaly and the seismic lines, it is possible to estimate the diameter of the crater. Unfortunately, both geophysical approaches obtained different numbers. From the gravitational anomaly, a crater diameter of 180 km to 210 km was concluded (Hildebrand et al., 1991); the interpretations of seismic lines yielded a diameter of 250 km to 270 km (Morgan and Warner, 1999). Besides the discussion on the size of the impact crater, there is also a heated discussion as to whether the Chicxulub impact represents the K/T boundary or not. From the diameter of the crater structure, the original size of the impactor can be estimated (Melosh, 1989). In case of Chicxulub, the impactor was 11km in diameter. Since the impact took place on a carbonate platform, the pre-impact water depth could no have been higher than 75 m (Tucker and Wright, 1990).

As described in the previous section, the velocity of the surge of water into the crater depends on the water depth because the kinetic energy of the surge is transferred from the potential energy of the water column. It means that the velocity of the surge owing to impact in a shallow water, like in the case of Chicxulub, is somewhat slower than the surge of an impact in deeper water. Another fact regarding the Chicxulub impact is the crater rim. The huge meteorite (11 km in diameter) caused a vast of material ejected in the atmosphere. A fraction of this ejected material is deposited and generated the crater rim. In case of a multi-ring basin, as the Chicxulub crater, such material covers the entire outer part of the crater (Melosh, 1989). The extension of the crater rim cannot be given because the crater is buried; but it may be expected that it is in same dimension of the water depth about 70 m or even higher. This fact and the decelerated surge in the direction of the crater lead to the assumption that the water masses are severely hindered by or reflected on crater rim. In both cases, the water uses permeable ways to flow in the crater resulting in a gully formation as in the case of the Lockne crater (Ormö and Miyamoto, 2002). In those gullies, sedimentary features imply energetic sediment transport, erosion and deposition. However, other areas, especially near the center of the crater structure, the water level slowly increases. In such areas, respective deposits indicate a low energy sedimentation. Fig. 6.5b gives a core section containing the end of the impact cratering and the beginning of the sedimentary life after. The end of impact cratering is marked by the suevite breccia. Just above this breccia, fine laminated limestones indicate a low energy sedimentation (Fig. 6.5b).

6.3 Erosion, Transport, Sedimentation along a Tsunami Wave Train

Along the solid line in Fig. 5.10, not only the wave elevation is measured, but also the velocity field. The two orthogonal components of the velocity field are combined to vectors. The length of a vector (given as the current velocity in Fig. 6.5) can be used in the Hjulström–Sundborg diagram to determine the mode of a possible sedimentary system for different grain sizes. The upper panel of Fig. 6.5 gives the maximum velocity along the wave train. The grey rectangular in the lower panel represents the dynamic range of the velocity which is between 0.9 (90 cm/s in Fig. 6.5) m/s and 30 m/s (3000 cm/s in Fig. 6.5).

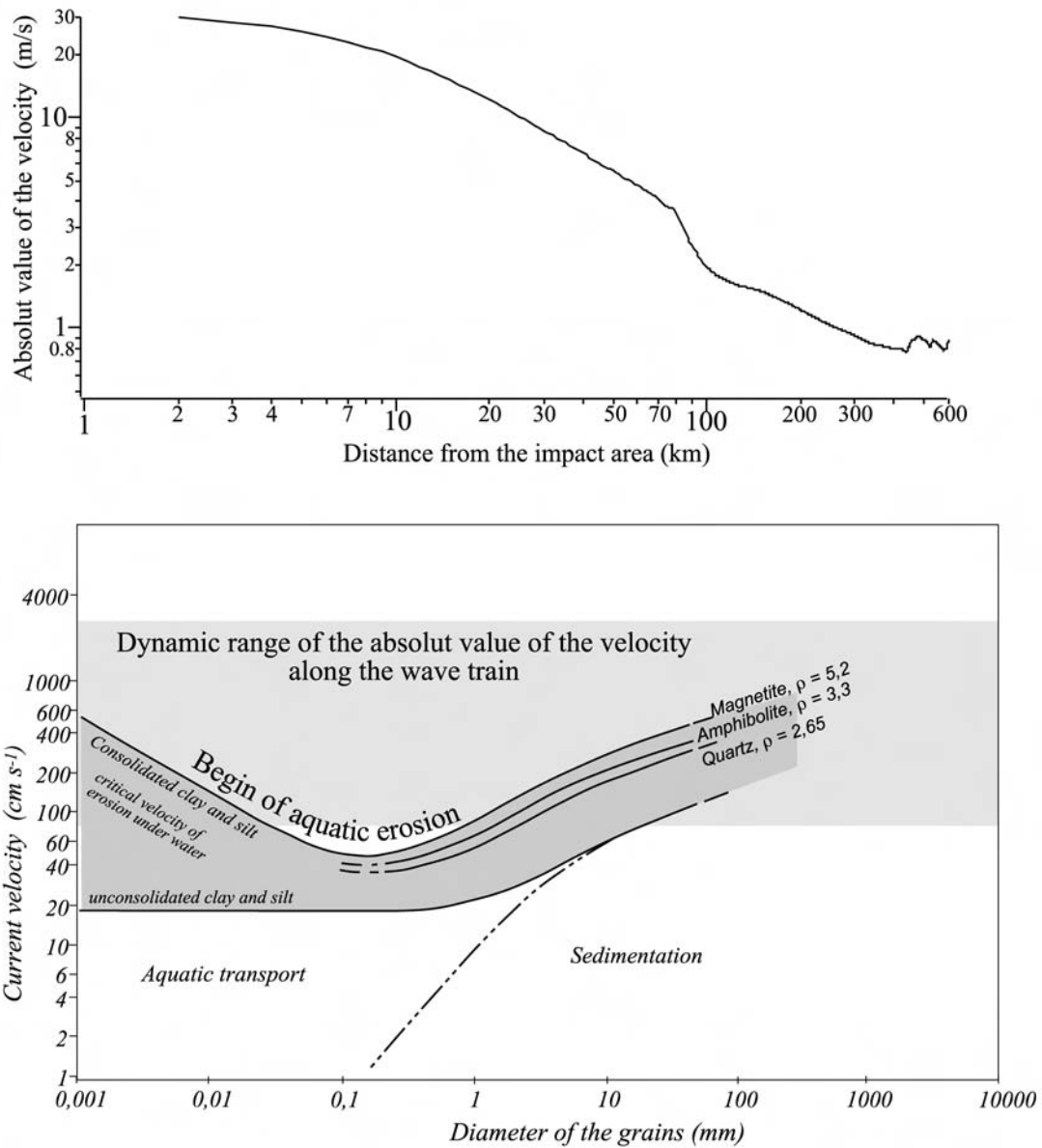


Figure 6.5: Upper panel: absolute value of the velocity along the tsunami wave train. Lower panel: The dynamic range of the absolute value of the velocity given in the Hjulström–Sundborg diagram.

For sandy grain sizes, only erosional conditions are expected along the wave train. Assuming sandy grain sizes all along the wave train, a sedimentologic feature is a erosional surface at the bottom of potential tsunami deposits. In coastal areas, it is very difficult, especially in ancient deposits, to distinguish between storm and tsunami deposits (Goff et al., 2004). Even if the physical processes are

completely different, the sedimentary products of storms and tsunami waves resemble in coastal areas. Taking the erosional condition along the train of tsunami waves into account, a distinction can be achieved if it is possible to follow the erosional base of a sediment layer below the wave base.

Tsunami deposits, found at recent beaches, are the result of the runup of tsunami waves. Depending on the pre-tsunami sedimentologic structure of a beach section, a tsunami wave results in a redistribution of sediments. It is even possible that blocks of the size of a house are lifted and transported over 10's to 100's of meters (Scheffers and Kelletat, 2003). The runup process which leads to those sediments, is a highly non-linear process, especially if the interaction with bottom sediments is taken into account. Therefore, it is highly speculative to extend the qualitative approach, given by Fig. 6.5 to the runup process.

Chapter 7

Summary and Outlook

The major outcome of this thesis is the establishment of 2D propagation code for tsunami waves. This hydrodynamic model uses the non-dispersive shallow water equations and a linear version of the dispersive Boussinesq equations. Especially the dispersive equations are important for the simulation of a long-distance wave propagation. The SALE hydrocode in its newest release is used to compute the impact cratering. This code is maintained by Kai Wünnenmann. A transition between SALE and the wave propagation was created as a mean step from the impact cratering to the free wave propagation. Both codes were used in determining answers that were asked at the beginning of this thesis:

1. How are tsunami waves generated by oceanic impacts?
2. In which way does the water depth influence the characteristics of the initial tsunami wave?
3. How do bathymetric changes (e.g. angle of the platform slope) influence the global evolution of a tsunami wave
4. What are the differences between a real bathymetry wave evolution compared to a linear one? What geological implications can be drawn from modeling impacts and tsunami wave propagation?

To answer the first two question, the SALE hydrocode was used. With the help of this code, general insights into how tsunami waves are generated by oceanic impacts, resulting in the identification of the rim wave and the collapse wave. Furthermore, three classes of oceanic impacts could be subdivided: impacts into deep, intermediate and shallow water. In case of shallow and intermediate

water, the rim wave is the main wave of the tsunami wave train, while in case of an impact into deep water, the collapse wave plays the master role. In this case, it is even possible that the number of the generated collapse wave is large due to free oscillation of the water column if the impact did not penetrate to the sea floor. The initial wave amplitude and period of the rim wave were investigated to give insights into the influence of impact parameters on the tsunami waves. For the wave amplitude a linear analysis yielded a positive relationship to the pre-impact water depth. Unfortunately, the same analysis was not possible for the wave period. Nonlinearities and a coarse resolution were found to be the reason for this. However, it should be mentioned that the spatial resolution has been increased extremely in the last year by the work of Kai Wünnemann. A general hypothesis of the characteristics of the rim wave as a function of impact parameter is also proposed.

To give an answer to the third question, the wave propagation was run based on a number of different bathymetries. A positive effect with an increasing angle of slope could be identified. However, the effective difference is rather small compared to the dynamic range of the wave elevations. The actual value is only important when the wave elevation amplifies. The geological implications can be listed as following: (a) The surge of water back into the crater is powerful enough to erode large fractions of the crater rim and transport them into the crater cavity. (b) The sedimentary system along a tsunami wave train is only in erosional conditions, implying that tsunami deposits might be identified by a erosional surface below the storm wave base. (c) In case of the Chicxulub impact, the crater rim was high enough to prevent a powerful surge of water into the crater cavity. The water masses were even reflected at the crater rim. The filling of the crater structure with water might last long enough to allow the generation of still water sediments. Finding answers to these questions was only possible by the development of a 3D wave propagation model which is based on non-dispersive and dispersive equations. The runup of waves was computed by the MOST code.

During the work on the questions above, not only answers were found but also new questions arose. Theoretical and modeling work in geosciences are only useful when observations can confirm their results. The geological implication of this thesis are of qualitative answers with only yes or no. To really confirm or deny the results of models, quantitative informations are necessary. In case of the surge of water back into the crater cavity, a coupling of the SALE hydrocode

to sediment transport model would give insights into the mode of erosion. The same is valid for the sedimentary system along the tsunami wave train. Especially for coastal areas, the implementation of the 4D wave/current model is crucial in combination with a sediment transport model.

Bibliography

- Abels, A., Plado, J., Pesonen, L., and Lehtinen, M. (2002). *Impacts in Precambrian Shields*, chapter The impact cratering record in Fennoscandia, pages 1–58. Springer Heidelberg.
- Alvarez, L. W., Alvarez, W., Asaro, F., and Michel, H. V. (1980). Extraterrestrial cause of the cretaceous–tertiary extinction: Experimental results and theoretical interpretation. *Science*, 208(4448):1095–1108.
- Amsden, A. A., Rupel, H. M., and Hirt, C. W. (1980). SALE: a simplified ALE computer program for fluids at all speeds. Technical Report LA–8095, Los Alamos National Laboratories.
- Bahlburg, H. and Claeys, P. (1999). Tsunami deposit or not: the problem of interpreting the siliciclastic KT sections in northeastern Mexico. In *ESF–Impact workshop 'Oceanic impacts: mechanisms and environmental perturbations'*, pages 19–20. Berichte zur Polarforschung 343/99.
- Beji, S. and Nadaoka, K. (1996). A formal derivation and numerical modelling of the improved Boussinesq equations for a varying depth. *Ocean Engineering*, 23(8):691–704.
- Bohor, B. (1996). A sediment gravity flow hypothesis for siliciclastic units at the K/T boundary, Northeastern Mexico. *Geological Society of America special paper*, 307:183–195.
- Bourgeois, J., Hansen, T., Wiberg, P., and Kauffmann, E. (1988). A tsunami deposit at the Cretaceous–Tertiary boundary in T. *Science*, 241:567–570.
- Brown, E. (1999). *Waves, tides and shallow–water processes*. Butterworth & Heinemann.

- Bryant, E. (1991). *Natural Hazards*. Cambridge University Press.
- Bryant, E. (2001). *Tsunami—The Underrated Hazard—*. Cambridge University Press.
- Chorley, R., Schumm, S., and Sugden, D. (1984). *Geomorphology*. Methuen.
- Chyba, C. F., Thomas, P. J., and Zahnle, K. (1993). Tunguska explosion: atmospheric disruption of a stony asteroid. *Nature*, 361:40–44.
- Dudley, W. and Lee, M. (1998). *Tsunami!* University of Hawai's Press, 2nd edition.
- Ferziger, J. and Peric, M. (2002). *Computational methods for fluid dynamics*. Springer Heidelberg, third edition.
- Fryer, G., Watts, P., and Pratson, L. (2004). Source of the great tsunami of 1 april 1946: a landslide in the upper Aleutian forearc. *Marine Geology*, 203:201–218.
- Gault, D. and Sonett, C. (1982). Laboratory simulation of pelagic asteroidal impact: Atmospheric injection, benthic topography and the surface wave radiation field. *Special Publication of the Geological Society of America*, 190:69–92.
- Gault, D. E., L. Quaide, W., and Oberbeck, V. R. (1968). Impact cratering mechanics and structures. In French, B. M. and Short, N. M., editors, *Shock Metamorphism of Natural Materials*, pages 87–99. Mono Book Co., Baltimore.
- Geist, E. and Dmowsky, R. (1999). Local tsunami and distributed slip at the source. *Pure and Applied Geophysics*, 154(485–512).
- Geist, E. L. (1997). Local tsunamis and earthquake source parameter. *Advances in Geophysics*, 39:117–209.
- Gersonde, R., A., D., Ivanov, B., and Kyte, F. T. (2002). Oceanic impacts – a growing field of fundamental science. *Deep Sea Research*, 49:951–957.
- Glikson, A. (1999). Oceanic mega impacts and crustal evolution. *Geology*, 27:387–390.
- Goff, J., McFadgen, B., and Chague-Goff, C. (2004). Sedimentary differences between the 2002 Eastern storm and the 15th-century Okoropunga tsunami southeastern North Island, New Zealand. *Marine Geology*, 204:235–250.

- Grieve, R., Robertson, P., and Dence, M. R. (1981). Multi-ring basins. In *Multi-ring Basins: Proceedings of the 12th Lunar and Planetary Science Conference*, pages 37–57.
- Harbitz, C. B. and Pedersen, G. (1992). Model theory and analytical solutions for large water waves due to landslides. *Preprint Series Insitut of Mathematics*, 4:17.
- Haymes, R. C. (1971). *Introduction to Space Science*. John Wiley & Son, Inc., New York.
- Hildebrand, A., Penfield, G., Kring, D., Pilkington, M., Jacobsen, S., and Boynton, W. (1991). Chicxulub crater: A possible Cretaceous–Tertiary boundary impact crater on the Yucatan Peninsula, Mexico. *Geology*, 19:867–871.
- Hirt, C., Amsden, A., and Cook, J. (1974). An arbitrary Lagrangian–Eulerian computing method for all flow field. *Journal of Computational Physics*, 14:227–253.
- Ivanov, B., Deniem, D., and Neukum, G. (1997). Implementation of dynamic strength models into 2D hydrocodes: Application for atmospheric breakup and impact cratering. *International Journal of Impact Engineering*, 20:411–430.
- Keller, G., Adatte, T., Stinnesbeck, W., Rebolledo-Vieyro, M., Fucugauchi, J., Kramar, U., and Stüben, D. (2004). Chicxulub impact predates the K–T boundary mass extinction. *PNAS*, 101(11):3753–3758.
- Lyne, J. E., Tauber, M., and Fought, R. (1996). An analytical model of the atmospheric entry of large meteors and its application to the tunguska event. *Journal of Geophysical Research*, 101:23207–23212.
- Lynett, P. and Liu, P. L.-F. (2002). A numerical study of submarine landslide generated waves and runup. *Proceedings of the Royal Society London*, 458:2885–2910.
- Marchuk, A. and Anisimov, A. (2001). A method for numerical modeling of tsunami wave run-up. In *ITS 2001*, pages 933–940.
- Melosh, H., J. (1989). *Impact Cratering: A Geological Process*. Oxford University Press, New York.

- Merriam, D. F. (2004). The quantification of geology: From the abacus to Pentium. a chronicle of people, places, and phenomena. *Earth Science Reviews*, 67:55–89.
- Morgan, J. and Warner, M. (1999). The third dimension of a multi-ring basin. *Geology*, 27:407–410.
- Nordyke, M. (1977). Proceedings of the symposium on planetary cratering mechanics. In Roddy, D., Pepin, R., and Merrill, R., editors, *Impact and Explosion Cratering*, pages 103–124. Pergamon New York.
- Okal, E., Plafker, G., Synolakis, C., and Borrero, J. (2003). Near-field survey of the 1946 Aleutian tsunami on Unimak and Sanak Islands. *Bulletin of the Seismological Society of America*, 93:1226–1234.
- Okal, E. and Synolakis, C. (2003). A theoretical comparison of tsunamis from dislocations and landslides. *Pure and Applied Geophysics*, 160:2177–2188.
- O’Keefe, J. and Ahrens, T. (1982). The interaction of the Cretaceous/Tertiary extinction bolide with the atmosphere, ocean and solid Earth. *Geological Society of America special paper*, 190:103–120.
- O’Keefe, J. and Ahrens, T. (1994). Impact-induced melting of planetary surfaces. *Geological Society of America special paper*, 293:103–109.
- Ormö, J. and Miyamoto, H. (2002). Computer modelling of the water resurge at a marine impact: The Lockne crater, Sweden. *Deep Sea Research II*, 49:983–994.
- Peregrine, D. (1967). Long waves on a beach. *Journal of Fluid Mechanics*, 27:815–827.
- Press, W., Teuklosky, S., Vetterling, W., and Flannery, B. (1992). *Numerical Recipes in C*. Cambridge University Press, 2nd edition.
- Scheffers, A. and Kelletat, D. (2003). Sedimentologic and geomorphologic tsunami imprints worldwide – a review. *Earth Science Reviews*, 63:83–92.
- Sepkoski, J. (1993). 10 years in the library – new data confirm paleontological pattern. *Paleobiology*, 19:43–51.

- Shoemaker, E. M. (1960). Penetration mechanics of high velocity meteorites, illustrated by the Meteor Crater. *Rept. of the Int. Geol. Congress.*
- Smit, J. (1999). The global stratigraphy of the Cretaceous–Tertiary boundary impact ejecta. *Annual Reviews of Planetary Science*, 27:75–113.
- Smit, J., Roep, T., Alvaret, W., Montanari, A., Claeys, P., Grajeles, J., and Bernudez, J. (1996). Coarse-grained, clastic sandstone complex at the K/T boundary around the Gulf of Mexico: Deposition by tsunami waves induced by the Chicxulub impact? *Geological Society of America special paper*, 307:151–182.
- Sonett, C., Pearce, S., and Gault, D. (1991). The oceanic impact of large objects. *Advances in Space Research*, 11:77–86.
- Stinnesbeck, W. and Keller, G. (1996). K/T boundary coarse-grained siliciclastic deposits in the northeastern Mexico and northeastern Brazil: Evidence for mega-tsunami or sea-level changes? *Geological Society of America special paper*, 307:197–209.
- Strelitz, R. (1979). Meteorite impact in the ocean. *Proceedings 10th Lunar Planet Conf.*, pages 2799–2813.
- Synolakis, C. (1986). *The runup of long waves*. PhD thesis, California Institute of Technology Pasadena, California.
- Synolakis, C. (1987). The runup of solitary waves. *Journal of Fluid Mechanics*, 185:523–545.
- Synolakis, C., Bardet, J., Borrero, J., Davis, H., Okal, E., Silver, E., Sweet, J., and Tapping, D. (2002). Slump origin of the 1998 Papua New Guinea tsunami. *Proceedings of the Royal Society London*, 458:763–789.
- Tadepalli, S. and Synolakis, C. E. (1994). The run-up of N-waves on sloping beaches. *Proceedings of the Royal Society London*, 445A:99–112.
- Thompson, S. and Lauson, H. (1972). Improvements in the chart D radiation-hydrodynamic CODE III: Revised analytical Equation of State. Technical report, Tech. Rep SC-RR7107714, Sandia National Laboratory.

- Titov, V. and Synolakis, C. E. (1995). Modeling of breaking and nonbreaking long-wave evolution and runup using VTCS-2. *Journal of Waterways, Ports, and Ocean Engineers*, 121(6):308–316.
- Titov, V. and Synolakis, C. E. (1998). Numerical modeling of tidal wave run-up. *Journal of Waterways, Ports, and Ocean Engineers*, 124(4):157–171.
- Tucker, M. and Wright, V. (1990). *Carbonate Sedimentology*. Blackwell Scientific Publications.
- Turtle, E., Pierazzo, E., Collins, G., Osinski, G., Melosh, H., Morgan, J., Reimold, W., and Spray, J. (2005). Impact structures: What does crater diameter mean? *Geological Society of America special paper*, 384:??–??, in press.
- van der Bergh, S. (1989). Life and death in the inner solar system. *Publications of the Astronomical Society of the Pacific*, 101:827–846.
- Ward, S. (2001). Landslide tsunamis. *Journal of Geophysical Research—Solid Earth*, 101(B06):11201–11215.
- Ward, S. and Asphaug, E. (2000). Asteroid impact tsunamis: a probabilistic hazard assessment. *Icarus*, 145:64–78.
- Ward, S. and Asphaug, E. (2003). Asteroid impact tsunami of 2880 March 16. *Geophysical Journal International*, 153:F6–F10.
- Ward, S. and Day, S. (2002). 2002, chapter Suboceanic Landslides, pages ??–?? McGraw-Hill.
- Ward, S. N. (2000). Tsunamis. In Meyers, R. A., editor, *The Encyclopedia of Physical Science and Technology*. Academic Press.
- Ward, S. N. and Asphaug, E. (2002). Impact tsunami – Eltanin. *Deep Sea Research II*, 49:1073–1079.
- Weisz, R., Wünnemann, and Bahlburg, H. (2003). Oceanic impacts, tsunamis and the influence of water depth on the quantity and characteristics of generated waves. In 3. *Large Meteoritic Impacts*.
- Wilkins, M. (1964). Calculation of elastic-plastic flow. *Methods in Computational Physics*, 3:211–263.

- Wünnemann, K. (2001). *Die Numerisch Behandlung von Impaktprozessen – Kraterbildung, stosswelleninduzierte Krustenmodifikationen und ozeanische Einschlagsereignisse*. PhD thesis, Institut of Geopyhsics, Westfälische Wilhelms Universität.
- Wünnemann, K. and Ivanov, B. (2003). Numerical modelling of impact crater depth–diameter dependence in an acoustically fluidized target. *Planetary and Space Science*, 51:831–845.
- Wünnemann, K. and Lange, M. (2002). Numerical modelling of impact induced modifications of the deep–sea floor. *Deep Sea Research II*, 49:969–981.

Danksagung

Zuerst möchte ich meiner Familie danken, die mich während der letzten drei Jahren stark entbehren mussten. Ich danke auch Heinrich Bahlburg, der an mich geglaubt hat und so manches möglich gemacht hat. Zum Beispiel ermöglichte er mir eine USA Reise in der ich einige Wochen an der Arbeit der Tsunami Research Group of the University of Southern California teilnehmen durfte. Dieser Aufenthalt war wohl das Schlüsselerlebnis für diese Arbeit. Ich wurde nicht nur in meiner Arbeitsweise bestätigt, sondern ich lernte auch interessante und erfrischende Menschen kennen. Zum einen wäre da Jose Borrero, der mir den Umgang mit MOST zeigte und mir in der Theorie erläuterte wie man surft. Zum anderen ist da noch Costas Synolakis, der seither inspiriert und mich ermutigt etwas offensiver zu meinen Ergebnissen und zu meiner Arbeitsweise zu stehen.

Aber auch in Münster sind eine ganze Menge Leute, denen ich vieles zu verdanken habe. Ich danke erst einmal allen, die mich mit Kaffee, Zucker und Brötchen versorgt haben. Ohne jene Menschen wäre diese Arbeit nie entstanden. Namentlich sind das: Nicole Dobrzinski, Christina Reimann, Judith Nagel, Wolfgang Peters-Kotting, Erasmus Westphal, Markus Euting und Holger Nübel.

Zu sehr grossem Dank verpflichtet bin ich Heiko Zumsprekel, Cornelia Reimann, Carita Augustsson und Billy Myers. Ohne sie wäre es nicht möglich diese Arbeit zu lesen. Hervorheben möchte ich Cornelia Reimann, die sich seit einigen Wochen traut mit mir ein Büro zu teilen.

Jedoch den größten Dank gilt meiner Sylvia, die mir immer hilft, auch in schwierigen Situationen, ich selbst zu bleiben und mich wiederzufinden, wenn ich mich mal verloren habe. Leider fehlen mir die Worte mein Dank adequat auszudrücken, deshalb werde ich es auf andere Art und Weise versuchen.

